
Electronic Thesis and Dissertation Repository

10-17-2017 3:00 PM

Seismic Performance of Steel Helical Piles

Moustafa K. El-sawy, *The University of Western Ontario*

Supervisor: Dr. M. Hesham El Naggar, *The University of Western Ontario*

A thesis submitted in partial fulfillment of the requirements for the Master of Engineering Science degree in Civil and Environmental Engineering

© Moustafa K. El-sawy 2017

Follow this and additional works at: <https://ir.lib.uwo.ca/etd>



Part of the [Civil Engineering Commons](#), [Geotechnical Engineering Commons](#), and the [Structural Engineering Commons](#)

Recommended Citation

El-sawy, Moustafa K., "Seismic Performance of Steel Helical Piles" (2017). *Electronic Thesis and Dissertation Repository*. 4999.

<https://ir.lib.uwo.ca/etd/4999>

This Dissertation/Thesis is brought to you for free and open access by Scholarship@Western. It has been accepted for inclusion in Electronic Thesis and Dissertation Repository by an authorized administrator of Scholarship@Western. For more information, please contact wlsadmin@uwo.ca.

ABSTRACT

Recent earthquakes have highlighted the need for safe and efficient construction of earthquake resilient structures. Meanwhile, helical piles are gaining popularity as a foundation for new structures and retrofitting solution for existing deficient foundations due to their immense advantages over conventional driven pile alternatives. In addition, helical pile foundations performed well in recent earthquakes, proving they can be a suitable foundation option in seismic regions. The objective of this thesis is to evaluate the seismic performance of helical piles by conducting full-scale shaking table tests and nonlinear three-dimensional numerical modeling using the computer program ABAQUS/Standard. The experimental setup involved installing ten steel piles with different configurations and pile head masses in dry sand enclosed in a laminar shear box mounted on the NEES/UCSD Large High Performance Outdoor Shake Table. The loading scheme consisted of white noise and two earthquake time histories with varying intensity and frequency content. The performance of different moment curve fitting techniques used for reduction of shake table experimental data are compared. The experimental results are presented in terms of natural frequency and response of the test piles. The effects of the loading intensity and frequency and the pile's geometrical configuration and installation method were evaluated. The dynamic numerical model constructed accounted properly for the test boundary conditions, employing tied vertical boundaries. In addition, the nonlinear behaviour of the soil during the strong ground motion was simulated by considering a strain-dependant shear modulus and applying Masing's loading-unloading rules by the overlay method to account for the soil nonlinearity more realistically. The numerical model was verified employing the full-scale experimental results, then was used to conduct a limited parametric study that investigated the effect of pile stiffness and the location of helix on its lateral response. The experimental results show that the natural frequency of the driven pile was slightly higher than that of the helical piles. However, the response of the helical pile was close to that of the driven pile, which illustrates the ability of helical piles to perform as good as conventional piles under seismic loading.

Keywords: Helical piles, full-scale, shaking table, dynamic, seismic, finite element, overlay.

CO-AUTHORSHIP STATEMENT

The design of the full-scale experimental test including the layout, instrumentation plan and loading schemes was provided by Drs. El Naggar and Cerato. All the physical experimental preparation and instrumentation were executed by professional contractors under the supervision of Dr. Amy Cerato at the University of Oklahoma. The piles were installed in the laminar box situated on the shake table at the University of California – San Diego (UCSD). The shake table was operated by the staff at UCSD under the supervision of Drs. El Naggar and Amy Cerato and the data were collected by the data acquisition system during the shake table tests. The raw data reduction, experimental results interpretation, numerical modeling and results publications were performed by the author alone under the supervision of Dr. El Naggar. The following publications were drafted by the authors and reviewed and edited by Dr. El Naggar.

1. **Elsawy, M.K.** et al. 2017. “Interpretation of Seismic Response Data from Full Scale Helical Piles Test.” In DFI - 42nd Annual Conference on Deep Foundations, New Orleans, LA, USA: Deep Foundations Institute. **Accepted**
2. Heidari, M., **M.K. Elsayy**, and M.H. El Naggar. 2017. “Nonlinear Seismic Response Analysis of Single Pile in Sand.” In PBD- III - 3rd International Conference on Performance Based Design in Earthquake Geotechnical Engineering, Vancouver, Canada. **Published.**

In addition, two journal manuscripts are prepared by the author and reviewed by Drs. El Naggar and Cerato and will be submitted in the near future for possible publication.

*To my lovely **mother** and **father***

To my sister and brother

To my supervisor, Dr. El Naggar

“The best teachers teach from the heart, not from the book.”

ACKNOWLEDGEMENTS

This thesis could have not been realized without a great deal of guidance and support. First, I would like to show my greatest appreciation to my advisor Dr. Hesham El Naggar for his continuous support and encouragement throughout the previous two years. His constant flow of ideas and expertise in this field has served as a foundation for the success of my work. I would also like to extend my gratitude to Dr. Mehdi Sarvestani for his persistent help and constructive suggestions through the hardships of my research.

I would also like to thank Dr. Amy Cerato and her research group for the great effort in preparing the experimental setup. I gratefully acknowledge all the financial support provided by the Helical Pile and Tiebacks Committee (HPTC) members through the Deep Foundation Institute's (DFI) Special Projects Fund, as well as the National Science Foundation (NSF). Furthermore, I would like to thank Torcsill Foundations LLC, Ram jack Foundation, Magnum Piering, Hubbell-Chance, and AMSquare for their generous help with the experimental testing.

Special thanks to all my family for their constant prayers and sympathetic ear. You are always there for me.

Finally yet importantly, thanks to all my friends for their constant flow of support and motivation.

TABLE OF CONTENTS

ABSTRACT.....	i
CO-AUTHORSHIP STATEMENT	ii
ACKNOWLEDGEMENTS	iv
LIST OF TABLES.....	viii
LIST OF FIGURES.....	ix
LIST OF ABBREVIATIONS AND SYMBOLS.....	xiv

INTRODUCTION

1.1 Overview	1
1.2 Objectives.....	3
1.3 Thesis Organization	3
1.4 References	5

LITERATURE REVIEW

2.1 Introduction to Helical piles.....	7
2.2 Static Lateral Capacity of a Helical Pile	10
2.2.1 Theoretical approaches	10
2.2.2 Experimental work.....	18
2.3 Dynamic Lateral Capacity of a Helical Pile	20
2.3.1 Theoretical work	20
2.3.2 Experimental work.....	26
2.4 Summary.....	29
2.5 References	30

FULL-SCALE SHAKING TABLE TEST SETUP AND DATA REDUCTION

3.1 Introduction.....	36
3.2 Experimental Setup	36

3.2.1	Shaking table mechanical system	36
3.2.2	Laminar soil shear box	37
3.2.3	Soil properties	38
3.2.4	Test piles: Installation and Instrumentation	42
3.2.5	Test program	48
3.3	Data preparation	50
3.3.1	Data filtering	50
3.3.2	Data interpretation	50
3.3.3	Curve fitting	52
3.4	Conclusions	61
3.5	References	63

EXPERIMENTAL RESULTS

4.1	Natural frequencies of Soil-Pile system.....	65
4.1.1	Effect of soil disturbance during installation	66
4.1.2	Effect of pile shaft shape.....	69
4.1.3	Effect of pile mass and diameter.....	70
4.1.4	Summary of piles response to white noise loading.....	71
4.2	Seismic response of helical piles.....	72
4.2.1	Effect of loading characteristics.....	72
4.3	Effect of pile configuration.....	77
4.3.1	Effect of installation method: helical pile versus driven pile (P2 vs P5)....	77
4.3.2	Effect of number of helices: single helix versus double helix (P2 vs P4) ..	80
4.3.3	Effect of pile shaft shape: circular shaft helical pile versus square shaft helical pile (P3 vs P6)	82
4.3.4	Effect of coupling type: threaded versus bolted coupling (P1 vs P2 and P3) 85	
4.4	Conclusions	86
4.5	References	89

NUMERICAL MODELING

5.1	Numerical Model features	91
5.1.1	3D Geometry.....	91
5.2	Element type	93
5.3	Material models	94
5.3.1	Pile material model	94
5.3.2	Soil material model	94
5.3.3	Damping.....	102
5.4	Pile – soil contact interface	105
5.5	Boundary conditions	106
5.5.1	Tied boundary validation	106
5.6	Mesh sensitivity analysis	110
5.6.1	Pile mesh.....	110
5.6.2	Soil mesh (combined system)	113
5.7	Final model verification with experimental results	116
5.7.1	Final model input parameters.....	116
5.7.2	Analysis steps.....	117
5.7.3	Model assumptions	119
5.7.4	Verification results.....	119
5.8	Parametric study	122
5.8.1	Effect of pile stiffness (EI).....	124
5.8.2	Effect of addition of second helix.....	129
5.9	Summary	133
5.10	References	134

SUMMARY, CONCLUSIONS AND RECOMMENDATIONS

6.1	Summary	136
6.2	Conclusions	137
6.3	Recommendations for future research	139
	Curriculum Vitae	140

LIST OF TABLES

Table 2-1: Summary of boundary conditions available in ABAQUS for dynamic analysis	25
Table 3-1: Test piles physical properties	44
Table 3-2: Added masses at each pile head	45
Table 3-3: Test program earthquake intensities	48
Table 3-4: Configurations for LPILE models	54
Table 3-5: Configuration 1 ranking methods for deflection and soil reaction.....	60
Table 3-6: Configuration 2 ranking of methods for deflection and soil reaction	61
Table 4-1: Summary of natural frequencies, period and expected spectral accelerations for both EQs for all soil-pile systems	72
Table 5-1: Selection schemes for w_1 and w_2	103
Table 5-2: Summary of damping for elastic and non-linear elements.....	104
Table 5-3: Soil properties used for validation of tied boundaries.....	107
Table 5-4: Pile material properties for mesh sensitivity	110
Table 5-5: Optimising pile mesh at zone 1 trials	112
Table 5-6: Error in deflection for each pile mesh trial.....	112
Table 5-7: Soil properties (all layers) for mesh sensitivity.....	114
Table 5-8: Optimising soil mesh at zone 1 trials	115
Table 5-9: Change in deflection for each soil mesh trial	115
Table 5-10: Summary of soil layers properties	117
Table 5-11: Pile material properties.....	117
Table 5-12: Analysis steps descriptions and boundary conditions	118
Table 5-13: Pile shaft and helix geometric properties used in parametric study	123
Table 5-14: Percentage contribution of each soil resistance component during load for each pile type with different pile stiffness	126

LIST OF FIGURES

Figure 2-1: Labor installing Helical pile manually by applying torque – After Lutenegger (2011).....	7
Figure 2-2: Typical helical pile configuration	8
Figure 2-3: Failure modes of laterally loaded piles	11
Figure 2-4: Subgrade Reaction approaches	12
Figure 2-5: Winkler model schematic.....	12
Figure 2-6: Schematic for p-y curve method	14
Figure 2-7: Integration and differentiation sequence of curves	15
Figure 2-8: Configuration of Passive Soil wedge in SW Model	16
Figure 3-1: Shaking table components schematic at NEES @ UCSD – (as per information provided in (“NERHI @ UC San Diego” n.d.))	37
Figure 3-2: Laminar soil shear box of NEES-UCSD testing facility.....	38
Figure 3-3: Grain size distribution of sand	39
Figure 3-4: Direct shear result – Shear stress vs normal stress.....	40
Figure 3-5: DCPT correlation for Effective Modulus (MPa) with DPI (mm/blow) – after De Beer and der Merwe (1991)	41
Figure 3-6: DCPT results along laminar shear box depth a) DPI with depth b) Effective modulus from correlation with depth.....	42
Figure 3-7: Installation torque profiles a) 88 mm diameter helical piles b) 140 mm diameter helical piles	45
Figure 3-8: Location of each test pile within the laminar shear box	46
Figure 3-9: North section - Piles instrumentation and elevations.....	46
Figure 3-10: South section - Piles instrumentation and elevations.....	47
Figure 3-11: Accelerometers locations within soil in laminar shear box	47
Figure 3-12: Unscaled Earthquake time records a) Northridge b) Takatori	49
Figure 3-13: Fourier Analysis of earthquake records a) Northridge b) Takatori.....	49
Figure 3-14: 5% Damped spectral acceleration (response spectrum) for earthquake records a) Northridge b) Takatori	50
Figure 3-15: General p-y curve approach	51

Figure 3-16: Curve fitting procedure	55
Figure 3-17: High degree global polynomial fit for Configuration 1 (Piles with 6 strain gauges)	57
Figure 3-18: Cubic interpolation and approximate splines for Configuration 1 (Piles with 6 strain gauges)	58
Figure 3-19: Cubic interpolation and approximate spline in Configuration 2 (Piles with 7 strain gauges)	59
Figure 4-1: Fourier spectra using response from strain gauges and accelerometer readings a) P1 (88-C-1HP) b) P2 (88-C-2HP)	66
Figure 4-2: Fourier spectra of single (P2) and double (P4) helical piles response to white noise excitation	68
Figure 4-3: Fourier spectra of helical (P2) and driven (P5) piles response to white noise excitation.....	68
Figure 4-4: Fourier spectra of circular (P2) and square shaft (P6) piles response to white noise excitation	69
Figure 4-5: Fourier spectra of circular (140-C-1HP) piles with different masses response to white noise	70
Figure 4-6: Fourier spectra of 88 mm diameter (P2) and 140 mm diameter (P8) response to white noise	71
Figure 4-7: Frequency effect on pile response a) Pile 6 - Square shaft helical pile b) Pile 1 - Circular shaft helical pile.....	74
Figure 4-8: Effect of load frequency on dynamic p-y curve for Pile 1 a) Depth of 1.25D b) Depth of 3D c) Depth of 5D d) Depth of 7D	75
Figure 4-9: Loading intensity correlation with maximum bending moment for P4 a) Northridge b) Takatori	76
Figure 4-10: Effect of loading intensity on dynamic p-y curve for Pile 1 Takatori a) Depth of 1.25D b) Depth of 3D c) Depth of 5D d) Depth of 7D.....	76
Figure 4-11: Effect of loading intensity on dynamic p-y curve for Pile 1 Northridge a) Depth of 1.25D b) Depth of 3D c) Depth of 5D d) Depth of 7D.....	77
Figure 4-12: Maximum deflection of single helical (P2) and driven (P5) piles a) Northridge 100% b) Takatori 100%	78

Figure 4-13: Comparison of dynamic p-y curves during Northridge 100% for single helical pile (P2) and driven pile (P5) at different depths a) 1.25D b) 3D c) 5D d) 7D	79
Figure 4-14: Comparison of dynamic p-y curves during Takatori 100% for single helical pile (P2) and driven pile (P5) at different depths a) 1.25D b) 3D c) 5D d) 7D	79
Figure 4-15: Comparison between maximum deflections of single helical (P2) and double helical (P4) piles during Northridge all intensities a) 100% b) 75% c) 50%	81
Figure 4-16: Comparison between maximum deflections of single helical (P2) and double helical (P4) piles during Takatori all intensities a) 100% b) 75% c) 50%	81
Figure 4-17: Comparison of dynamic p-y curves during Takatori 100% for single helical pile (P2) and double helical pile (P4) at different depths a) 1.25D b) 3D c) 5D d) 7D	82
Figure 4-18: Comparison of dynamic p-y curves during Takatori 50% for single helical pile (P2) and double helical pile (P4) at different depths a) 1.25D b) 3D c) 5D d) 7D	82
Figure 4-19: Maximum deflection of circular helical (P3) and square helical (P6) piles a) Northridge 100% b) Takatori 100%	83
Figure 4-20: Comparison of dynamic p-y curves during Northridge 100% for circular helical pile (P3) and square helical pile (P6) at different depths a) 1.25D b) 3D c) 5D d) 7D	84
Figure 4-21: Comparison of dynamic p-y curves during Takatori 100% for circular helical pile (P3) and square helical pile (P6) at different depths a) 1.25D b) 3D c) 5D d) 7D	84
Figure 4-22: Comparison of dynamic p-y curves during Takatori 100% for threaded coupling (P1) and bolted coupling (P2 and P3) at different depths a) 1.25D b) 3D c) 5D d) 7D.....	86
Figure 5-1: Soil block dimensions	92
Figure 5-2: Pile 1 dimensions	92
Figure 5-3: Comparison between reduced and fully integrated 8-node brick elements a) reduced integration b) full integration	94
Figure 5-4: MC model behaviour compared to example of real soil.....	96
Figure 5-5: Overlay elements schematic in overlay model using X = 4 stacked elements	97
Figure 5-6: One way loading-unloading stress-strain behaviour of overlay model using X = 4 stacked elements	97

Figure 5-7: Matasovic (1993) versus Seed & Idriss (1991) a) Shear modulus reduction with strain b) Damping with strain	100
Figure 5-8: Soil block elastic and non-linear regions	101
Figure 5-9: Rayleigh damping with frequency	103
Figure 5-10: Hysteretic damping schematic during one loading cycle for non-linear overlay elements	104
Figure 5-11: Tied boundaries a) Un-deformed b) Deformed.....	106
Figure 5-12: Acceleration at surface by DEEPSOIL and FE model with tied boundaries	108
Figure 5-13: Acceleration transfer function (output/input) by DEEPSOIL and FE model with tied boundaries	109
Figure 5-14: Pile mesh zones schematic	110
Figure 5-15: Loading for pile mesh sensitivity	111
Figure 5-16: Soil mesh zones schematic.....	113
Figure 5-17: Loading on pile for soil mesh sensitivity	114
Figure 5-18: Soil profile and layers thickness	116
Figure 5-19: Comparison Fourier spectra of pile response to white noise between FE Model and Experiment for Pile 1 (88-C-1HP)	120
Figure 5-20: Comparison of peak response between FE Model and Experiment results for Pile 1 (88-C-1HP) a) Displacement versus depth b) Bending moment versus depth.....	121
Figure 5-21: Comparison of dynamic p-y curves between FE Model and Experiment results for Pile 1 (88-C-1HP) at different depths a) 1.25D b) 3D c) 5D d) 7D	122
Figure 5-22: Schematic of piles used in parametric study a) Straight shaft b) Single helical c) Double helical	124
Figure 5-23: Effect of pile stiffness on deflection shape of different pile types a) Straight shaft b) Single helical c) Double helical	125
Figure 5-24: Effect of pile stiffness on force versus displacement at pile head for different pile types a) Straight shaft b) Single helical c) Double helical.....	125
Figure 5-25: p-y curves for flexible and rigid single helical pile at 3D. a) Total b) Normal c) Shear	127

Figure 5-26: p-y curves for flexible and rigid double helical pile at 3D. a) Total b) Normal c) Shear	128
Figure 5-27: Shear at helical plate for both single and double helical piles a) Flexible b) Rigid.....	129
Figure 5-28: Moment due helical plate for both single and double helical piles a) Flexible b) Rigid	130
Figure 5-29: Top and bottom helical plates for double helical pile when the pile is flexible a,d) Contact status b,e) Shear force c,f) Normal force.....	131
Figure 5-30: Top and bottom helical plates for double helical pile when the pile is rigid a,d) Contact status b,e) Shear force c,f) Normal force.....	131
Figure 5-31: Helical plate for single helical pile when the pile is flexible a) Contact status b) Shear force c) Normal force	132
Figure 5-32: Helical plate for single helical pile when the pile is rigid a) Contact status b) Shear force c) Normal force.....	132

LIST OF ABBREVIATIONS AND SYMBOLS

a, b	Matasovic (1993) curve fitting parameters
API	American petroleum institute
ASTM	American section of the International Association for Testing Materials
BWF	Beam on Winkler foundation
BNWF	Beam on non-linear Winkler foundation
C	Cohesion
C_u	Coefficient of uniformity
D	Pile diameter
D_{50}	Average grain size
[D]	Damping matrix
DAQ	Data acquisition
DPI	Dynamic penetration index
DCPT	Dynamic cone penetration test
E	Void ratio
EI	Flexural stiffness
E_s	Young's modulus of horizontal subgrade reaction in soil
E_p	Young's modulus for pile material
f_n	Nth natural frequency of soil
f_p	Earthquake predominant frequency
f_{p1}	Lower bound of predominant frequency range
f_{p2}	Upper bound of predominant frequency range
f_{pile}	Natural frequency of soil-pile system
f_{max}	Maximum frequency of input motion
$f_{soil-pile}$	Natural frequency of soil-pile system
F_c	Fines content
FEA	Finite element analysis
FFT	Fast Fourier Transform
G	Shear modulus
G_s	Specific gravity

G_{\max}	Initial shear modulus at zero strain
H	Total thickness
H_{SW}	Height of mobilised soil wedge
HiSS	Hierarchical single surface
I_p	Moment of inertia for pile cross-section
K	Stiffness of soil-pile system
k_x	Modulus of horizontal subgrade reaction
[K]	Stiffness matrix
L	Ratio of pile length inside soil
L_{SW}	Length of mobilised soil wedge
LHPOST	Large high-performance outdoor shake table
m	Total mass of system
$M(z)$	Bending moment function of pile length
MC	Mohr Coulomb
[M]	Mass matrix
NEES	Network for Earthquake Engineering Simulation
NHERI	Nation Home Education Research
P	Soil reaction
p_{contact}	Normal contact pressure between two surfaces
P	Magnitude of force
R	Relative stiffness factor
RMS	Root mean square
s, α	Matasovic (1993) backbone curve fitting parameters
SDOF	Single degree of freedom
SW	Strain wedge
UMAT	User defined material
UCSD	University of California, San Diego
USCS	Unified soil classification system
V_s	Shear wave velocity
w_1, w_2	Desired frequency damping frequency range
w_c	Water content

W_d	Energy dissipated
W_s	Energy stored
W_{SW}	Width of soil wedge
X	Depth along pile
y_{soil}	Far-field soil movement relative to input motion
y_{pile}	Pile deflection relative to pile tip
ϕ	Friction angle
γ	Shear strain
τ	Shear stress
μ	Friction coefficient
ν	Poisson's ratio
ξ	Target critical damping ratio
ε	Strain gauge reading
γ_r	Reference shear strain
σ_v	Overburden (vertical) stress
σ_{VM}	Von mises stress
σ_{ref}	Reference confining pressure = 0.18 MPa
β_{SW}	Base angle of mobilised soil wedge
θ_{SW}	Mobilised friction angle of soil wedge
τ_{crit}	Critical shear stress after which movement occurs
τ_{yield}	Mohr Coulomb failure/yield stress
$\alpha_{rayleigh}$	Mass proportional damping
$\beta_{rayleigh}$	Stiffness proportional damping

INTRODUCTION

1.1 Overview

Recent catastrophic earthquake events have underscored the need for safe design and construction of earthquake resistant structures. In particular, there is an increasing demand for safe and cost-effective foundation solutions suitable for retrofitting deficient foundations as well as supporting new structures in regions characterized with significant seismic hazard. Different foundation options are used to support structures and infrastructure in seismic regions, including the conventional driven steel and pre-cast concrete piles as well as drilled cast-in-place concrete piles. Some pile options did not perform well during past earthquakes. For example, there have been some exhumation studies from Japan's 1964 Niigata earthquake in a three-layer liquefiable zone that have shown broken reinforced concrete piles (e.g., Kawamura et al. 1985; Hamada et al. 1988; Yoshida and Hamada 1990; Hamada and O'Rourke 1992; Hamada 2000) at the interface of non-liquefiable and liquefiable layers, which experienced large lateral displacements. In addition, the construction industry is continuously pursuing innovative foundation solutions to reduce the cost and installation time and effort of foundation piles. Furthermore, the qualitative observations from recent earthquakes in Christchurch, New Zealand, and California, USA, demonstrated that structures supported on helical piles withstood multiple earthquakes with negligible structural damage. Therefore, there is a strong motivation to explore employing helical piles as a reliable and cost effective foundation option to support structures in seismic active areas.

A helical pile is comprised of a steel shaft pile with one or more helices welded to it. The steel shaft can have a square cross-section with rounded corners or a circular cross-section. Helical piles are installed into the ground by applying a mechanical torque to the pile head using the drive head mounted on a construction equipment. The length of pile shaft can be increased to satisfy the required depth by adding shaft extensions to the first lead section using bolted or threaded couplings. The installation method of helical piles facilitate using for retrofitting existing foundations since they can be installed in confined and limited

access spaces. Recently, helical piles have become an attractive alternative to conventional foundations to support new structures due to their many advantages, including: easy and rapid installation; efficient use of material; reduced cost and risk to labor; and most importantly, the ability to estimate its axial capacity using installation torque readings (Perko, 2009).

The behaviour of helical piles under axial loading has been the subject of numerous investigations (e.g. Livneh and El Naggar 2008; Sakr 2009; Elsherbiny and El Naggar 2013; Gavin et al. 2014). However, the lateral performance of helical piles has received much less attention due to the general perception they are not suitable for lateral loading due the small diameter of their shafts. In particular, there is a limited number of experimental studies that investigated the performance of full-scale single helical piles under cyclic or dynamic lateral loadings (e.g., Rao et al. 1993; Prasad and Rao 1994; Abdelghany 2008; Abdelghany and El Naggar 2010 & 2011; El Sharnouby and El Naggar 2012; Abdelghany and El Naggar 2014). Meanwhile, large diameter helical piles are widely used in practice nowadays and their axial response was investigated (e.g. Sakr 2009; Elsherbiny and El Naggar 2013; Elkasabgy and El Naggar 2015; Harnish and El Naggar 2017). In addition, a few studies investigated the lateral response of large diameter helical piles (Sakr 2009; Fahmy and El Naggar 2015, 2017) Much fewer studies investigated the lateral cyclic or dynamic behaviour of helical piles (e.g. Elkasabgy et al. 2010; Elsherbiny et al. 2017). However, in all previous studies, the cyclic or dynamic loading was applied at the pile head, which may not be representative of seismic loads. Up till now, there exists no published research that investigated full-scale seismic loading on helical piles and driven piles.

The current research involves the first full-scale testing of helical and driven piles using a large outdoor shaking table. Furthermore, a nonlinear three-dimensional finite element model was developed and verified using the experimental data, and was then used to conduct a limited parametric study to better understand and evaluate the effects of different aspects of the helical pile on its lateral performance.

1.2 Objectives

The current study investigates the seismic performance of helical piles by means of a full-scale shaking table test program and numerical modeling utilising the finite element software ABAQUS/Standard (SIMULIA, 2013). The full-scale experimental setup included ten steel piles with different configurations and pile head masses. The piles were installed in dry sand enclosed in a laminar shear box mounted on NEES/UCSD Large High Performance Outdoor Shake Table (LHPOST). The experimental results were discussed in terms of natural frequencies and responses of the piles under different loading schemes. The experimental results were then used to validate the dynamic numerical model. Finally, a parametric study was performed in order to investigate the effect of the pile's flexural stiffness and addition of second helix on the lateral performance and p-y curves.

1.3 Thesis Organization

This thesis consists of six chapters that have been organised in accordance with the guidelines provided by the School of Graduate and Postdoctoral Studies. A brief description of each chapter is listed below:

Chapter 1: Introduces helical piles and the research motivation, objectives and scope of work as well as description of the thesis organization.

Chapter 2: Provides a limited literature review on relevant topics of the research. It starts with a brief introduction to helical piles, followed by a description of available literature on the lateral behaviour of single helical piles. In addition, the previous theoretical approaches and experimental work regarding the behaviour of single straight shaft helical piles under both static and dynamic loading are discussed with an emphasis on the latter.

Chapter 3: Details the experimental setup, which includes the pile configurations, layout, instrumentation of piles and soil, soil testing and seismic loading schemes. In addition, the procedures employed for raw data reduction and evaluation of different curve fitting methods are discussed in detail.

Chapter 4: Presents the experimental results in terms of natural frequency and response of the test piles. The effect of pile installation method, number of helices, pile shaft shape and diameter on the natural frequency and response of the piles under different earthquakes is investigated. The response is presented as peak deflections or bending moment and dynamic p-y curves.

Chapter 5: Details of the main aspects of 3D finite element model that includes geometry, element type selection, material model formulations, contact formulation, boundary conditions and mesh sensitivity analysis. The numerical model was verified against experimental test results. Finally, the results of the limited parametric study are presented that evaluate the effect of pile stiffness and addition of second helix on the lateral response of helical piles.

Chapter 6: Brief description of the research work performed is summarized and the main conclusions drawn from previous chapters are listed. Finally, the recommendations for future research are also suggested at the end.

1.4 References

- Abdelghany, Y. 2008. Monotonic and Cyclic Behaviour of Helical Screw Piles Under Axial and Lateral Loading. The University of Western Ontario, Canada.
- Abdelghany, Y., and El Naggar, H. 2011. Steel Fibers Reinforced Grouted and Fiber Reinforced Polymer Helical Screw Piles—A New Dimension for Deep Foundations Seismic Performance. In *Geo-Frontiers 2011: Advances in Geotechnical Engineering*. pp. 103–112.
- Abdelghany, Y., and El Naggar, M.H. 2010. Monotonic and Cyclic Behavior of Helical Screw Piles Under Axial and Lateral Loading. Missouri University of Science and Technology.
- Abdelghany, Y., and El Naggar, M.H. 2014. Full-scale field investigations and numerical analyses of innovative seismic composite fiber-reinforced polymer and reinforced grouted helical screw instrumented piles under axial and lateral monotonic and cyclic loadings. In *Advances in Soil Dynamics and Foundation Engineering*. pp. 414–424.
- Elkasabgy, M.A., and El Naggar, M.H. 2015. Lateral Performance of Large-Capacity Helical Piles. In *IFCEE 2015*.
- Elkasabgy, M., El Naggar, M.H., and Sakr, M. 2010. Full-scale vertical and horizontal dynamic testing of a double helix screw pile. In *Proceedings of the 63rd Canadian Geotechnical Conference*, Calgary, Alta. pp. 12–16.
- Elsherbiny, Z.H., and El Naggar, M.H. 2013. Axial compressive capacity of helical piles from field tests and numerical study. *Canadian Geotechnical Journal*, 50(12): 1191–1203.
- Elsherbiny, Z.H., El Naggar, M.H., and ElGamal, A. 2017. Helical piles foundation for wind turbines: Full-scale testing of a single helical pile in sand. In *3rd International Conference on Performance-based Design in Earthquake Geotechnical Engineering*. Vancouver, Canada.
- Fahmy, A., and El Naggar, M.H. 2015. Lateral performance of helical tapered piles in sand. In *The Canadian Geotechnical Conference GEOQuebec*, Quebec, Canada.
- Fahmy, A., and El Naggar, M.H. 2017. Axial and lateral performance of spun-cast ductile iron helical tapered piles in clay. *Proceedings of the Institution of Civil Engineers-Geotechnical Engineering*,: 1–14.
- Gavin, K., Doherty, P., and Tolooiyan, A. 2014. Field investigation of the axial resistance of helical piles in dense sand. *Canadian Geotechnical Journal*, 51(11): 1343–1354.

- Hamada, M. 2000. Performances of foundations against liquefaction-induced permanent ground displacements. In Proceedings of the 12th World Conference on Earthquake Engineering, Auckland, New Zealand.
- Hamada, M., and O'Rourke, T. 1992. Case studies of liquefaction and lifeline performance during past earthquakes, Volume 1 Japanese Case Studies. National Center for Earthquake Engineering Research. SUNY at Buffalo, Red Jacket Quadrangle, Buffalo, NY, 14261.
- Hamada, M., Saito, K., Yasuda, S., and Isoyama, R. 1988. Earthquake damage by liquefaction-induced permanent ground displacement. In Proceedings of the Ninth World Conference on Earthquake Engineering, Tokyo-Kyoto. pp. 213–218.
- Harnish, J., and El Naggar, M.H. 2017. Large Diameter Helical Pile Capacity-Torque Correlations. Canadian Geotechnical Journal.
- Kawamura, S., Nishizawa, T., and Wada, H. 1985. Damage to piles due to liquefaction found by excavation twenty years after earthquakes. *Nikkei Architecture*, 7(29): 130–134.
- Livneh, B., and El Naggar, M.H. 2008. Axial testing and numerical modeling of square shaft helical piles under compressive and tensile loading. *Canadian Geotechnical Journal*, 45(8): 1142–1155.
- Perko, H.A. 2009. Helical Piles. In *Helical Piles: A Practical Guide to Design and Installation*. doi:10.1002/9780470549063.
- Prasad, Y., and Rao, S.N. 1994. Pullout behaviour of model pile and helical pile anchors subjected to lateral cyclic loading. *Canadian geotechnical journal*, 31(1): 110–119.
- Rao, S.N., Prasad, Y., and Veeresh, C. 1993. Behaviour of embedded model screw anchors in soft clays. *Geotechnique*, 43(4): 605–614.
- Sakr, M. 2009. Performance of helical piles in oil sand. *Canadian Geotechnical Journal*, 46(9): 1046–1061. doi:10.1139/T09-044.
- El Sharnouby, M.M., and El Naggar, M.H. 2012. Field investigation of axial monotonic and cyclic performance of reinforced helical pulldown Micropiles. *Canadian Geotechnical Journal*, 49(5): 560–573.
- SIMULIA. 2013. ABAQUS/CAE. Dassault Systèmes Simulia Corp, RI, USA.
- Yoshida, N., and Hamada, M. 1990. Damage to foundation piles and deformation pattern of ground due to liquefaction-induced permanent ground deformations. In Proceedings of the 3rd Japan-U.S. workshop on earthquake resistance design of lifeline facilities and countermeasures for soil liquefaction. San Francisco, CA. pp. 147–161.

LITERATURE REVIEW

This chapter provides a brief introduction to helical piles and summarises different theoretical approaches and experimental studies regarding the lateral response of single straight and helical piles. Both the static and dynamic lateral response characteristics are reviewed with an emphasis on the former.

2.1 Introduction to Helical piles

Alexander Mitchell, an Irish builder and brick manufacturer, was the first person to utilize helical (screw) shaped components for geotechnical purposes and was granted the first patent on helical piles in 1833. Mitchell initially used helical piles for mooring at the Port of London, UK. In 1838, Later, he introduced the concept of helical piles as a foundation at the Maplin Sands light-house, which was the first structure to be founded on helical piles. Figure 2-1 shows the manual installation of one of the helical piles used at the Maplin Sands light-house.

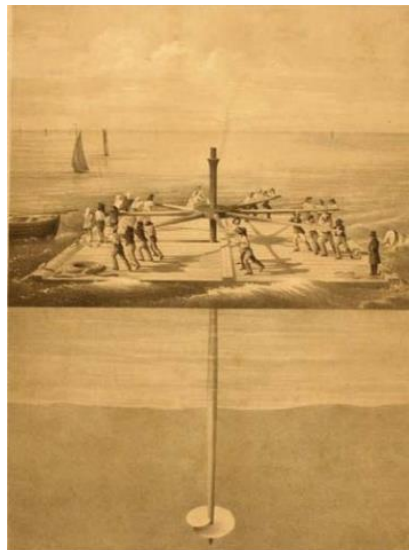


Figure 2-1: Labor installing Helical pile manually by applying torque – After Lutenegeger (2011)

Throughout the years, the geometry of helical piles has been refined, including multi-helix piles at the end of the nineteenth century. Today, helical piles consist of a straight steel shaft with one or more helical bearing plates welded to it. The pile is advanced into the soil using a combination of torque provided by the hydraulic torque motor and slight vertical downward pressure (crowd). A typical helical pile configuration is shown in Figure 2-2.

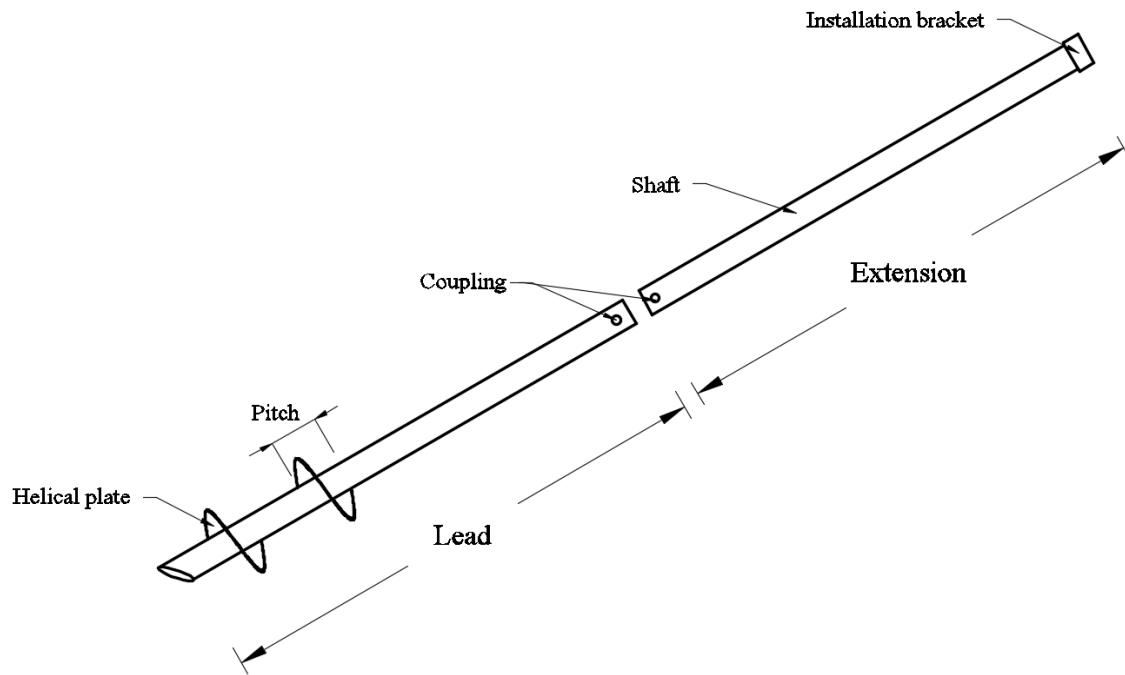


Figure 2-2: Typical helical pile configuration

Due to the nature of their installation technique and geometry, helical piles offer many advantages over the conventional bored or driven piles such as listed below (Perko 2009):

- **Rapid installation:** they don't require heavy or special equipment such as a crane or large driller. Usually, a rotational speed of 25 – 30 rpm and vertical speed of around one pitch depth per revolution are used, which allows complete installation of the pile within a few minutes.
- **Immediate load carrying capacity:** they have no “curing” time such as in concrete bored piles, thus can be loaded immediately after installation.
- **Minimum disturbance to the site:** there are no soil cuttings produced in the process of installation. Furthermore, **low level of noise and vibration** is associated with their installation.

- **Torque-capacity correlations:** the installation torque is measured by the installation equipment, which can be correlated to the axial load carrying capacity to provide good estimate of the pile capacity during installation (Canadian Geotechnical Society, 2006). This provides a cheaper alternative when compared to other types of piles that require on-site load tests. Perhaps, this is the most unique and important feature of helical piles as it provides an instant method for quality assurance/quality control.
- **Low carbon footprint:** the steel used to manufacture helical piles can be recycled and re-used.
- **Construction in limited spaces:** due to the small size equipment required for installation, helical piles can be installed in tight and low-head room places in applications involving retrofitting of existing deficient foundations or new structures.

Helical piles have been traditionally used to support light to medium weight buildings and structures or in tension applications. However, with advancement in installation machinery and the need for alternative foundations to support heavier loads, large diameter helical piles are used for residential and commercial buildings, as well as to support heavy equipment in industrial plants.

The main function of piles is to transfer loads from the structure further down to more competent soil layers. In addition to gravity loads, piles are often subjected to different forms of lateral loads. Examples of potential sources of lateral loading include: wind, earthquakes, waves, lateral earth pressure and dynamic loads from machines. The frequency of lateral load acting on the pile depends on the nature of the load. For example, earthquake loading usually contains frequencies ranging from 1 - 10 Hz, while machine loading can reach frequencies up to 200 Hz.

2.2 Static Lateral Capacity of a Helical Pile

2.2.1 Theoretical approaches

Several methods are available to calculate the lateral capacity of a pile, such as limit equilibrium analysis methods, beam on elastic support or Winkler approach with specified displacement criteria and strain wedge methods. The static lateral capacity of a helical pile can be calculated using the same methods; however, the effects of soil disturbance associated with pile installation due to the shearing effect of the helix as it advances through the soil should be accounted for. In addition, the increased bearing and friction resistance resulting from the helix, especially for helical plates placed near the ground surface, would contribute to the lateral capacity of the helical pile.

The following sections will discuss some of the theoretical methods that are employed to analyse the static lateral behaviour of a pile. The main assumptions and limitations of each method are presented and discussed.

2.2.1.1 Broms approach

Broms (1964a, 1964b) developed a method for calculating the lateral capacity of piles in sand and clay based on limiting equilibrium analysis. Broms defined two possible failure mechanisms: rigid pile and flexible pile. The pile's failure behaviour is dependent on the ratio of the pile embedded length (L) to the relative stiffness factor (R). The relative stiffness factor (R), defines the relative rigidity of the pile and adjacent soil, and is given by:

$$R = \sqrt[4]{EI / k_x} \quad (2.1)$$

Where: k_x is the modulus of horizontal subgrade reaction, EI is the flexural stiffness of the pile. The modulus of subgrade reaction, k_x , can either be constant or increases linearly with depth. For piles with $L/R < 2$, rigid pile behaviour occurs. On the other hand, for $L/R > 4$, flexible pile behaviour is observed (Davisson, 1970). As shown in Figure 2-3, rotation dominates the deflected shape of a rigid pile whereas flexural deflection defines the behaviour of a flexible pile.

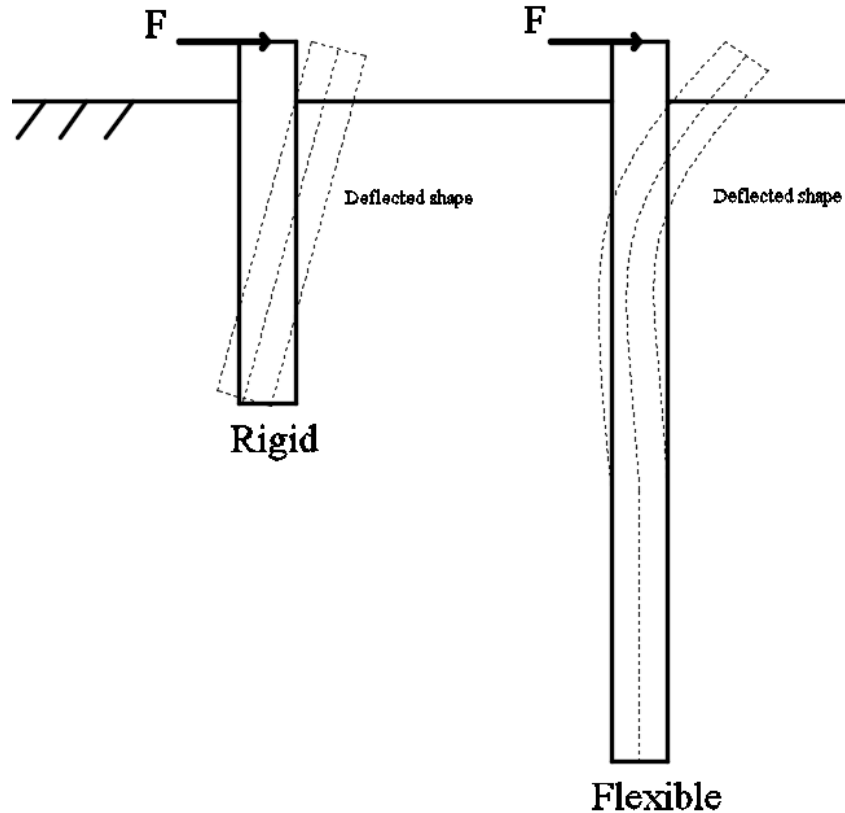


Figure 2-3: Failure modes of laterally loaded piles

The lateral capacity of a rigid pile is controlled by the resistance offered by the soil along the pile shaft, i.e., the lateral capacity is dominated by the failure of soil adjacent to the pile. On the other hand, the failure mechanism of a flexible pile involves the formation of a plastic hinge within the pile and the lateral capacity is influenced by both the flexural capacity of the pile and the soil resistance along the deflected length of the pile. In this case, the lateral capacity is computed by solving the system equilibrium considering the force applied at the pile head and the soil resistance to calculate the bending moment developed in the pile. If the calculated bending moment exceeds the plastic moment of the pile cross-section, the lateral capacity is calculated based on the pile failure considering its plastic moment. If the calculated the maximum bending moment, is less than the plastic capacity then the lateral capacity is calculated assuming the soil resistance along the deflected part of the pile. This method, however, does not provide any information regarding the deflection or serviceability state of the pile. It also does not take into account multi-layered soil profiles.

2.2.1.2 Subgrade reaction approach

The subgrade reaction approach forms the basis of three different methods as seen in Figure 2-4. Each method will be discussed briefly in this section.

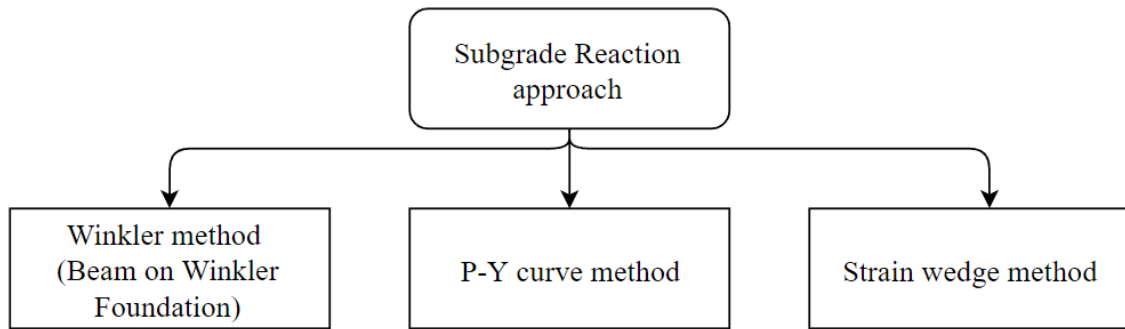


Figure 2-4: Subgrade Reaction approaches

Winkler method

The subgrade reaction approach was initially proposed by Winkler (1867) to analyse the soil-pile system as a beam (pile) resting on a series of independent linear elastic springs (soil) as shown in Figure 2-5.

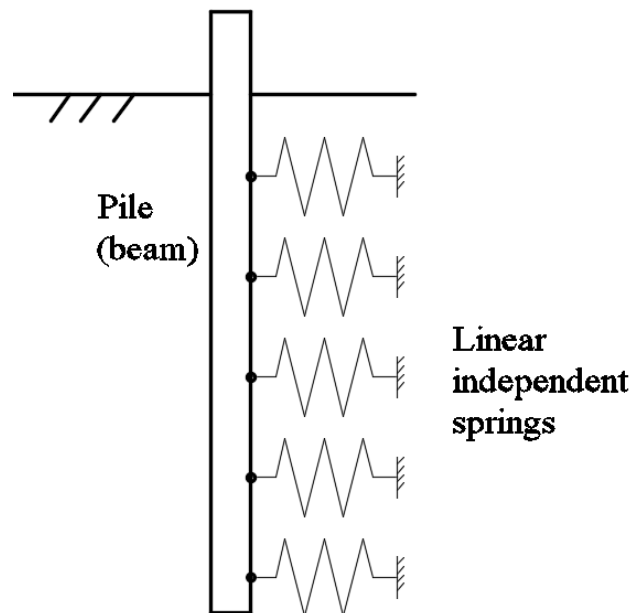


Figure 2-5: Winkler model schematic

This model is also known as **Beam on Winkler Foundation (BWF)** and is represented by the fourth order differential equation of equilibrium of the pile-soil system, i.e.:

$$E_p I_p \frac{d^4 y}{dx^4} + E_s x = 0 \quad (2.2)$$

Where: $E_p I_p$ is the flexural stiffness of the pile, E_s is the modulus of horizontal subgrade reaction and x is depth.

Hetényi (1946) derived a closed form solution utilizing the Winkler model to analyse the response of a laterally loaded pile installed in a single soil layer of constant subgrade modulus. Reese and Matlock (1956) developed a non-dimensional solution for the lateral response of a pile in a single soil layer with a subgrade modulus that increases with depth in a linear fashion. However, in most cases, the soil profile comprises several layers and both solutions are not applicable. Davisson and Gill (1963) extended the model to consider two soil layers instead of one. Puri et al. (1984) developed a mathematical model based on the Winkler's approach to calculate the lateral capacity of helical piles. The model accounts for the soil disturbance due to the pile installation technique. The theoretical model predictions were in good agreement with the experimental results of model pile load tests. The BWF model, however, is limited to linear elastic behavior due to the assumption of constant stiffness linear springs, which does not take into account for the non-linear soil behaviour. Therefore, it is only suitable for small loading conditions that lead to small soil strains where the soil behaviour remains within the linear range.

p-y curve method

Matlock (1970) introduced the p-y curve method to account for the soil non-linear behaviour. In this method, a series of non-linear springs replace the linear springs used in the BWF model as shown in Figure 2-6. The p-y curve is a force-deflection relationship that relates the soil resistance, p , to the pile deflection, y .

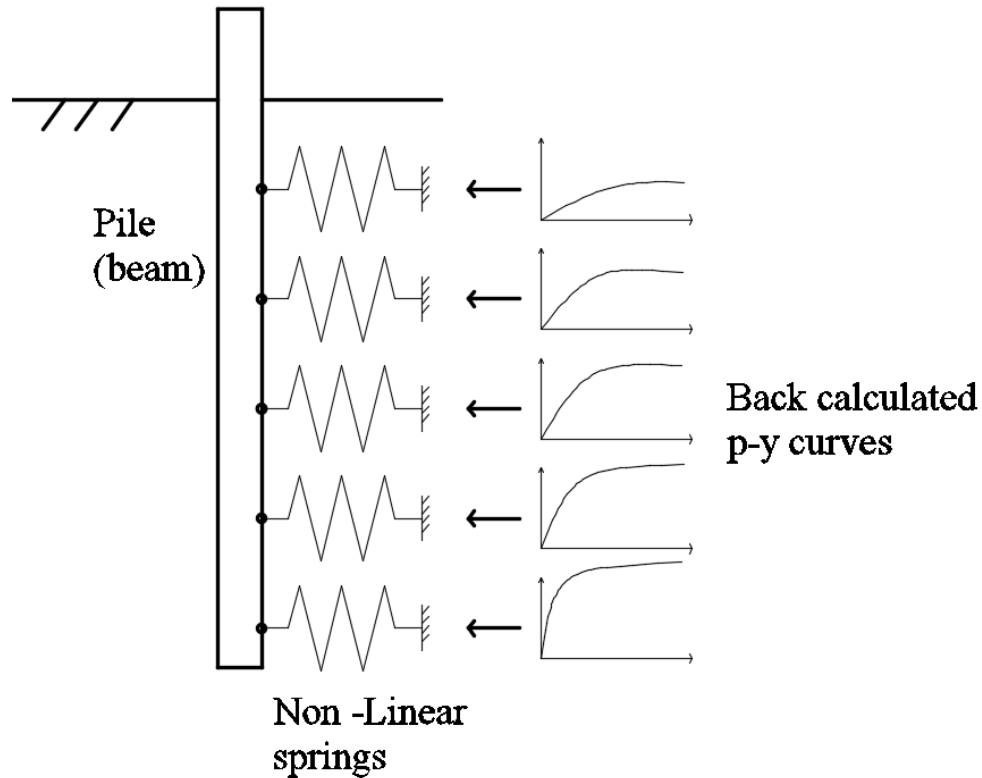


Figure 2-6: Schematic for p-y curve method

The basis of the p-y curve method is empirically derived p-y curves, which are back-calculated at different depths along the pile shaft from a set of full-scale lateral load tests. The procedure to obtain p-y curves from experimental tests is summarized as follows:

1. Obtain curvature readings at different locations (depths) along the pile shaft. This is most commonly achieved through the use of strain gauges or inclinometers.
2. Convert the curvature readings into moment values using the elastic bending moment relation (linear in the case of steel sections) between curvature and moment.
3. Employ a curve fitting technique to the moment and curvature data points to obtain a mathematical equation relating the moment with depth and curvature with depth.
4. Double integrate and double differentiate the moment curve to obtain deflection curves and soil reaction curves, respectively. The relationships between the different curves are shown in Figure 2-7.

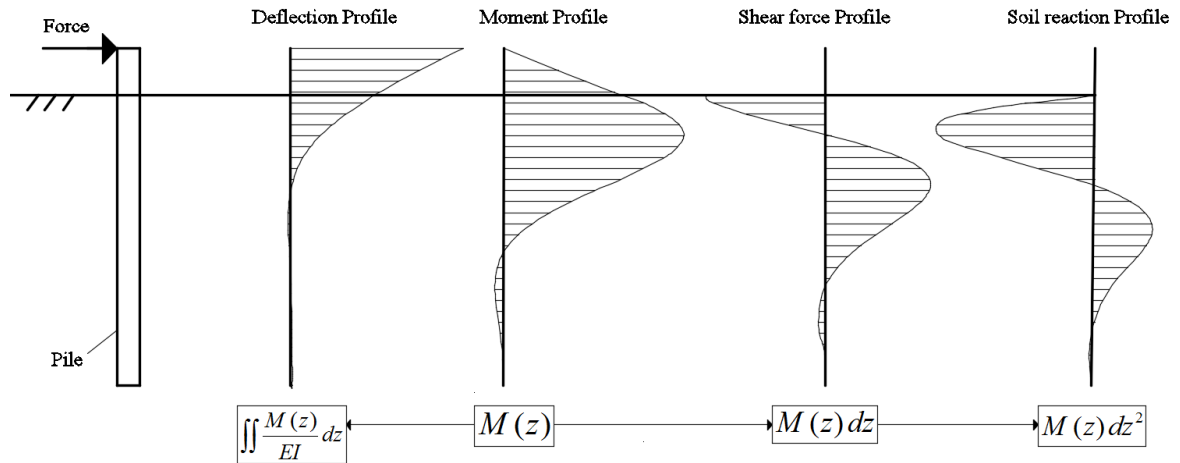


Figure 2-7: Integration and differentiation sequence of curves

The American Petroleum Institute (API) proposed standard p-y curves as part of pile design recommendations such as API 1987, 1993 and 2005 based on experimental test data (e.g, Matlock ,1970; Welch and Reese, 1972; Reese et al., 1974, 1975; Murchison and O’Neill, 1984). These curves are now being incorporated in most geotechnical software packages used in pile analysis and design such as LPILE (Ensoft Inc., 2011). Unfortunately, since the p-y curves method is limited to only the experimental tests of which the results are back calculated from, the p-y curves are representative of the pile configuration and soil conditions of the experimental data set. For example, most p-y curves are established load testing of relatively small diameter cylindrical piles, and hence they are not suitable for large diameter piles or square cross-sections.

Strain wedge method

The strain wedge (SW) method was developed by Ashour et al. (1998) to address the shortcomings of the p-y curves method. Unlike the p-y curves method, the SW method is semi-empirical and relates the pressure distribution (soil resistance) to the stress-strain-strength soil behaviour and the shape of the passive wedge formed in front of the pile foundation due to lateral loading. This model simplifies the complicated 3D pile-soil system formulated using the SW into one-dimensional by making the following assumptions (Ashour et al., 1998):

- Relate the horizontal stress change developed in the passive soil wedge to the soil reaction used in the BWF model.
- Relate the horizontal strain developed in the passive soil wedge to the pile deflection used in the BWF model.

Figure 2-8 displays a schematic of the passive mobilized soil wedge formed in front of the pile. The size and shape of the soil wedge are characterized by its length, L_{sw} , width, W_{sw} , height, H_{sw} , the base angle, β_{sw} , and mobilized friction angle θ_{sw} . The pile deflection pattern is assumed to be linear within the height of the wedge. The size of the mobilized soil wedge is obtained through an iterative process to satisfy equilibrium between the size of the wedge and the pile deflection under that specific loading. Additionally, it is assumed that the soil reaction obtained is only due to the resistance of the mobilized soil wedge and does not include any of the active soil pressure behind the pile.

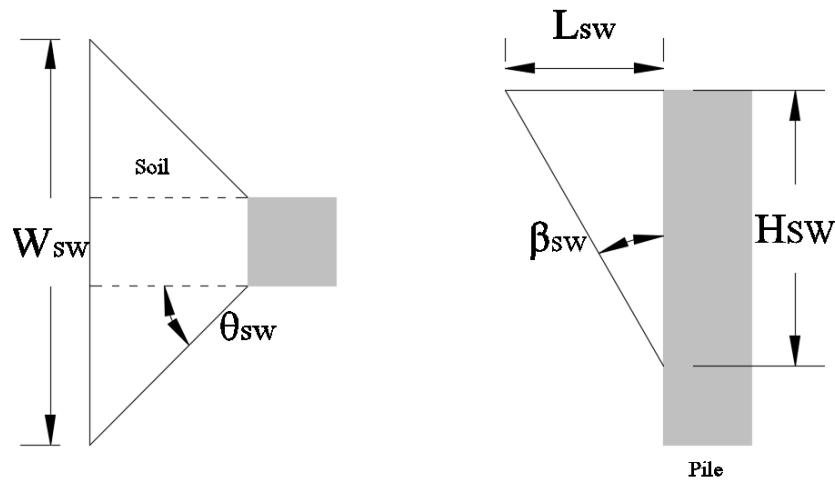


Figure 2-8: Configuration of Passive Soil wedge in SW Model

2.2.1.3 Continuum approach

In the continuum approach, the surrounding soil is modeled as a homogenous elastic continuum. Adopting the continuum approach, Mindlin (1936) developed a solution for the response of a concentrated point force acting in the interior of a semi-infinite solid. Perhaps, the earliest applications of this methodology to the lateral response of piles were proposed by Douglas and Davis (1964) for rigid piles and Poulos (1971) for flexible piles. In both methods, the pile is treated as a rectangular vertical strip divided into elements placed into a soil elastic continuum of constant modulus with depth. The soil displacement at each node is determined by Mindlin's integral solution. Poulos (1973) extended Mindlin's solution to take into account variation of soil modulus with depth. Banerjee and Davies (1978) provided a solution for multi-layered soil profile. In all of the above methods, the soil is modeled as an elastic medium.

Spillers and Stoll (1964) considered elastic-perfectly plastic soil behaviour to account for the non-linear yield behaviour of soil. Budhu and Davies (1988) incorporated both the non-linear behaviour in the soil and pile into a theoretical model for piles installed in soil with a linearly increasing modulus with depth. This model takes into account bearing capacity failure at the compressive zone underneath the foundation, shear failure along the interface of the soil-pile and tension failure in the soil.

2.2.1.4 Numerical approach

The finite element analysis (FEA) offers a very powerful computational tool to solve geotechnical problems with complicated loading, geometry and material behavior. It can provide a rigorous solution for complex soil profiles when an analytical solution is difficult to obtain. The domain (pile and soil) is divided into smaller pieces called finite elements connected at common nodes. The main model is defined with a global stiffness matrix that is constructed by the simple individual stiffness matrices of the smaller finite elements. By solving the equilibrium equation, the displacement at every single node can be obtained. Finally, the stresses and strain accompanied with these displacements can be computed. The FEA has the potential to address most of the shortcomings of other approaches such as soil continuity, nonlinear soil behaviour, nonlinear pile-soil interface conditions such as

gapping, 3D shape effects of pile cross-section and interaction of soil-pile system. On the other, the FEA is computationally demanding and requires special expertise in numerical modeling in order to provide reliable results. However, with advancement in computational systems, the FEA method has become more popular and affordable.

Yegian et al. (1973) developed a two-dimensional finite element model to analyze the response of a single pile installed in soft clay. Based on the FEA results, they established static p-y curves that accounted for the nonlinear soil material model and considered slip elements around the pile to represent the soil-pile interaction.

Kurian and Shah (2009) investigated numerically the effect of several parameters on the axial and lateral behaviour of helical piles. They developed a 3D FE model considering linear elastic behavior of the pile and implemented the Drucker-Prager plasticity model to represent the soil nonlinear behaviour. They investigated the effect of modeling the helix as a plane blade (usual simplified approach) with no pitch versus the actual microscopic geometry including the pitch. The results showed that including the helix pitch in the pile's geometry resulted in negligible change on the axial capacity but greatly increased the difficulty of the meshing process. Elsherbiny and El Naggar (2013) investigated the behaviour of helical piles in clay and sand using a 3D FE model in ABAQUS with linear elastic behaviour for the pile and elastic-plastic material model (Mohr-Coulomb) for the soil. Nur Eldayem and Mohamedzein (2016) investigated the performance of laterally loaded piles in clay using a 3D FE model in ABAQUS. The pile was modeled as a linear material while the modified Drucker-Prager model was used to simulate the soil. Fahmy and El Naggar (2016) and Fahmy and El Naggar (2017) studied the axial and lateral performance of helical tapered piles in clay and sand using 3D FE models employing ABAQUS with linear elastic behaviour for the pile and elastic-plastic material model (Mohr-Coulomb) for the soil.

2.2.2 Experimental work

The contribution of the helix to the lateral capacity of the pile generally depends on the location of the helix along the shaft and the expected behaviour of the pile (rigid or flexible). A helix placed at shallow depths can increase the lateral capacity of a pile by providing extra bearing and uplift resistance and friction along the helix surface.

Puri et al. (1984) performed lateral load tests on model helical piles with single, double and triple helices. The results showed that the effect of the number of helices on the lateral capacity was negligible and it was controlled almost entirely by the extension section close to the surface of the soil (flexible piles). Prasad and Rao (1994) investigated the effect of lateral cyclic loading on the pull out capacity of model helical piles. The experimental setup included model steel jacked and helical piles. Their results show that the lateral cyclic loading had negligible effect on the pullout capacity of helical piles while the pullout capacity of jacked piles decreased greatly. Prasad and Rao (1996) conducted lateral load tests on relatively rigid model helical piles in a laboratory set up. They demonstrated that the static lateral capacity of a helical pile was greater than that of a straight slender shaft and the lateral capacity increased as the number of helical plates increased. They also developed a theoretical model that confirmed the beneficial effect of the helical plate on the lateral capacity of the pile due to the increased bearing, uplift and frictional resistance on the helical plate's surface. Qin and Guo (2016) investigated the response of model rigid piles installed in sand under cyclic loading. The results demonstrated that the load level had a greater impact than number of cycles during cyclic loading. The results also demonstrated that there is a linear relationship between the maximum bending moment and applied lateral load independent of the number of cycles applied.

Sakr (2009) performed lateral tests on full-scale helical piles installed in oil sands. He concluded that the lateral behaviour of the test helical piles was mainly controlled by the size of the shaft (cross-section area and inertia). Furthermore, an increase in the number of helices caused very slight reduction in the lateral capacity of the helical piles due to the disturbance associated with installation. Elkasabgy and El Nagggar (2015) investigated the lateral performance of large-capacity full-scale double helical piles. Two piles (6.0m and 9.0m long) installed in cohesive soil were subjected to static lateral load testing at two different times: two weeks and nine months after installation. The results showed that the ultimate lateral capacity increased with time. Furthermore, the modulus of subgrade reaction obtained from the lateral tests was smaller than the calculated modulus of intact soil, which highlights the effect of soil disturbance during installation. Fahmy and El Nagggar (2015, 2016) studied the static and cyclic lateral behaviour of full-scale tapered helical piles in silty sand. Their results show an increase in lateral capacity due to the helical

plate for short piles. They also concluded that the tapered piles generally exhibited stiffer behaviour when compared to straight shaft helical piles.

2.3 Dynamic Lateral Capacity of a Helical Pile

2.3.1 Theoretical work

Lateral dynamic behaviour of single piles is typically evaluated using modified versions of the beam on Winkler foundation models similar to those discussed in Section 2.2.1.

2.3.1.1 Subgrade reaction approach

The conventional static BWF model has been modified to introduce the **Beam on Non-linear Winkler Foundation (BNWF)** model in order to simulate the dynamic behaviour of piles. Several BNWF models have been developed to account for certain non-linear aspects of the pile behaviour under dynamic loading. Recent advanced models account for pile installation effects, soil gapping, soil degradation and soil damping. In general, the analysis of piles seismic response using BNWF models involves two stages:

1. Determining the free-field motion of the soil alone
2. Applying the free-field motion at the end of the soil springs supporting the pile

Matlock et al. (1978) developed a BNWF model considering soil degradation, gapping and damping. In this model, the pile is represented by linear elastic beam elements supported by non-linear detachable Winkler soil springs on each side of the pile. In addition, linear dashpots and friction blocks are placed on both sides of the pile to account for the hysteretic and radiation damping. To reduce the computational demand, the springs at deep depths are modeled as linear elastic springs with no gapping. Kagawa and Kraft (1980) provided closed-form solution to analyze the dynamic lateral behaviour of piles. In this solution, the spring stiffness is related to the elastic modulus of soil through a non-dimensional soil reaction coefficient. Their results demonstrated that this soil reaction coefficient depended on the soil and pile dynamic properties as well as the loading conditions (i.e., whether the load applied at pile head or seismic load originating from bedrock). The soil reaction coefficient also varied significantly along the pile shaft. Consequently, they developed a

simple procedure to modify the lateral load-deflection curves of piles in homogenous elastic soils to account for the nonlinear soil-pile-structure interaction for both loading at the pile head (active) or seismic shaking (passive).

Nogami and Konagai (1988) developed transfer functions to evaluate the flexural response of a single pile under dynamic loading in the frequency-domain. Boulanger et al. (1999) evaluated the performance of a BNWF model in predicting the seismic soil-pile-structure interaction effects. Features such as damping and gapping were included using the procedures proposed by Wang et al. (1998) and Matlock et al. (1978), respectively. They compared the predictions of the numerical model with the results obtained from dynamic centrifuge tests on model piles. The numerical results were in reasonable agreement with the dynamic centrifuge tests. Allotey and El Naggar (2008) developed a versatile dynamic BNWF model capable of analysing the behaviour of piles under both quasi static (i.e. pushover) and time history loading. The model is currently implemented in SeismoStruct (SeismoSoft, 2003) software. The model takes into account pile non-linear behaviour, soil gapping and cave in, radiation damping and soil strength degradation. The authors state the model's main advantage over previous BNWF models is the computational speed and efficiency.

In most BNWF models described above, the soil resistance is usually represented by a single spring at each elevation. To account for soil continuity and energy dissipation in the far field, a class of subgrade reaction models represent the soil resistance at each elevation utilizing two springs in series, one to simulate near field behaviour and one to simulate the far field condition. For example, Novak and Sheta (1980) discretized the soil medium into two zones; inner and outer zones. The inner zone included effects of gapping and soil non-linearity, while the outer zone was modeled as a linear elastic region. Similarly, Nogami and Chen (1987) developed a hybrid model that included near and far field springs. The focus was on determining the effect of the non-linear near field springs on the lateral behaviour of the pile. Nogami et al. (1992) proposed a simple soil-pile interaction model using frequency independent mass, springs (near field and far field) and dashpots. The parameters of the springs and dashpots can be obtained from static p-y curves. El Naggar and Novak (1996) developed a model including inner field and far field springs on either

side of the pile. The inner field soil is modeled by nonlinear springs and dashpots while the far field soil consists of linear elastic springs and dashpots. The gapping and slippage are modeled at the soil-pile interface. The inner field springs can only carry compression forces and when the force becomes zero, separation occurs. When gapping occurs, the node is kept at its displaced position and a permanent gap develops. The model also accounts for group effects by joining individual piles within a group with virtual springs and dashpots. The model was validated against field tests and similar analytical approaches by other authors.

El Naggar and Bentley (2000) developed dynamic p-y curves to represent different features of dynamic soil-pile interaction. The conventional static p-y curves were used to generate the non-linear spring stiffness resulting in dynamic p-y curves considering loading dimensionless frequency and apparent velocity of the soil particles. The resulting dynamic p-y curves could provide a relatively simple method to analyse piles under harmonic loading. Rovithis et al. (2009) developed a simplified procedure for producing dynamic p-y curves based on the BNWF method from sampled pile bending moments data. The procedure is validated using data from a well-documented dynamic centrifuge test on a single pile. However, the procedure is based on the assumption that there is a perfect bond between the pile and soil and no separation occurs during shaking.

2.3.1.2 Continuum approach

Novak (1974) proposed an analytical approach based on linear elasticity to determine closed-form formulas for the pile dynamic stiffness and damping. Novak and Nogami (1977) examined the interaction between soil and a pile vibrating in the horizontal direction. The pile was modeled as a linear elastic material and the soil as a linear viscoelastic layer overlying rigid bedrock. A closed-form solution was developed to calculate the pile dynamic stiffness and damping as well as its response. Gazetas (1991) proposed a complete set of equations and charts to determine the dynamic stiffness and damping coefficients of piles under harmonic shaking based on an elastic and homogenous half-space. All geometric foundation shapes and possible significant modes of vibration were taken into account.

2.3.1.3 Numerical approach

As the numerical modeling in this study was performed using the general finite element analysis program ABAQUS, a brief discussion of some of the features of the program with an emphasis on boundary conditions suitable for static and dynamic analyses.

ABAQUS boundary conditions

In finite element analyses, it is important to properly account for boundary conditions for reliable prediction of pile behaviour. In static analysis, the boundaries are usually assumed to be fixed and are placed at a sufficiently far distance in such a way they have no effect on the results within the region of interest. On the other hand, in dynamic analysis, the boundary conditions play a far more important role and its treatment is much more complex depending on the type of dynamic loading and its frequency range.

For geotechnical problems, the dynamic forces can either originate from within the model (e.g. shaking equipment resting on soil) or externally (e.g. seismic waves due to bedrock movement). The selection of the boundary conditions depends on which case is involved in the analysis, and proper selection of boundaries is critical for ensuring reliable results.

In the case of dynamic forces originating within the model (e.g. dynamic load applied at pile head), fixed boundaries can be placed at a large distance from the sources so as to allow the waves to be absorbed through soil damping and die out before reaching the fixed boundaries. If the distance is not sufficient, waves will be reflected back as they impact the fixed boundaries causing energy to be trapped within the model. Although this method is simple, increasing the model size will result in undesirable and unnecessary increase in computational time and effort. Alternatively, springs and dashpots may be attached at the boundaries to absorb incident waves (e.g., infinite and absorbing boundaries). Infinite boundaries involves placing finite element with virtual length that extends to infinity to represent wave propagation into the far field. Absorbing boundaries (e.g. Lysmer and Kuhlemeyer, 1969) involve dashpots that are utilized to dissipate the energy of impacting waves. These boundaries can be placed relatively close to the region of interest and hence can reduce the model size significantly. It completely absorbs waves approaching the boundary at normal incidence; however, for waves with oblique angles of incidence the

energy absorption is not perfect. Several studies (e.g., Lindman, 1975; Randall, 1988; Higdon, 1990; Zhao and Valliappan, 1993) have proposed absorbing boundaries to overcome the shortcomings of the infinite boundaries but none of these methods are currently readily available in ABAQUS and “Infinite Boundary” remains the only readily available absorbing boundary in ABAQUS. The user can implement other methods manually through user-defined subroutines.

For dynamic loading applied through the boundary (e.g. seismic waves due to bedrock movement simulated in laminar shear box tests), the soil block itself is being displaced by applying acceleration at the base (bedrock motion). The use of fixed boundaries on the sides even at large distance from the region of interest will not work as this will prevent the soil block from translating. Infinite boundaries by Lysmer and Kuhlemeyer (1969) also cannot be used because they attenuate the input motion (overdamp) as it travels up the soil; this effect is known as leakage (Nielsen, 2014). There are two solutions to this problem; Tied boundaries and Free Field Elements. Tied boundaries were introduced by Zienkiewicz et al. (1989), which involve constraining corresponding nodes (on the lateral boundaries) at every elevation to move together. This is essentially the same excitation mechanism of a laminar shear box. Any excitation wave due to pile shaking within the model that exits through the right boundary will re-enter at the left boundary. Therefore, when using this approach, the boundaries should be placed at a sufficient distance to allow dissipation of energy resulting from the pile (within the model). On the other hand, Free Field Elements (FFUEL) boundary was introduced by Nielsen (2006) and consists of two components: viscous dashpots that absorb radiating energy and soil column element that ensures undisturbed free-field motion at the boundaries. The FFUEL code is implemented in ABAQUS through the User defined elements subroutine code (UEL) provided by Nielsen (2006).

Table 2-1 summarises the boundary conditions available in ABAQUS for different cases of dynamic analysis.

Table 2-1: Summary of boundary conditions available in ABAQUS for dynamic analysis

Cases for source of dynamic waves	Fixed	Infinite elements	Tied	Free Field (FFUEL)
Case 1 – within model	✓	✓	✓	✓
Case 2 – outside model			✓	✓

Previous dynamic FE studies

Angelides and Roesset (1981) investigated the effect of nonlinear soil behaviour on the dynamic lateral response of piles. A consistent boundary matrix was placed at some distance from the region of interest to allow energy absorption. A quasi 3D FE program PILE-3D was developed by Wu and Finn (1997) for the dynamic analysis of soil-pile-structure interaction. The pile and soil are modeled using two-node and eight node brick elements, respectively. The soil model incorporates soil yielding. The nonlinear hysteretic behaviour of soil is performed using the equivalent linear method. Gapping between the soil and pile is allowed by ensuring that the normal stress in the direction of shaking does not exceed the tensile strength (zero for sand). Dashpots are placed at the boundaries to absorb incoming waves and simulate infinite soil medium. Bentley and El Naggar (2000) constructed a 3D FE model using ANSYS (ANSYS Inc., 1996) to evaluate the kinematic soil-pile interaction. The model incorporated soil nonlinear behaviour, pile gapping and energy dissipation. Transmitting boundaries were used at the sides of the model to prevent wave reflection.

Cai et al. (2000) investigated the seismic response of a soil-pile-structure system. Hierarchical single surface (HiSS) advanced constitutive law is used to represent the soil's (clay) nonlinearity and to represent the interface which is composed of a thin layer of eight-node solid elements between the pile and soil. Absorbing boundaries were used based on the work of Zhao and Valliappan (1993). Maheshwari et al. (2004) investigated the effects

of soil nonlinearity and separation between the soil and pile on the dynamic behaviour of single pile and pile groups. The 3D FE model used the Hierarchical single surface (HiSS) material model for the soil and a linear material model for the pile. By using symmetry and anti symmetry, only one fourth of the model was constructed. Kelvin elements (combination of dashpots and springs) are placed at the lateral boundaries to eliminate entrapment of energy within the model. Ground motion is applied at the base of the soil which is assumed to be bedrock. It was found that effect of soil non-linearity on the response of the soil-pile system was evident at low frequencies of dynamic loading and negligible at high frequencies.

Ayothiraman and Boominathan (2006) constructed a simple 2D plane strain model using PLAXIS to determine the efficiency of the model on replicating experimental results. The pile was modeled using elastic beam elements and the soil was modeled using 15 nodes triangular element. The soil material behaviour was assumed to be elastic-perfectly plastic using the Mohr-Coulomb failure criteria. Fixities are placed on the outer boundaries and built-in PLAXIS absorbing dashpots are used to prevent wave reflection at the boundaries. The simple 2D plane strain model reasonably predicted the experimental behaviour. Rovithis et al. (2009) studied the dynamic response of coupled soil-pile-structure systems under seismic loading. The system was represented as a concentrated mass attached to the head of a single degree of freedom pile installed in soil. The 3D FE model was constructed using ANSYS (ANSYS Inc., 1996). The soil consists of linear 8-noded brick elements while the pile is composed of linear beam elements.

2.3.2 Experimental work

Novak and F. Grigg (1976) performed dynamic tests on small model single and pile groups by applying harmonic motion at the pile heads via a Lazan mechanical oscillator to evaluate dynamic stiffness of piles. Yang et al. (2011) performed a series of 1g shaking table tests on model piles installed in both dry and saturated dense sand to determine the effect of various conditions of input motion and pile physical characteristics on the dynamic p-y curves. The results showed that the p-y curves were largely affected by the magnitude of input acceleration and how close the frequency of input motion is to the natural frequency of the soil-pile system (resonance effect).

Ting and Scott (1984) performed centrifuge model tests on a single pile and two pile groups embedded in saturated sand. The dynamic load was applied at the pile heads with an eccentric mass shaker. The results showed that the dynamic secant modulus for single and pile groups was lower than the static secant modulus for small pile deflections but became greater for higher pile deflections. Ting et al. (1987) investigated the behaviour of a single model pile embedded in saturated sand using a centrifuge model and compared the results to a similar full-scale test. The dynamic load was applied at the pile head by a specially built compressed-air-driven miniature eccentric-mass shaker. The results showed that for dense sand, there was limited nonlinearity and the stiffness was relatively independent of frequency of loading. Also, the damping ratio evaluated from the centrifuge tests remained constant during shaking. However, the damping ratio was observed to increase during the full-scale test at larger pile deflections. Weissman and Prevost (1989) conducted centrifuge model tests to study soil-structure interaction systems under earthquake loading. The model was validated through three stages: free-field soil tests, dynamic soil-structure interaction and numerical analysis of the experimental results. The target earthquake shaking loads with specific amplitude and frequency were generated by a hammer-exciter plate method at the base of the centrifuge. The validation results demonstrated the capability of the centrifuge model to behave as expected for simple dynamic soil-structure systems under earthquake loading. Dou and Byrne (1996) investigated the pile response and soil-pile interaction during earthquake loading and free vibrations. The earthquake loading was applied using a small shaking table. The model piles were installed in sand within the shaking table. To simulate full-scale tests, a hydraulic gradient similitude device was used. This device covered the whole shaking table and applies air pressure to increase the effective stresses in the model. The dynamic p-y curves obtained from the test agreed reasonably with API curves at deep depths. At shallow depths, the p-y curves exhibited highly non-linear behaviour. Kagawa et al. (2004) documented three case studies for dynamic centrifuge tests simulating full-scale shaking table tests for soil-pile-structure systems. The degree of agreement was considered satisfactory and the authors mention several assumptions and limitations involved in dynamic centrifuge testing such as: scaling issues, variation of centrifuge acceleration within the model and boundary effects.

Scott et al. (1982) investigated the performance of two full-scale steel piles driven in saturated silty sand subjected to lateral dynamic loads. Two vibration generators (counter-rotating weight) applied the dynamic loads at the pile head.

Han and Novak (1988) conducted dynamic experiments on full-scale piles in sand under lateral and vertical excitation. An exciter with two counter rotating eccentric masses was used to apply the load at the pile heads. They concluded that considering a weakened zone around the pile when subjected to strong vibration reasonably approximated the nonlinear behaviour of the soil. By considering this weakened zone with suitably chosen soil characteristics, the nonlinear behavior of the pile could be reasonably predicted using equivalent linear approach without resorting to fully nonlinear analysis. Elkasabgy et al. (2010) and Elkasabgy and El Naggari (2013) investigated the dynamic performance of helical piles through full-scale testing. Both vertical and lateral dynamic loads were applied at the pile head via a Lazan mechanical oscillator. The experimental results were used to verify the applicability of theoretical formulations (linear continuum approach and non-linear approach) on predicting the stiffness and damping of helical piles. The calculated response using the non-linear model in DYNA 6 (El Naggari et al. 2011) was in good agreement with the experimental results. Fleming et al. (2015) investigated the seismic performance of full-scale piles in improved and unimproved soft clay. Cement deep soil mixing was used to provide the improved soil. Two steel piles, one installed in improved clay and the other installed in unimproved clay, were subjected to quasi-static and seismic loading at the pile head via a dynamic actuator. The pile installed in the improved clay showed 42% increase in lateral strength, 600% increase in elastic stiffness and 650% increase in equivalent damping ratio.

2.4 Summary

This chapter presents a summary of the current available literature on the lateral performance of straight shaft and helical piles. The literature includes both previous experimental work and theoretical approaches. Both the static and dynamic behaviours are included with an emphasis on the latter. The literature survey reveals a knowledge gap regarding the full-scale dynamic behaviour of helical piles under seismic loading which encourages further investigation.

2.5 References

- Allotey, N., and El Naggar, M.H. 2008. Generalized dynamic Winkler model for nonlinear soil--structure interaction analysis. *Canadian Geotechnical Journal*, 45(4): 560–573.
- Angelides, D.C., and Roesset, J.M. 1981. Nonlinear lateral dynamic stiffness of piles. *Journal of Geotechnical and Geoenvironmental Engineering*, 107(ASCE 16635 Proceeding).
- ANSYS Inc. 1996. ANSYS General finite element analysis program. Canonsburg, PA.
- Ashour, M., Norris, G., and Pilling, P. 1998. Lateral loading of a pile in layered soil using the strain wedge model. *Journal of Geotechnical and Geoenvironmental engineering*, 124(4): 303–315. American Society of Civil Engineers.
- Ayothiraman, R., and Boominathan, A. 2006. Observed and predicted dynamic lateral response of single pile in clay. In *Soil and Rock Behavior and Modeling*. pp. 367–374.
- Banerjee, P.K., and Davies, T.G. 1978. The behaviour of axially and laterally loaded single piles embedded in nonhomogeneous soils. *Geotechnique*, 28(3): 309–326.
- Bentley, K.J., and El Naggar, M.H. 2000. Numerical analysis of kinematic response of single piles. *Canadian Geotechnical Journal*, 37(6): 1368–1382.
- Boulanger, B.R.W., Curras, C.J., Member, S., Kutter, B.L., Wilson, D.W., Member, A., and Abghari, A. 1999. Seismic soil-pile-structure interaction experiments and analyses. *Journal of Geotechnical and Geoenvironmental Engineering*, 125(September): 750–759.
- Broms, B.B. 1964a. Lateral resistance of piles in cohesionless soils. *Journal of the Soil Mechanics and Foundations Division*, 90(3): 123–158. ASCE.
- Broms, B.B. 1964b. Lateral resistance of piles in cohesive soils. *Journal of the Soil Mechanics and Foundations Division*, 90(2): 27–64. ASCE.
- Budhu, M., and Davies, T.G. 1988. Analysis of laterally loaded piles in soft clays. *Journal of geotechnical engineering*, 114(1): 21–39. American Society of Civil Engineers.
- Cai, Y.X., Gould, P.L., and Desai, C.S. 2000. Nonlinear analysis of 3D seismic interaction of soil--pile--structure systems and application. *Engineering Structures*, 22(2): 191–199.
- Canadian Geotechnical Society. 2006. Canadian foundation engineering manual. Richmond, B.C.
- Davisson, M.T. 1970. *Laterally Loaded Capacity of Piles*.
- Davisson, M.T., and Gill, H.L. 1963. Laterally Loaded Piles in a Layered Soil System, ASCE. In *Proceedings of ASCE*.

- Dou, H., and Byrne, P.M. 1996. Dynamic response of single piles and soil–pile interaction. *Canadian Geotechnical Journal*, 33(1): 80–96. NRC Research Press. doi:10.1139/t96-025.
- Douglas, D.J., and Davis, E.H. 1964. The movement of buried footings due to moment and horizontal load and the movement of anchor plates. *Geotechnique*, 14(2): 115–132.
- Elkasabgy, M.A., and El Naggar, M.H. 2015. Lateral Performance of Large-Capacity Helical Piles. In IFCEE 2015.
- Elkasabgy, M., and El Naggar, M.H. 2013. Dynamic response of vertically loaded helical and driven steel piles. *Canadian Geotechnical Journal*, 50(5): 521–535.
- Elkasabgy, M., El Naggar, M.H., and Sakr, M. 2010. Full-scale vertical and horizontal dynamic testing of a double helix screw pile. In *Proceedings of the 63rd Canadian Geotechnical Conference*, Calgary, Alta. pp. 12–16.
- Elsherbiny, Z.H., and El Naggar, M.H. 2013. Axial compressive capacity of helical piles from field tests and numerical study. *Canadian Geotechnical Journal*, 50(12): 1191–1203.
- Ensoft Inc. 2011. LPILE v6.0: A program for the analysis of piles and drilled shafts under lateral loads. Ensoft Inc., Austin, Texas.
- Fahmy, A., and El Naggar, M.H. 2015. Lateral performance of helical tapered piles in sand. In *The Canadian Geotechnical Conference GEOQuebec*, Quebec, Canada.
- Fahmy, A., and El Naggar, M.H. 2016. Cyclic lateral performance of helical tapered piles in silty sand. *DFI Journal-The Journal of the Deep Foundations Institute*, 10(3): 111–124.
- Fahmy, A., and El Naggar, M.H. 2017. Axial and lateral performance of spun-cast ductile iron helical tapered piles in clay. *Proceedings of the Institution of Civil Engineers-Geotechnical Engineering*,: 1–14.
- Fleming, B.J., Sritharan, S., Miller, G.A., and Muraleetharan, K.K. 2015. Full-Scale Seismic Testing of Piles in Improved and Unimproved Soft Clay. *Earthquake Spectra*, 32(1): 239–265. Earthquake Engineering Research Institute. doi:10.1193/012714EQS018M.
- Gazetas, G. 1991. Formulas and charts for impedances of surface and embedded foundations. *Journal of geotechnical engineering*, 117(9): 1363–1381. American Society of Civil Engineers.
- Han, Y., and Novak, M. 1988. Dynamic behaviour of single piles under strong harmonic excitation. *Canadian Geotechnical Journal*, 25(3): 523–534.
- Hetényi, M. 1946. *Beams on Elastic Foundation;: Theory with Applications in the Fields of Civil and Mechanical Engineering*. University of Michigan press.

- Higdon, R.L. 1990. Radiation boundary conditions for elastic wave propagation. *SIAM Journal on Numerical Analysis*, 27(4): 831–869.
- Kagawa, T., and Kraft, L.M. 1980. Lateral load-deflection relationships of piles subjected to dynamic loadings. *Soils and Foundations*, 20(4): 19–36. THE JAPANESE GEOTECHNICAL SOCIETY.
- Kagawa, T., Sato, M., Minowa, C., Abe, A., and Tazoh, T. 2004. Centrifuge Simulations of Large-Scale Shaking Table Tests: Case Studies. *Journal of Geotechnical and Geoenvironmental Engineering*, 130(7): 663–672. doi:10.1061/(ASCE)1090-0241(2004)130:7(663).
- Kurian, N.P., and Shah, S.J. 2009. Studies on the behaviour of screw piles by the finite element method. *Canadian Geotechnical Journal*, 46(6): 627–638.
- Lindman, E.L. 1975. “Free-space” boundary conditions for the time dependent wave equation. *Journal of computational physics*, 18(1): 66–78.
- Lutenegger, A.J. 2011. Historical development of iron screw-pile foundations: 1836--1900. *The International Journal for the History of Engineering & Technology*, 81(1): 108–128.
- Lysmer, J., and Kuhlemeyer, R.L. 1969. Finite dynamic model for infinite media. *Journal of the Engineering Mechanics Division*, 95(4): 859–878. ASCE.
- Maheshwari, B.K., Truman, K.Z., Naggar, M.H. El, and Gould, P.L. 2004. Three-dimensional finite element nonlinear dynamic analysis of pile groups for lateral transient and seismic excitations. *Canadian geotechnical journal*, 41(1): 118–133.
- Matlock, H. 1970. Correlations for design of laterally loaded piles in soft clay. *Offshore Technology in Civil Engineering’s Hall of Fame Papers from the Early Years*,: 77–94.
- Matlock, H., Foo, S.H.C., and others. 1978. Simulation of lateral pile behavior under earthquake motion. In *From Volume I of Earthquake Engineering and Soil Dynamics--Proceedings of the ASCE Geotechnical Engineering Division Specialty Conference*, June 19-21, 1978, Pasadena, California.
- Mindlin, R.D. 1936. Force at a point in the interior of a semi-infinite solid. *Physics*, 7(5): 195–202.
- Murchison, J.M., and O’Neill, M.W. 1984. Evaluation of $p-y$ relationships in cohesionless soils. In *Analysis and design of pile foundations*. pp. 174–191.
- El Naggar, M.H., and Bentley, K.J. 2000. Dynamic analysis for laterally loaded piles and dynamic $p-y$ curves. *Canadian Geotechnical Journal*, 37(6): 1166–1183.
- El Naggar, M.H., and Novak, M. 1996. Nonlinear analysis for dynamic lateral pile response. *Soil Dynamics and Earthquake Engineering*, 15(4): 233–244.

- El Naggar, M.H., Novak, M., Sheta, M., El Hifnawi, L., and El-Marsafawi, H. 2011. DYNA 6 - a computer program for calculation of foundation response to dynamic loads. Geotechnical Research Center, The University of Western Ontario, London, Ontario.
- Nielsen, A.H. 2006. Absorbing boundary conditions for seismic analysis in ABAQUS. In Proc. of the 2006 ABAQUS Users' Conference, Cambridge, Massachusetts. pp. 23–25.
- Nielsen, A.H. 2014. Towards a complete framework for seismic analysis in ABAQUS. Proceedings of the ICE-Engineering and Computational Mechanics, 167(1): 3–12.
- Nogami, T., and Chen, H.-L. 1987. Prediction of dynamic lateral response of nonlinear single-pile by using Winkler soil model. In Dynamic Response of Pile Foundations—Experiment, Analysis and Observation. pp. 39–52.
- Nogami, T., and Konagai, K. 1988. Time domain flexural response of dynamically loaded single piles. Journal of Engineering Mechanics, 114(9): 1512–1525. American Society of Civil Engineers.
- Nogami, T., Otani, J., Konagai, K., and Chen, H.-L. 1992. Nonlinear soil-pile interaction model for dynamic lateral motion. Journal of Geotechnical Engineering, 118(1): 89–106. American Society of Civil Engineers.
- Novak, M. 1974. Dynamic stiffness and damping of piles. Canadian Geotechnical Journal, 11(4): 574–598.
- Novak, M., and F. Grigg, R. 1976. Dynamic experiments with small pile foundations. Canadian Geotechnical Journal, 13(4): 372–385.
- Novak, M., and Nogami, T. 1977. Soil-pile interaction in horizontal vibration. Earthquake Engineering & Structural Dynamics, 5(3): 263–281.
- Novak, M., and Sheta, M. 1980. Approximate approach to contact effects of piles. In Dynamic response of pile foundations: analytical aspects. pp. 53–79.
- Nur Eldayem, F.E.E., and Mohamedzein, Y.E.-A. 2016. Finite Element Analysis of Laterally Loaded Piles in Clays. In Geo-China 2016. pp. 175–182.
- Perko, H.A. 2009. Helical Piles. In Helical Piles: A Practical Guide to Design and Installation. doi:10.1002/9780470549063.
- Poulos, H.G. 1971. Behavior of laterally loaded piles I. Single Piles. Journal of Soil Mechanics & Foundations Div.
- Poulos, H.G. 1973. Load-deflection prediction for laterally loaded piles.
- Prasad, Y., and Rao, S.N. 1994. Pullout behaviour of model pile and helical pile anchors subjected to lateral cyclic loading. Canadian geotechnical journal, 31(1): 110–119.

- Prasad, Y.V.S.N., and Rao, S.N. 1996. Lateral Capacity of Helical Piles in Clays . American Society of Civil Engineers , NEW YORK . doi:10.1061/(ASCE)0733-9410(1996)122:11(938).
- Puri, V.K., Stephenson, R.W., Dziedzic, E., and Goen, L. 1984. Helical anchor piles under lateral loading. In *Laterally Loaded Deep Foundations: Analysis and Performance*. ASTM International.
- Qin, H., and Guo, W.D. 2016. Response of static and cyclic laterally loaded rigid piles in sand. *Marine Georesources & Geotechnology*, 34(2): 138–153.
- Randall, C.J. 1988. Absorbing boundary condition for the elastic wave equation. *Geophysics*, 53(5): 611–624. Society of Exploration Geophysicists.
- Reese, L.C., Cox, W.R., and Koop, F.D. 1974. Analysis of laterally loaded piles in sand. *Offshore Technology in Civil Engineering Hall of Fame Papers from the Early Years*,: 95–105.
- Reese, L.C., Cox, W.R., Koop, F.D., and others. 1975. Field testing and analysis of laterally loaded piles on stiff clay. In *Offshore Technology Conference*.
- Reese, L.C., and Matlock, H. 1956. Non-dimensional solutions for laterally-loaded piles with soil modulus assumed proportional to depth. Association of Drilled Shaft Contractors.
- Rovithis, E., Kirtas, E., and Pitilakis, K. 2009a. Experimental p-y loops for estimating seismic soil-pile interaction. *Bulletin of Earthquake Engineering*, 7(3): 719–736. doi:10.1007/s10518-009-9116-7.
- Rovithis, E.N., Pitilakis, K.D., and Mylonakis, G.E. 2009b. Seismic analysis of coupled soil-pile-structure systems leading to the definition of a pseudo-natural SSI frequency. *Soil Dynamics and Earthquake Engineering*, 29(6): 1005–1015.
- Sakr, M. 2009. Performance of helical piles in oil sand. *Canadian Geotechnical Journal*, 46(9): 1046–1061. doi:10.1139/T09-044.
- Scott, R.F., Tsai, C.F., Steussy, D., and Ting, J.M. 1982. Full-scale dynamic lateral pile tests. In *14th Annual Offshore Technology Conference*. pp. 435–450.
- SeismoSoft. 2003. *SeismoStruct -- A computer program for static and nonlinear analysis of frame structures*.
- Spillers, W.R., and Stoll, R.D. 1964. Lateral response of piles. *Journal of the Soil Mechanics and Foundations Division*, 90(6): 1–10. ASCE.
- Ting, J.M., Kauffman, C.R., and Lovicsek, M. 1987. Centrifuge static and dynamic lateral pile behaviour. *Canadian Geotechnical Journal*, 24(2): 198–207.

- Ting, J.M., and Scott, R.F. 1984. Static and Dynamic Lateral Pile Group Action'. In 8th World Conference on Earthquake Engineering. pp. 641–648.
- Wang, S., Kutter, B.L., Chacko, M.J., Wilson, D.W., Boulanger, R.W., and Abghari, A. 1998. Nonlinear seismic soil-pile structure interaction. *Earthquake spectra*, 14(2): 377–396.
- Weissman, K., and Prevost, J.H. 1989. Centrifugal modelling of dynamic soil-structure interaction. *Earthquake Engineering & Structural Dynamics*, 18(8): 1145–1161.
- Welch, R.C., and Reese, L.C. 1972. Lateral load behavior of drilled shafts.
- Winkler, E. 1867. *Theory of elasticity and strength*. Dominicus, Prague.
- Wu, G., and Finn, W.D.L. 1997. Dynamic nonlinear analysis of pile foundations using finite element method in the time domain. *Canadian Geotechnical Journal*, 34(1): 44–52.
- Yang, E.-K., Choi, J.-I., Kwon, S.-Y., and Kim, M.-M. 2011. Development of dynamic py backbone curves for a single pile in dense sand by 1g shaking table tests. *KSCE Journal of Civil Engineering*, 15(5): 813–821.
- Yegian, M., Wright, S.G., and others. 1973. Lateral Soil Resistance Displacement Relationships for Pile Foundation in Soft clays. In *Offshore Technology Conference*.
- Zhao, C., and Valliappan, S. 1993. A dynamic infinite element for three-dimensional infinite-domain wave problems. *International journal for numerical methods in engineering*, 36(15): 2567–2580. Wiley Online Library.
- Zienkiewicz, O.C., Bicanic, N., and Shen, F.Q. 1989. Earthquake Input Definition and the Transmitting Boundary Conditions. In *Advances in computational nonlinear mechanics*. Springer. pp. 109–138.

FULL-SCALE SHAKING TABLE TEST SETUP AND DATA REDUCTION

3.1 Introduction

This chapter describes the experimental setup and data reduction of the full-scale shaking table testing that was conducted to evaluate the seismic performance of helical piles. The tests were performed employing the Large High Performance Shake Table (LHPOST) located at The University of California - San Diego. This facility is part of the Englekirk Structural Engineering Research Center and is supported by the National Science Foundation (NSF). The details of the experimental setup include the piles configurations, layout, and material properties; instrumentation of piles and soil; soil testing; and seismic loading scheme. The raw data reduction procedure is also described in detail, which includes filtering of raw data and the comparison of different curve fitting methods.

3.2 Experimental Setup

3.2.1 Shaking table mechanical system

The tests were conducted employing the NEES/UCSD Large High Performance Outdoor Shake Table (LHPOST), which is the largest outdoor shake table outside of Japan. The LHPOST was designed to handle 6 degrees of freedom movement. However, it is currently equipped with vertical and horizontal actuators only, which allow producing a total of 4 degrees of freedom. For this test, the vertical actuators were not used.

The shake table is 7.6 m x 12.2 m and is capable of handling up to 20 MN vertical payload. The table is powered by two horizontal force actuators each with a capacity of 6.8 MN capable of ± 0.75 m stroke length. The force actuators can produce a peak acceleration and velocity of 4.2 g and 1.8 m/s, respectively. The operating frequency range is 0 – 33 Hz. A schematic of the shaking table components is shown in Figure 3-1.

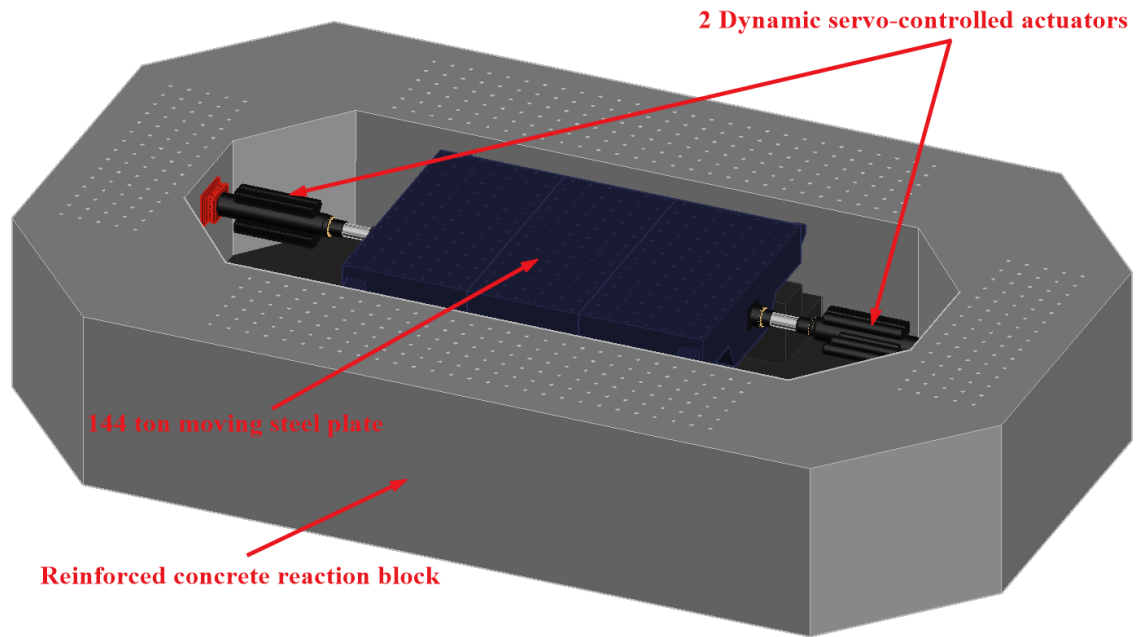


Figure 3-1: Shaking table components schematic at NEES @ UCSD – (as per information provided in (“NERHI @ UC San Diego” n.d.))

3.2.2 Laminar soil shear box

The laminar soil shear box used is 6.7 m long, 3.0 m wide and 4.7 m high, as shown in Figure 3-2. It consists of 31 steel laminar frames that are separated by steel rollers to allow for uni-directional movement, one dimensional shear deformation inside the soil and to minimize reflection of energy waves propagating throughout the soil. Nine W 8 x 35 sections are placed at the lower region of the box followed by sixteen W 8 x 15 sections in the mid height region and six W 8 x 10 sections in the uppermost region. This arrangement minimizes the weight of the box, which leads to a laminar frame weight to soil weight ratio of 8% – 15%. This is similar to other full-scale laminar soil shear boxes used in similar test facilities in Japan such as the laminar shear box in the National Research Institute for Earth Science and Disaster (NIED) located at Tsukuba, Japan (Ishihara et al., 1996).

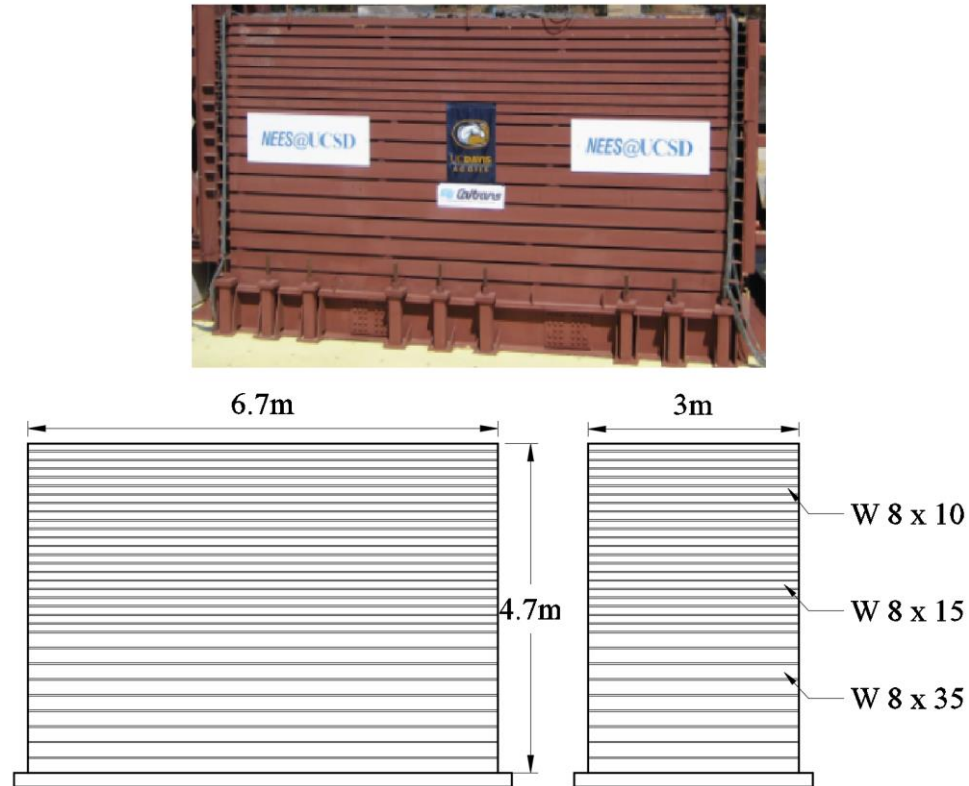


Figure 3-2: Laminar soil shear box of NEES-UCSD testing facility

3.2.3 Soil properties

The sand deposit prepared in the laminar box was placed within a thin waterproof polypropylene liner and was compacted to approximately 100% relative density. The total depth of the soil bed was 4.57 m, which was accomplished in layers of thickness 25 cm each. The same compaction effort was utilized for each layer to ensure relatively uniform density across the depth and along the cross-section of the laminar box.

3.2.3.1 Laboratory tests

Soil classification

Sieve analysis was performed according to ASTM C136 (2014) to determine the particle size distribution. Figure 3-3 shows the grain size distribution of the sand deposit obtained from the sieve analysis. The sand is classified as well-graded sand (SW) according to USCS (Unified Soil Classification System) with average grain size $D_{50} = 0.85$ mm, coefficient of

uniformity $C_u = 7.65$, specific gravity $G_s = 2.667$, unit weight of 19.5 kN/m^3 , water content (w_c) = 6.0%, fines content (F_c) = 4.5%, maximum and minimum void ratio (e) of 0.74 and 0.47 respectively.

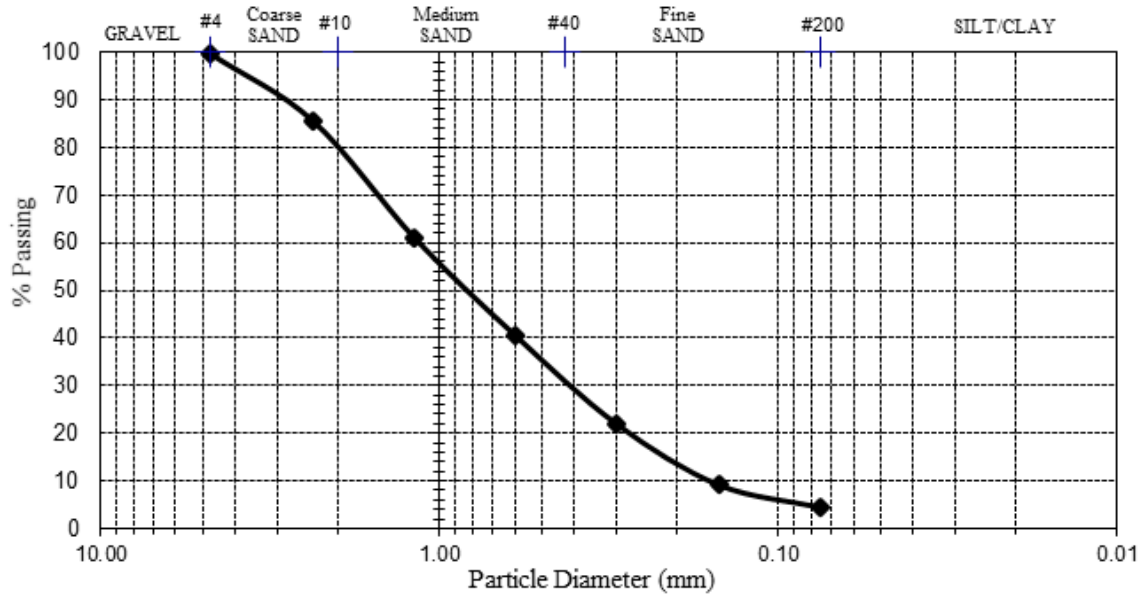


Figure 3-3: Grain size distribution of sand

Soil shear strength parameters

Direct shear (ASTM D3080, 2011) tests were performed on several soil samples to determine the strength parameters of the soil.

Three direct shear tests were performed under a normal stress of 50, 100, 200 kPa. The horizontal feed was kept constant at a rate of 0.30 mm/min. All the soil samples were prepared to match the same unit weight and water content of in situ conditions. Figure 3-4 shows the variation of shear stresses with normal stress during the direct shear tests. The results indicate a friction angle of 48.5° .

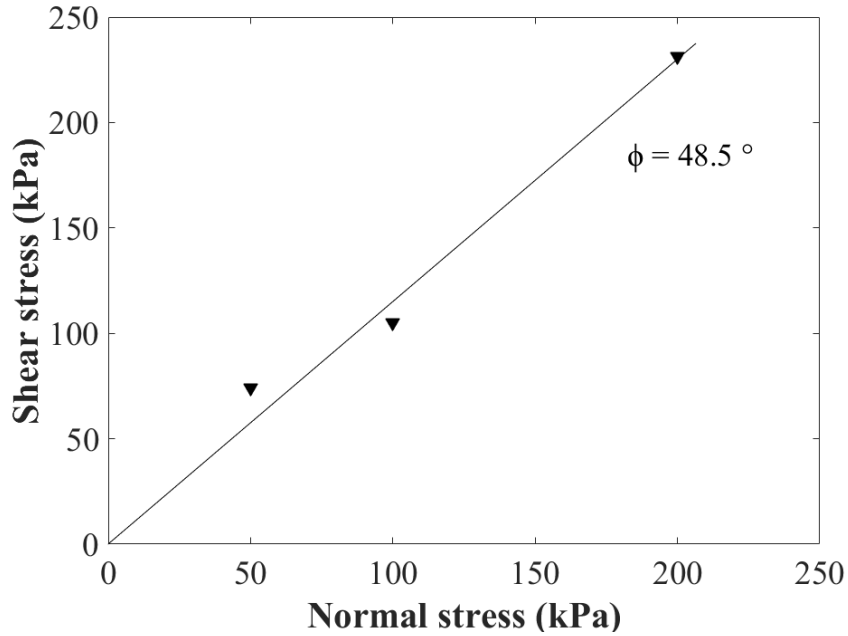


Figure 3-4: Direct shear result – Shear stress vs normal stress

3.2.3.2 In situ tests

The dynamic cone penetration test (DCPT) was carried out on the soil within the laminar shear box. The number of blows per incremental depth (50 mm) were recorded. The DCP penetration index (DPI) is determined using the following equation:

$$DPI = \frac{\text{Incremental Depth}}{\text{Number of blows}} \quad (3.1)$$

De Beer and der Merwe (1991) proposed a correlation between the effective soil modulus and DPI as shown in Figure 3-5. The data points show a slight scatter; however, the confidence limits can aid in providing a rough starting point to estimate the soil modulus with depth that will be used in the numerical modeling (Chapter 5). Also, the DCPT results show that starting from a depth of almost 0.8 meter below the ground surface, the soil DPI, and consequently correlated properties, became constant with depth.

Bowles (1988) suggested the elastic modulus of very dense sand ranges from 45 to 85 MPa. The lower 95th percentile confidence limit was found to be the most reasonable representation of the soil elastic modulus, which also agrees with Bowles (1988). The other

limits correlate to very high moduli values reaching 600 MPa, which seems unreasonable for a 4.57 m soil layer.

Figure 3-6 shows the variation of DPI and correlated effective modulus (95th percentile) with depth in the laminar shear box.

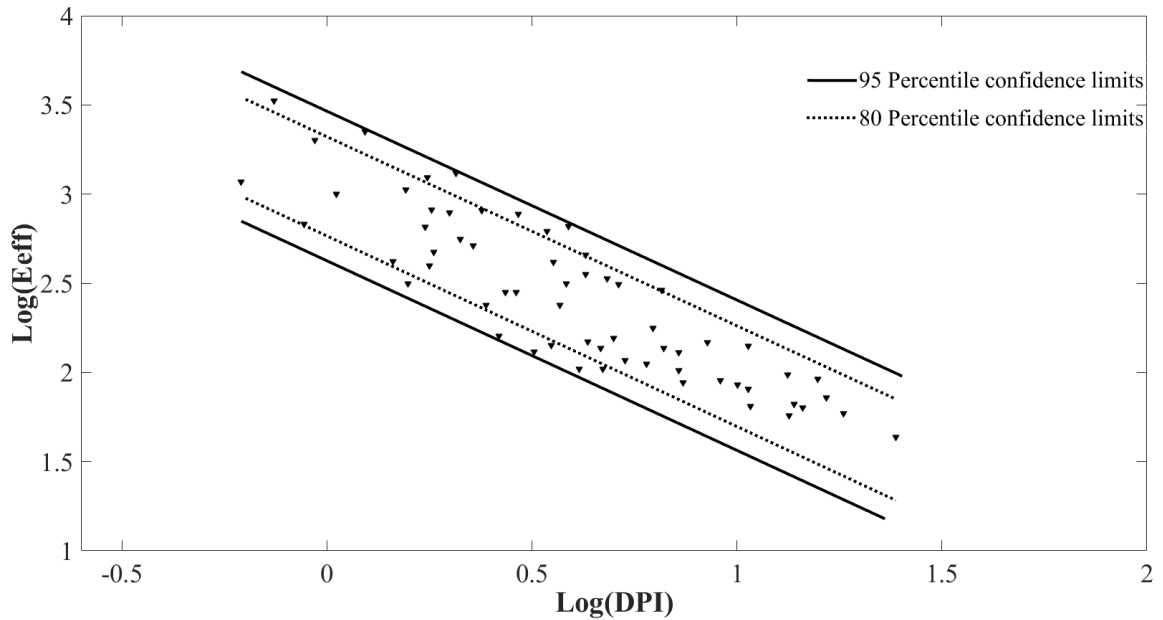


Figure 3-5: DCPT correlation for Effective Modulus (MPa) with DPI (mm/blow) – after De Beer and der Merwe (1991)

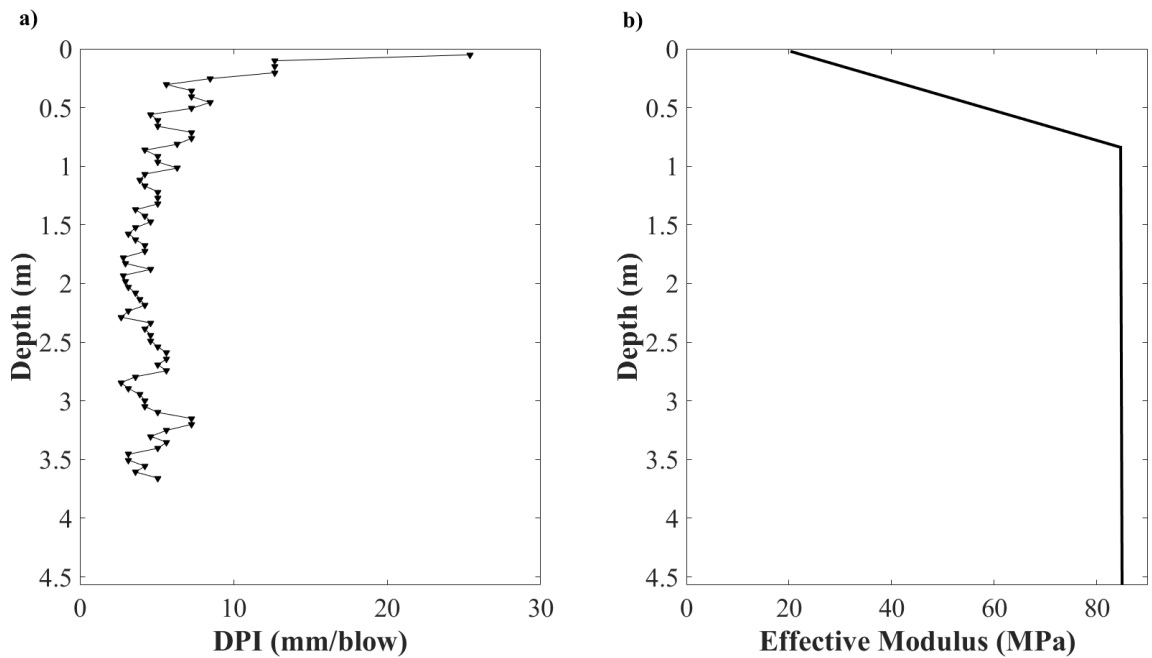


Figure 3-6: DCPT results along laminar shear box depth a) DPI with depth b) Effective modulus from correlation with depth

3.2.4 Test piles: Installation and Instrumentation

Ten steel (A572 Grade 65 & 80) straight piles, nine of which are helical piles, were installed in the soil bed within the laminar shear box. Table 3-1 provides a summary of the geometrical properties of the test piles. The piles were installed in sand contained in the laminar shear box employing the same installation method used in the field (i.e. torquing the piles into the soil by applying a mechanical torque to the pile head). The torque profiles were consistent for piles of the same configuration, as shown in Figure 3-7, which indicates that the soil within the laminar shear box was uniform. They were installed at a minimum spacing centre-to-centre of 1.0 m (i.e. spacing to diameter ratio equal to approximately 12D), as shown in Figure 3-8, to minimise any interaction effects. All piles' lead and extension sections were coupled using a 3-bolt coupling except for Pile 1, which had a threaded coupling.

Twenty blocks of concrete were used to provide mass at the pile heads. The difference in mass applied to the test piles allowed evaluating different dynamic behaviour of the same

pile type. The mass of each concrete block ranged from 340 to 435 kg. The total masses added to each pile are shown in Table 3-2.

Since the shaking was induced in the W-E direction, the strain gauges were placed in that plane at key locations as shown in Figure 3-9 and Figure 3-10 to capture the dynamic behaviour of the piles. Each pile had either six or seven strain gauge elevations, with two opposing strain gauges at each elevation. The strain gauges used were YFLA-5-5LT by Texas measurements Inc. with 120 Ω electrical resistance.

The piles external surfaces, at the locations of the strain gauges, were prepared by first sanding using a 60-grit, followed by a 120-grit, then a 220-grit and finally a 320-grit resulting in a smooth surface suitable for gluing the strain gauge. Before gluing the gauges into place, the gauge locations were cleaned from any oils using a lacquer thinner. To protect the strain gauges, all gauges were coated with a 2 – part epoxy and fiberglass tape. The strain gauges were connected as half-bridges, to minimise the effect of temperature induced measurement errors, with all wiring running inside the pile's shaft through pre-drilled holes. The pre-drilled holes are plugged with silicone to prevent any wire from being damaged. After installation, the strain gauges were checked and only 17% of the strain gauges were damaged. This amount is deemed acceptable and proved the effectiveness of the protection scheme used considering the high frictional stresses developed along the pile's surface during the installation.

To capture soil movement and pile head movement, a total of 33 accelerometers were placed within the soil and one accelerometer on each pile head as shown in Figure 3-11. Two different models (352M54, 355M69) of accelerometers were used and both were special products made to order manufactured by PCB Piezotronics.

The strain gauges and the accelerometers were linked to a compact data acquisition system (DAQ) which consisted of a main chassis of model NI-cDAQ-9188 by National Instruments capable of measuring up to 256 channels. The DAQ recorded the strain gauges and accelerometers with time during the shaking tests, using a minimum of 200 Hz sampling rate.

Table 3-1: Test piles physical properties

Pile ID	Type (<i>Notation</i>)	Length (m)	Helix level (m)	Helix diameter (m)	Outer Diameter / Wall thickness (mm)	Inertia (cm ⁴)	Yield Strength (MPa)
P1	Circular single helical (88-C-1HP)	3.96	-3.40	0.254	88 / 5	119.9	450
P2	Circular single helical (88-C-1HP)	3.66	-3.15	0.254	88 / 5	119.9	450
P3							
P4	Circular double helical (88-C-2HP)	3.66	-2.55 -3.15	0.203 0.254	88 / 5	119.9	450
P5	Driven (88-C- DP)	3.66	---	---	88 / 5	119.9	450
P6	Square single helical (76-S-1HP)	3.66	-3.15	0.254	76 / 5	125.7	415
P7							
P8	Circular helical single (140-C-1HP)	4.27	-3.15	0.254	140 / 10.5	899.1	550
P9							
P10							

*C: circular shaft, 1HP: single helix pile, 2HP: double helix pile, S: square shaft, 88: pile diameter, 140: pile diameter, and 76: length of square side.

Table 3-2: Added masses at each pile head

Pile	Added mass at pile head (kg)
P1	770
P2	750
P3	780
P4	750
P5	370
P6	435
P7	1235
P8	785
P9	700
P10	1245

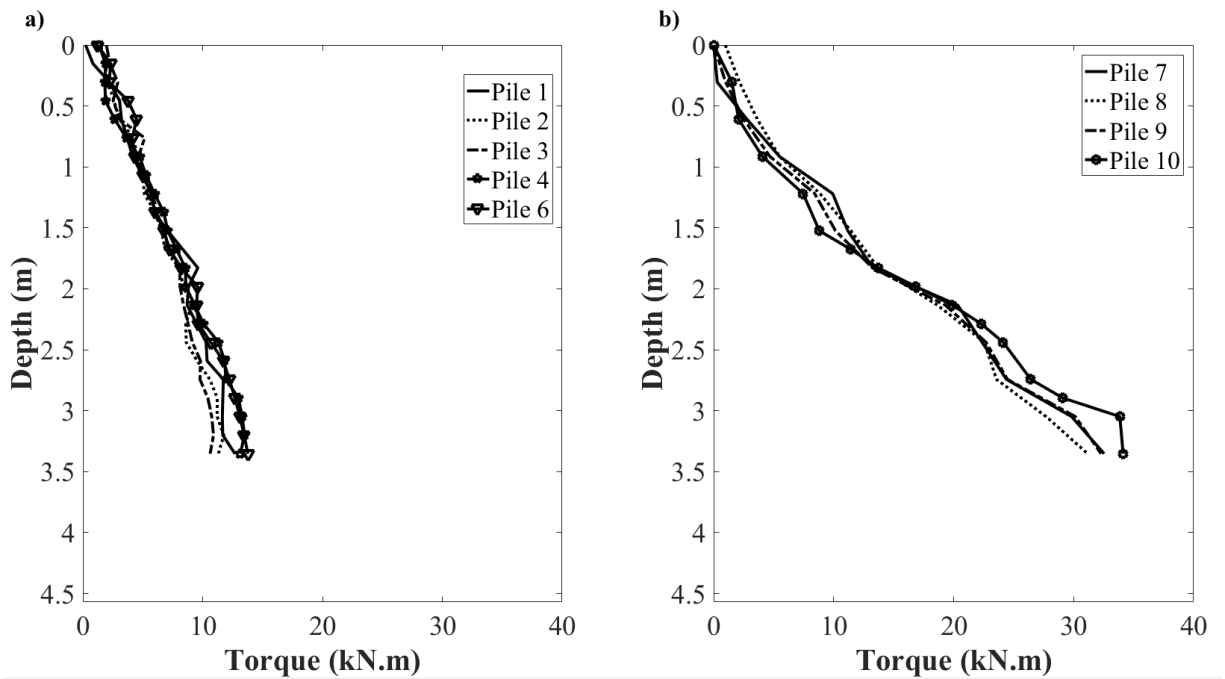


Figure 3-7: Installation torque profiles a) 88 mm diameter helical piles b) 140 mm diameter helical piles

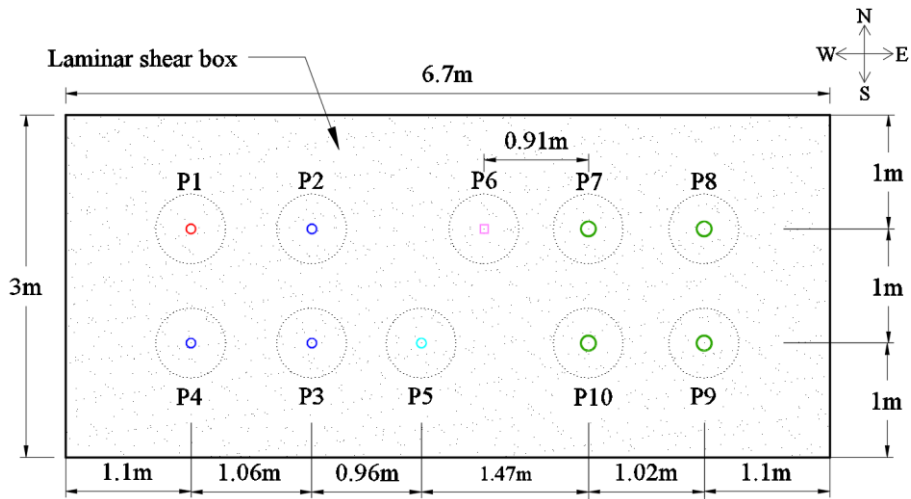


Figure 3-8: Location of each test pile within the laminar shear box

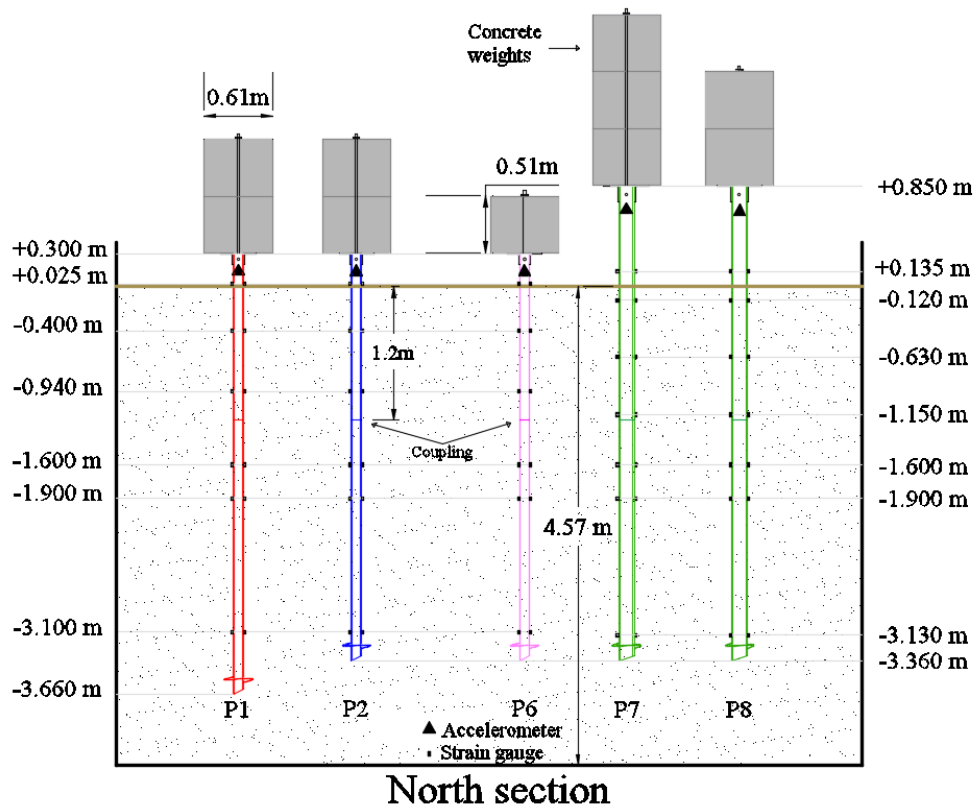


Figure 3-9: North section - Piles instrumentation and elevations

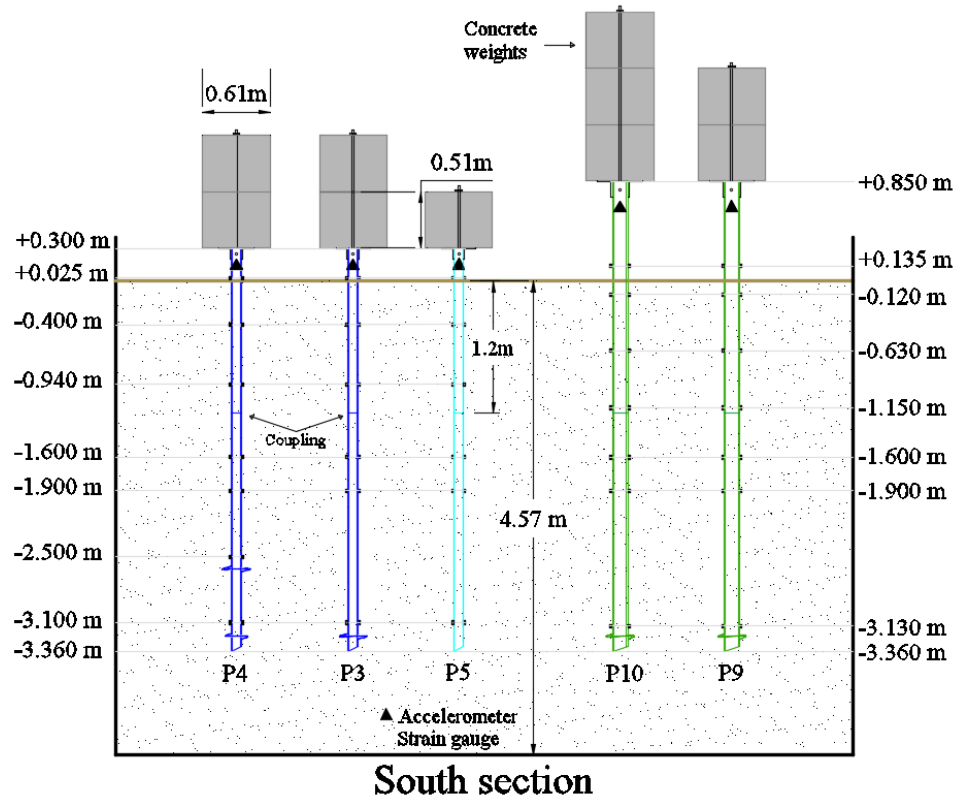


Figure 3-10: South section - Piles instrumentation and elevations

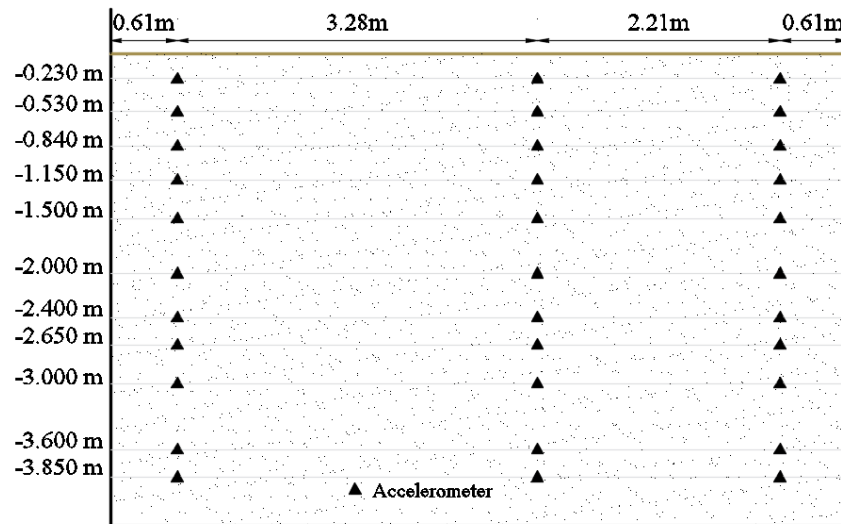


Figure 3-11: Accelerometers locations within soil in laminar shear box

3.2.5 Test program

The seismic loading tests consisted of two different shaking schemes: white noise records and ground motion records.

The white noise was a random signal with a constant intensity for a range of frequencies. The intensity or peak acceleration was chosen in such a way that it produced just enough movement and deformation to be recorded by sensors without resulting in non-linear behaviour in the soil or pile. The white noise signal used in this test had a bandwidth of 0 – 40 Hz and root mean square (RMS) amplitude value of 0.07g.

The ground motion records used were: Northridge (1994) earthquake recorded at Fire station 108, USC station 5314, California, United States and the Kobe (1995) earthquake recorded at Takatori station, Takatori, Japan (hereby named Northridge and Takatori). In addition to the two original earthquake time histories, the accelerations of each earthquake were scaled to 75% and 50% as shown in Table 3-3, in order to evaluate the range of pile responses from linear to nonlinear. Figure 3-12, Figure 3-13 and Figure 3-14 present information (acceleration time history, frequency content and spectral accelerations) regarding the original earthquake records. As can be noted from Figure 3-13, the energy content of Northridge record was spread over a wide range of frequency (i.e. 1 Hz – 5.0 Hz) while Takatori record's energy content was concentrated within the range 0.5 Hz to 1.5 Hz.

Table 3-3: Test program earthquake intensities

Earthquake	Intensity relative to unscaled (%)	Absolute peak acceleration (g)
1) Northridge	100	0.50
2) Northridge	75	0.37
3) Northridge	50	0.25
4) Takatori	100	0.67
5) Takatori	75	0.50
6) Takatori	50	0.33

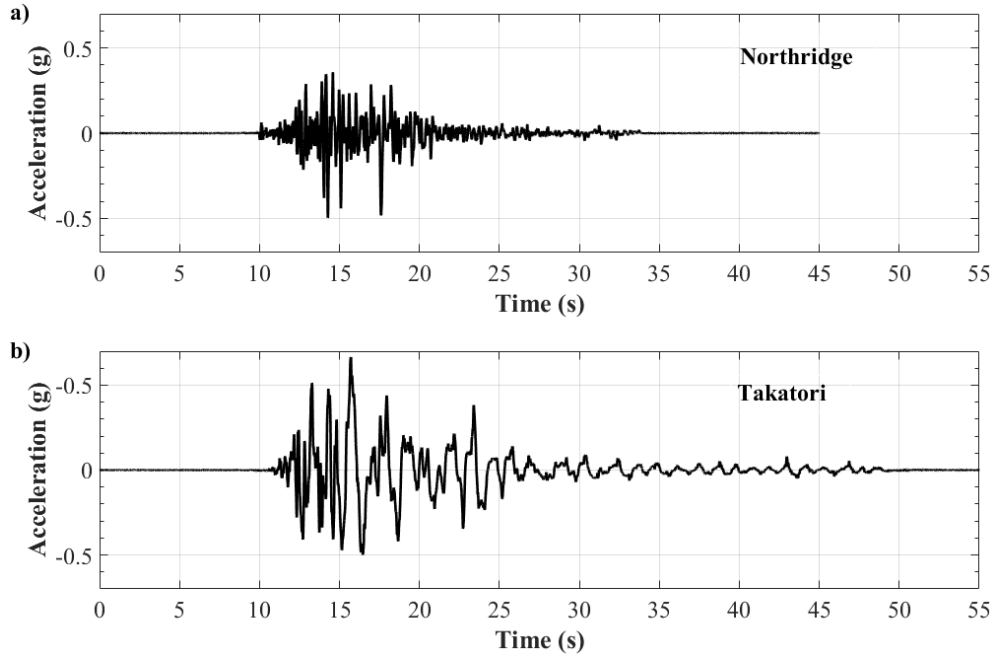


Figure 3-12: Unscaled Earthquake time records a) Northridge b) Takatori

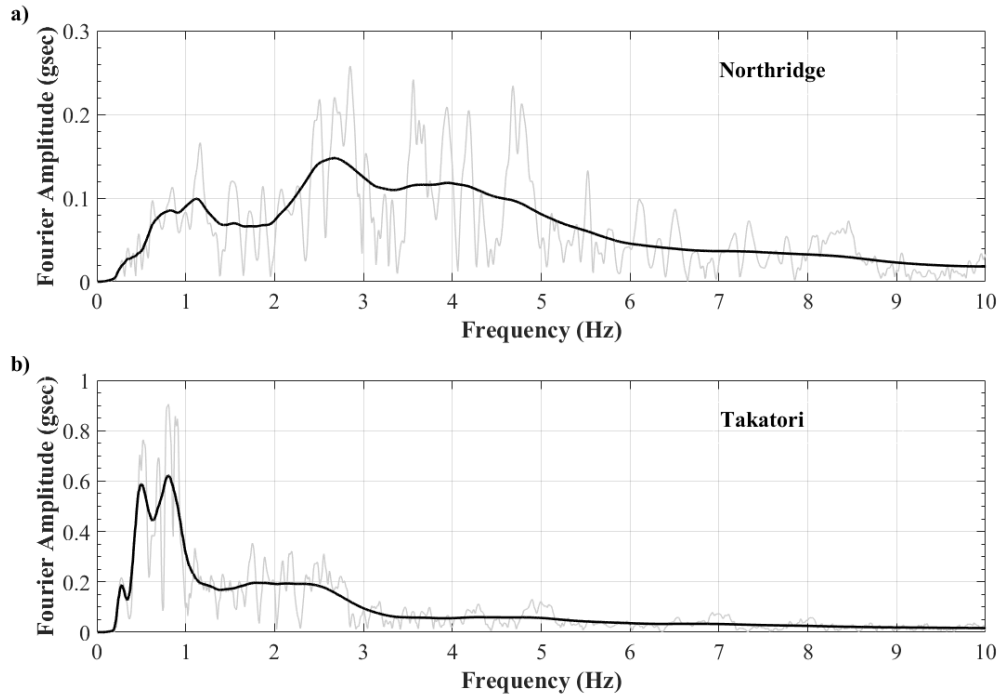


Figure 3-13: Fourier Analysis of earthquake records a) Northridge b) Takatori

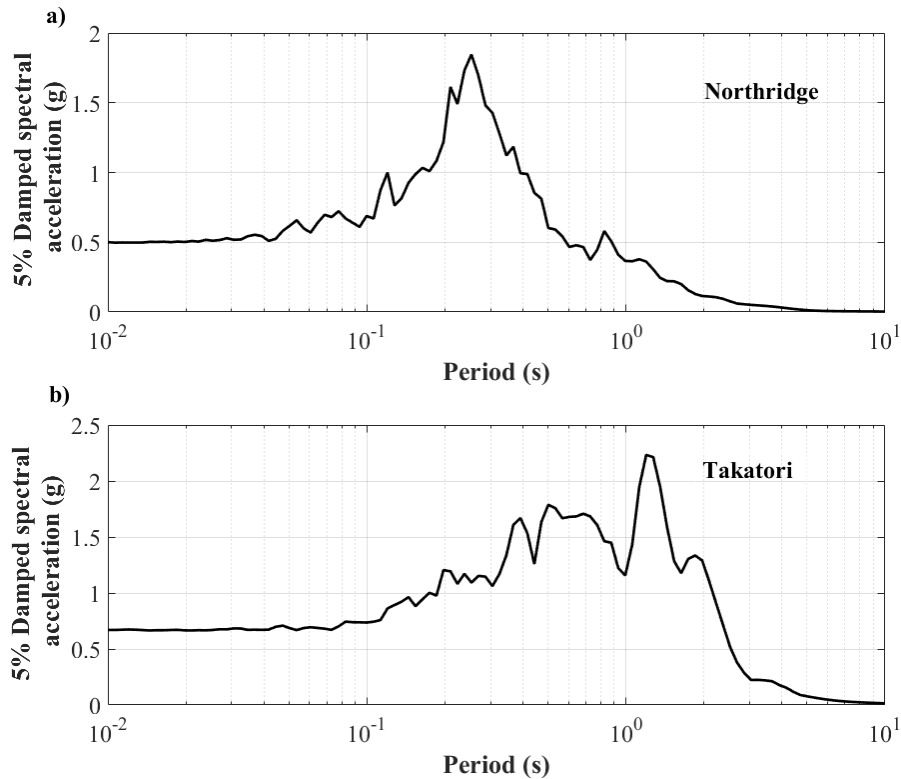


Figure 3-14: 5% Damped spectral acceleration (response spectrum) for earthquake records a) Northridge b) Takatori

3.3 Data preparation

3.3.1 Data filtering

Strain gauges and accelerometers are sensitive to fluctuations in electric signal and often display high-frequency noise; therefore, filtering of raw data was performed to remove the noise from strain gauge readings employing the band pass 4th degree Butterworth filter. The Butterworth filter was deemed most suitable as it has the flattest magnitude filter. The band pass was performed between 0.25 to 8 Hz to ensure no earthquake signal was lost and all high frequency noise was removed.

3.3.2 Data interpretation

Straining actions occurring in piles during shaking can be captured using different instrumentation types. Strain gauges provide a reliable and inexpensive method to record

varying strains with time during a dynamic test; however, they only measure strains at discrete points along the pile. Therefore, a curve fitting method must be employed to establish the straining actions pattern along the entire length of the pile. The bending moment at each strain gauge elevation at a certain time step is given by:

$$M(z) = \frac{E_p I_p (\varepsilon_1 - \varepsilon_2)}{D} \quad (3.2)$$

Where $\varepsilon_1, \varepsilon_2$ are the strain gauge readings at opposite sides of the pile cross-section at the specified elevation and D is the pile outer diameter.

The soil reactions to the pile movement during lateral loading can be expressed through the p-y curve approach. In this approach, the soil resistance is represented by discrete springs and dashpots attached to the pile along its shaft as shown in Figure 3-15.

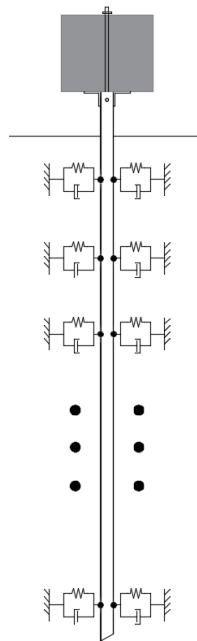


Figure 3-15: General p-y curve approach

The spring force-deformation relationship can be represented by the p-y curves obtained from results of lateral load tests on instrumented piles. The soil reaction (p) and the pile lateral deflection relative to the tip of the pile (y_{pile}) can be obtained by double differentiation and double integration, respectively, of the bending moment function, i.e.:

$$p(z) = \frac{d^2 M(z)}{dz^2} \quad (3.3)$$

$$y_{pile}(z) = \iint \frac{M(z)}{E_p I_p} dz \quad (3.4)$$

Where $M(z)$ is the pile bending moment at depth z ; and E_p, I_p are the elastic modulus of pile material and its cross-sectional moment of inertia. The soil pressure computed from Equation (3.3) does not include the dynamic pressure due to the inertial component of the pile. However, (Ting, 1987) has reasoned that the inertial component is negligible when compared to the component resulting from the beam theory and therefore can be ignored. The calculations given by Equations (3.3) and (3.4) are performed at every time step to compute the full time histories of p and y_{pile} during the shaking.

Unlike static p - y curves, the dynamic p - y curves include the far-field soil movement relative to the base. The general form of the y component of the p - y curves can be expressed

$$y = y_{pile} - y_{soil} \quad (3.5)$$

where y_{pile} is obtained from Equation (3.4) and y_{soil} is the far-field soil movement, y is the displacement of the pile relative to the far-field soil. In the case of static loading, the y_{soil} is equal to zero; while it is obtained from accelerometer readings during dynamic loading or by performing ground response analysis. In this study, the far-field soil movement is obtained by linear analysis performed in DEEPSOIL (Hashash et al., 2016).

3.3.3 Curve fitting

Since the number of strain gauges along each pile, and hence known strain and bending moment locations, is limited, a numerical curve fitting procedure must be performed to digitize the full bending moment profile. There are various curve fitting procedures available in the literature that can be used for this purpose. Two general procedures were utilized herein: *global polynomials* and *splines* (Spline of order 3 represents a Cubic spline, order 4 represents a Quartic spline and order 5 represents a Quintic spline). There are two types of curve fitting, interpolation and approximation. For interpolation, the resulting curve must pass through all data points; while the curve in approximation should satisfy the minimum least-squares error depending on the weight assigned to each data point.

Global polynomial approximation (4th to 9th degree) was used by (Ting, 1987; Springman, 1989; Bouafia and Garnier, 1991; King, 1994; Kitazume, 1994; Ilyas et al., 2004; Kong and Zhang, 2007; Jeanjean, 2009; Klinkvort, 2012; Choo and Kim, 2015). *Cubic spline interpolation and/or approximation* was used by (Barton, 1982; King, 1994; Jeanjean, 2009; Lau, 2015; Haiderali and Madabhushi, 2016). *Quartic spline interpolation and/or approximation* was used by King (1994) and *Quintic spline interpolation and/or approximation* was used by (Bouafia and Garnier, 1991; Mezazigh and Levacher, 1998; Remaud et al., 1998; Bouafia and Bouguerra, 2006). The procedure used for curve fitting is important, especially for the calculation of soil reaction profiles as a small deviation in the curvature of the fitted moment profile curve can be magnified through the double differentiation. The inconsistency in curve fitting methods used by different researchers is probably due to the relative sensitivity of the different curve fitting methods to the amount and locations of data points (strain gauge readings) available in the experimental setup and/or expected behaviour of a pile. Therefore, a study was performed to evaluate the different curve fitting methods for this specific experimental setup. In addition to this qualitative comparison, a quantitative comparison was performed to rank the methods.

In order to enforce the boundary conditions for the curve fitting profile, several artificial points were added. The center of mass at the pile head was assumed to have zero bending moment. Two artificial points were added close to the pile tip and assigned zero moment to ensure the boundary condition of zero curvature and zero change in curvature at the bottom of the pile. Three additional points were added at the surface (i.e. at -0.01, 0 and +0.01 m) to ensure the slope of the fitted moment profile matched the known shear value back calculated from the top strain gauge readings above the ground surface. All artificial points were given a weight value of 1000 to ensure the resulting fitted moment curve passes through them. The numerical integration was conducted following a bottom-up integration using the boundary condition of zero rotation and deflection at the pile tip.

3.3.3.1 Curve fitting study using LPILE

Simple pile lateral response analyses were conducted employing the computer code LPILE (Ensoft Inc., 2011) to generate moment profiles for two pile configurations, defined by number of discrete strain gauges (Table 3-4). These analyses did not account for the error

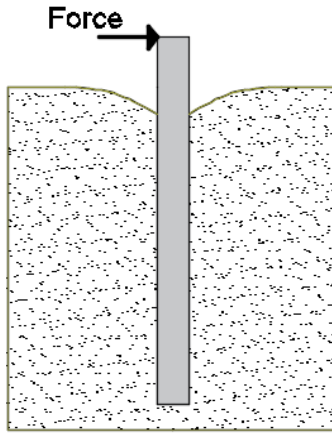
in strain gauge readings; however, they provided a general pattern for the expected bending moment profile in order to evaluate what curve fitting methods produce results that suit the pile configurations used and to assess whether the amount of strain gauge readings used is sufficient.

Table 3-4: Configurations for LPILE models

Configuration	Piles	Total number of strain gauges
1	1,2,3,5,6	6
2	4,7,8,9,10	7

For each configuration, a pile with the same properties embedded in clean sand with $\phi = 49^\circ$ and $\gamma = 19.5 \text{ kN/m}^3$ was modelled. A lateral load was applied at the pile head at the same location as the center of the concrete masses used in the test. After the full bending moment profile was evaluated using LPILE, discrete points were extracted at the same locations of the strain gauges. These points would represent the “experimental” strain gauge readings and would be used to further test the global polynomial and spline curve fitting methods. The resulting fitted moment profile from each method was then compared with the moment profile generated from the LPILE analysis. The pile deflection and soil reaction profiles generated from the double integration and double differentiation, respectively, of the fitted moment profiles for each method were also compared with the profiles generated from LPILE. A diagram summarising the curve fitting procedure is shown in Figure 3-16.

Scripts were developed using MATLAB (MathWorks, 2016) to facilitate the procedure of curve fitting, numerical double integration and numerical double differentiation.



LPILE OUTPUT

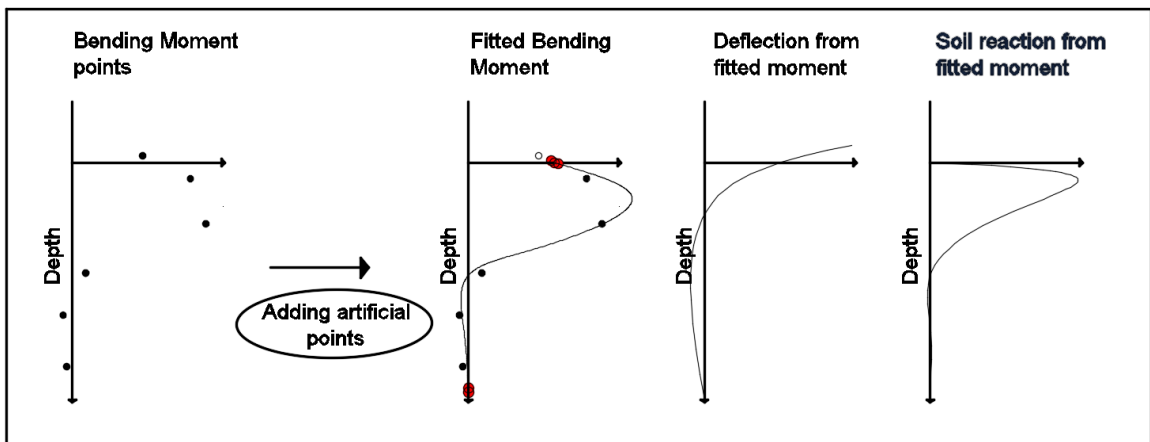
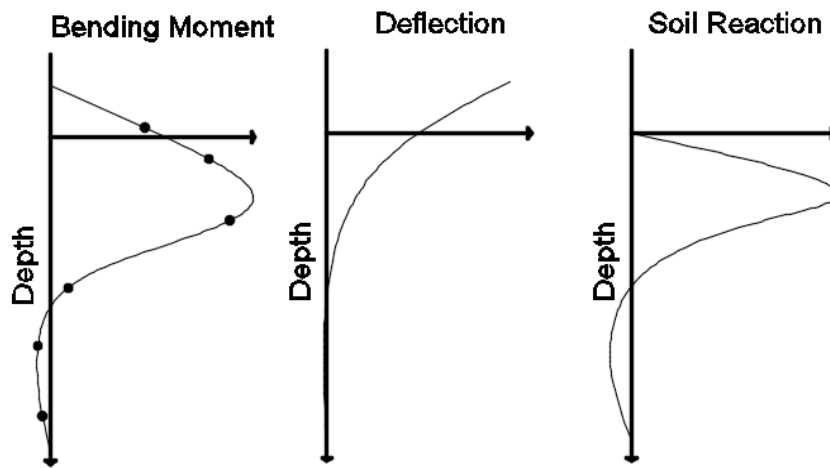


Figure 3-16: Curve fitting procedure

3.3.3.2 Qualitative comparison

Global polynomials method

All global polynomials were fitted by the least squares approximation technique. Global polynomials are mathematically represented as:

$$M(z) = a_n z^n + a_{(n-1)} z^{(n-1)} + \dots + a_1 z + a_0; \quad z \in [\text{pile length}] \quad (3.6)$$

where $a_n, a_{(n-1)} \dots a_1, a_0$ are unknown polynomial coefficients of a nth degree polynomial.

Performance of polynomials starting from the 4th degree to the 9th degree were evaluated for both configurations. None of the polynomial functions provided good results for the deflection (y) profile and only the 9th degree polynomial provided good results for the soil reaction (p) profile. Increased deflection errors were observed resulting from numerical integration of the oscillating areas near the pile tip. This is a common problem with all high degree global polynomials, known as the Runge's phenomenon, which was also noted by Haiderali and Madabhushi (2016). This phenomenon occurs as the high degree polynomial fit reaches the pile tip and is unable to decay properly and starts oscillating. For this reason, global polynomials were not used herein, and rather, the analysis proceeded utilizing splines (piecewise polynomials). Figure 3-17 illustrates Runge's phenomenon in high degree global polynomials.

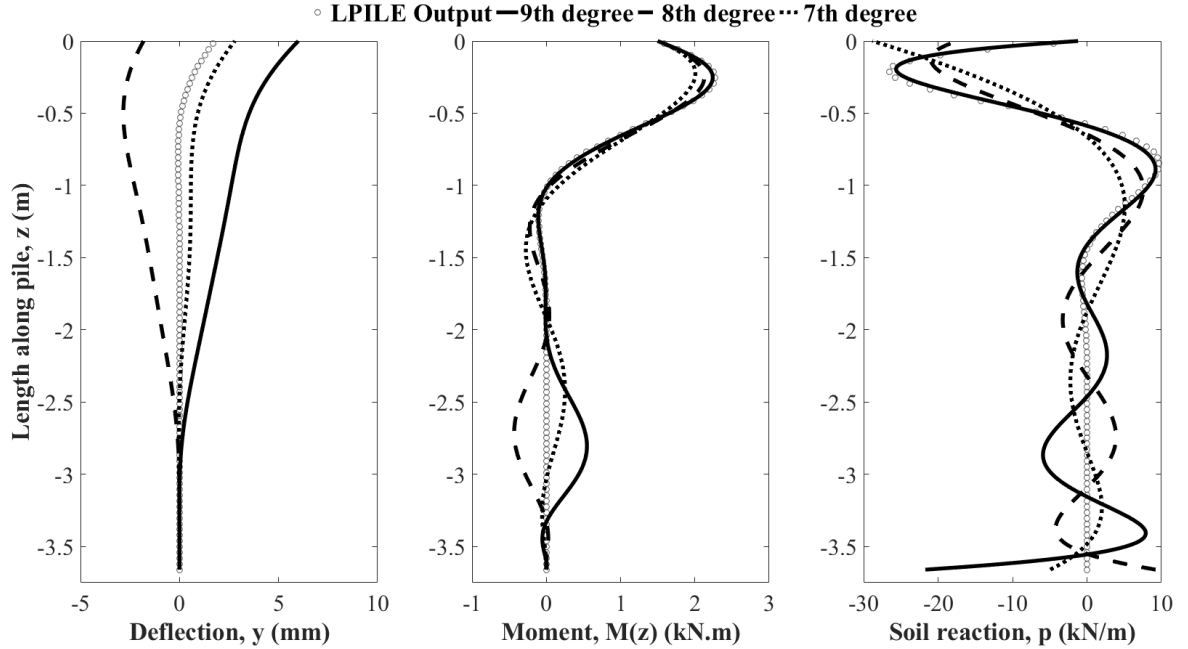


Figure 3-17: High degree global polynomial fit for Configuration 1 (Piles with 6 strain gauges)

Splines method

There are two common forms of splines: piecewise polynomial form (ppform) and B-form. What greatly affects the formulation of a spline is the selection of the number of knots and their locations. Knot locations are where the pieces of the spline connect. All splines are continuous across their first and second derivative. The mathematical representation of a spline in the ppform with breaks at $\xi_1, \xi_2, \dots, \xi_{l+1}$ may be given by:

$$M(z) = \sum_{i=1}^k c_{ji} (z - \xi_j)^{k-i} \quad ; j \in [1, l] \quad (3.7)$$

where k is the spline order, l the number of pieces, c_{ji} the unknown spline coefficient.

Since splines give the capability of breaking the curve fitted function into several pieces, they are able to capture the decay as the moment reaches the pile tip and generally provides a better fit than global polynomials. Haiderali and Madabhushi (2016) discussed the knot number and locations, and used interpolation splines with knot locations determined by the acceptable knot sequence algorithm available in MATLAB for interpolation splines. The acceptable knot sequence algorithm is unreliable, especially when dealing with a large

number of dynamic readings. For approximation splines, the user specifies the knot number and locations. As the number of knots increases, the approximation spline approaches the results in a curve fitting solution similar to that of interpolation splines. Through inspecting several curve fitting data in the test, it was found that two interior knots provide the best and smoothest fit for approximation splines. The locations of the knots were optimized using a code developed by the author, which was tailored for this test. Due to the enormous amount of data and curve fitting trials, only cubic splines are shown in Figure 3-18 and Figure 3-19 for both configurations to illustrate the difference in the performance of cubic spline approximation and interpolation.

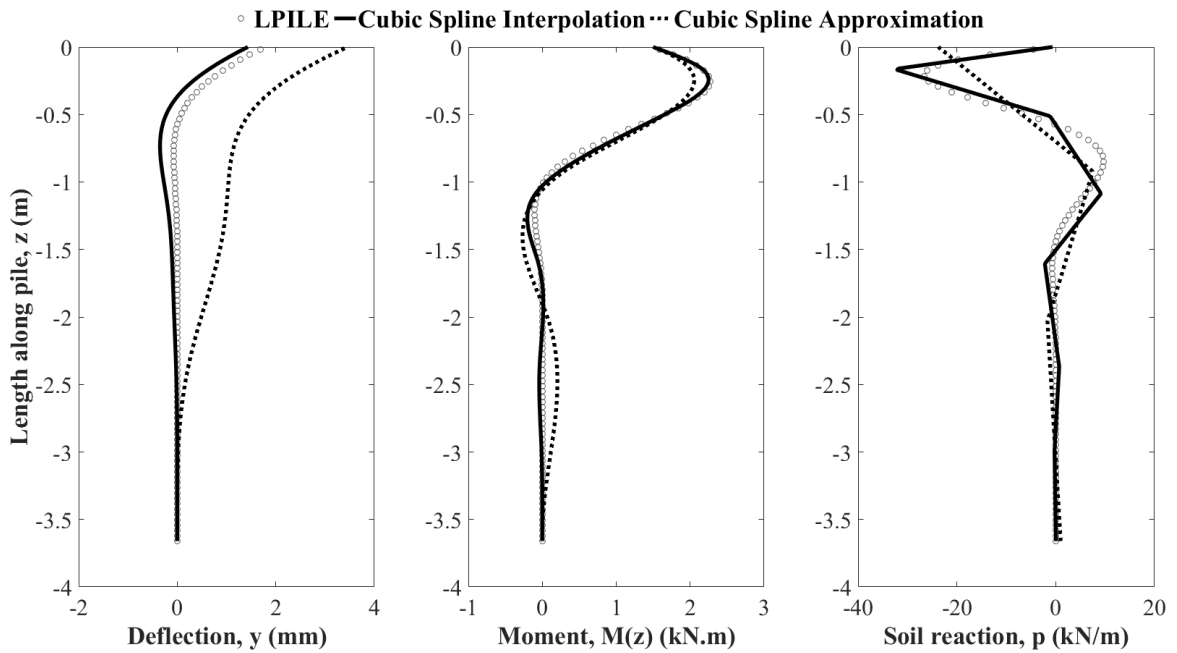


Figure 3-18: Cubic interpolation and approximate splines for Configuration 1 (Piles with 6 strain gauges)

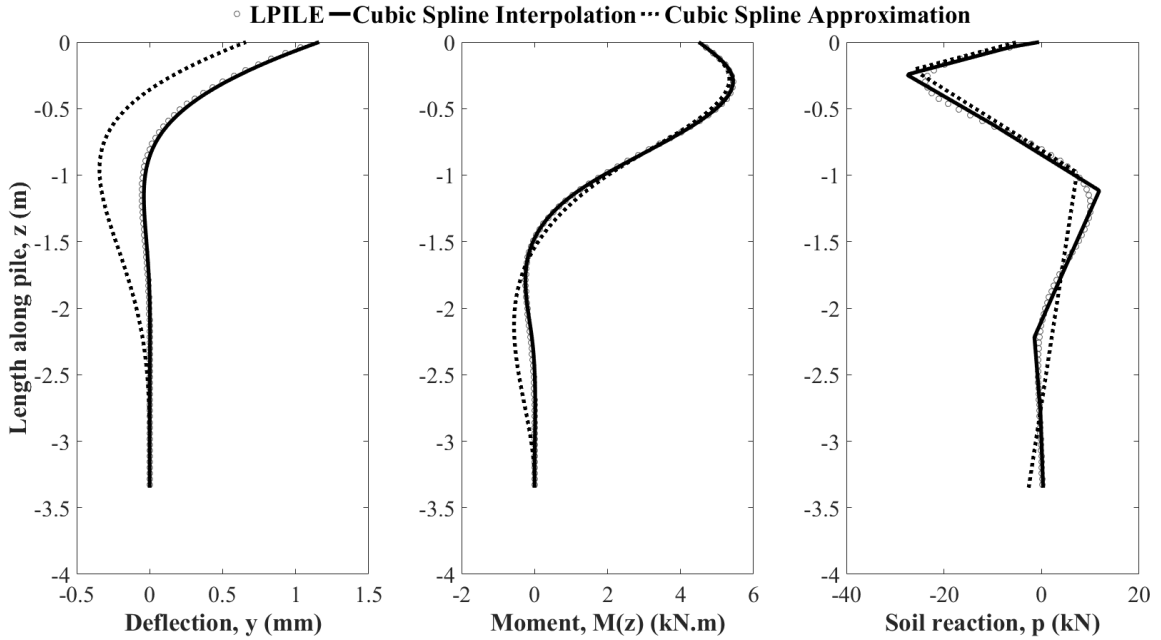


Figure 3-19: Cubic interpolation and approximate spline in Configuration 2 (Piles with 7 strain gauges)

3.3.3.3 Quantitative comparison

As can be seen visually from Figure 3-18 and Figure 3-19, the cubic spline interpolation conformed to the original idealized LPILE moment curves much better than the cubic approximation method. However, interpolation splines are generally avoided due to the fact that the fitted curve is forced to pass through all points, which may lead to unexpected jumps in curvature between two data points due to experimental error. This change in curvature is significant when it comes to calculating the soil reaction profile but only has a small effect on the deflection profile (Ting, 1987). This phenomenon was not seen in the idealized curve fitting study performed herein as the data were extracted from LPILE analyses and contained no experimental errors. During dynamic testing, however, small errors in strain gauges may cause a jump in curvature of the fitted moment curve. By using approximation splines, small errors in data will not cause jumps in the curvature of the fitted moment curve.

Table 3-5 and Table 3-6 compare the goodness of fit for pile configurations 1 and 2, respectively. The goodness of fit is judged by the error calculated as follows:

$$Error = \sum_{i=1}^N (fitted_i - LPILE_i)^2 \quad i = 1, 2, \dots, N \quad (3.8)$$

Where *Fitted* is the value determined from the curve fitting method (deflection or soil reaction), *LPILE* is the theoretical value obtained from LPILE (deflection or soil reaction), N is 100 which represents the number of points.

As can be noted from Table 3-5 and Table 3-6, the Quintic spline interpolation provided the best results for deflections (y) for both configurations. Therefore, it will be used to estimate deflection (y) for all piles in this test. In addition, the quintic interpolation splines and 9th degree global polynomial outperformed the cubic, quartic and quintic approximation splines in both configurations for the soil reaction (p) profile but they will be discarded since interpolation splines may lead to unexpected jumps in curvature between two data points and the 9th global polynomial suffers from the Runge's phenomenon. Therefore, quartic spline approximation and cubic spline approximation were used for Configuration 1 piles and Configuration 2 piles, respectively, to calculate the soil reaction (p) profile.

Table 3-5: Configuration 1 ranking methods for deflection and soil reaction

Rank of methods for Deflection (y)	Rank of methods for Soil reaction (p)
1. Quintic spline interp.	1. Quintic spline interp.
2. Cubic spline interp.	2. 9 th global polynomial
3. Quartic spline interp.	3. Quartic spline interp.
4. Cubic spline approx.	4. Quartic spline approx.

Table 3-6: Configuration 2 ranking of methods for deflection and soil reaction

Rank of methods for Deflection (y)	Rank of methods for Soil reaction (p)
1. Quintic spline interp.	1. Quintic spline interp.
2. Quartic spline interp.	2. 9 th global polynomial
3. Cubic spline interp.	3. Cubic spline interp.
4. Quintic spline approx.	4. Cubic spline approx.

3.4 Conclusions

Ten steel piles were installed in a laminar soil shear box filled with dry sand. The test piles include single circular helical piles, double circular helical pile, a single square helical pile and a circular driven pile. To characterise the soil; different laboratory and in situ tests are performed on several soil samples. Finally, a comparison of different curve fitting methods is performed. Based on the results, the main conclusions are as follows:

1. The DCPT results showed that the soil properties become constant at a depth of approximately 0.8 m. The DCPT results are correlated with the elastic modulus (Figure 3-6) to provide initial starting values for the numerical modeling (Chapter 5). The direct shear test indicates a friction angle of 48.5° , which will also be used in the numerical modeling.
2. The installation torque profiles (Figure 3-7) demonstrate that the soil within the laminar shear box is uniform.
3. The instrumentation scheme used provided sufficient and reliable data to evaluate the seismic behaviour of the test piles.
4. The performance of curve fitting methods heavily depends on the test/instrumentation setup used (amount of strain gauges, spacing of strain gauges, rigid or flexible pile etc.). It is recommended to perform a simplified analysis for the test setup before developing the instrumentation plan to ensure the number and spacing of strain gauges used are sufficient to produce accurate results.

5. The quintic spline interpolation curve fitting method provided the best deflection (y) results for the specific test/instrumentation setup used herein, while quartic and cubic spline approximation curve fitting methods provided the best soil reaction (p) results for configuration 1 (6 strain gauge locations) and configuration 2 (7 strain gauge locations), respectively.

3.5 References

- Barton, Y.O. 1982. Laterally loaded model piles in sand: Centrifuge tests and finite element analyses. University of Cambridge.
- De Beer, M., and der Merwe, C.J. 1991. Use of the Dynamic Cone Penetrometer (DCP) in the design of road structures. Pavement Engineering Technology, Division of Roads and Transport Technology.
- Bouafia, A., and Bouguerra, A. 2006. Single piles under lateral loads—centrifuge modelling of some particular aspects. In Proceedings of the international conference on physical modelling in Geotechnics. pp. 915–920.
- Bouafia, A., and Garnier, J. 1991. Experimental study of PY curves for piles in sand. In Proceedings of the international conference Centrifuge. pp. 261–268.
- Bowles, J.E. 1988. Foundation analysis and design.
- Choo, Y.W., and Kim, D. 2015. Experimental Development of the p-y Relationship for Large-Diameter Offshore Monopiles in Sands: Centrifuge Tests. Journal of Geotechnical and Geoenvironmental Engineering, 142(1): 4015058. American Society of Civil Engineers.
- Ensoft Inc. 2011. LPILE v6.0: A program for the analysis of piles and drilled shafts under lateral loads. Ensoft Inc., Austin, Texas.
- Haiderali, A.E., and Madabhushi, G. 2016. Evaluation of Curve Fitting Techniques in Deriving p--y Curves for Laterally Loaded Piles. Geotechnical and Geological Engineering, 34(5): 1453–1473.
- Hashash, Y.M.A., Musgrove, M.I., Harmon, J.A., Groholski, D., Phillips, C.A., and Park, D. 2016. DEEPSOIL V6.1, User Manual. Board of Trustees of University of Illinois at Urbana-Champaign, Urbana, IL.
- Ilyas, T., Leung, C., Chow, Y., and Budi, S. 2004. Centrifuge model study of laterally loaded pile groups in clay. Journal of Geotechnical and Geoenvironmental Engineering, 130(3): 274–283.
- Ishihara, K., Kagawa, T., Ogawa, N., Minowa, C., and Sakai, K. 1996. Design of large-scale liquefaction experiment facility. In Proc., 31st Japanese National Conf. on Geotechnical Engineering. pp. 1189–1190.
- Jeanjean, P. 2009. Re-assessment of py curves for soft clays from centrifuge testing and finite element modeling. In Offshore Technology Conference.

- King, G.J.W. 1994. The interpretation of data from tests on laterally loaded piles. In Proceedings of the international conference Centrifuge. pp. 515–520.
- Kitazume, M. 1994. Lateral resistance of long pile in soft clay. In Proc. of the International Conference Centrifuge 94. pp. 485–490.
- Klinkvort, R. 2012. Centrifuge modelling of drained lateral pile–soil response: application for offshore wind turbine support structures. Technical University of Denmark.
- Kong, L.G., and Zhang, L.M. 2007. Rate-controlled lateral-load pile tests using a robotic manipulator in centrifuge. *Geotechnical Testing Journal*, 30(3): 192–201. ASTM International.
- Lau, B.H. 2015. Cyclic behaviour of Monopile foundations for offshore wind turbines in clay. University of Cambridge.
- Mezazigh, S., and Levacher, D. 1998. Laterally loaded piles in sand: slope effect on py reaction curves. *Canadian geotechnical journal*, 35(3): 433–441.
- NERHI @ UC San Diego. (n.d.). Available from <http://nees.ucsd.edu/> [accessed 13 August 2017].
- Remaud, D., Garnier, J., and Frank, R. 1998. Laterally loaded piles in dense sand: Group effects. In *Int. Conf. Centrifuge 98*. pp. 533–538.
- Springman, S. 1989. Lateral loading on piles due to simulated embankment construction. University of Cambridge.
- Standard Test Method for Sieve Analysis of Fine and Coarse Aggregates. 2014. ASTM International.
- Standard Test Method for Direct Shear Test of Soils Under Consolidated Drained Conditions. 2011. ASTM International.
- the MathWorks, I. 2016. MATLAB and Statistics Toolbox. the Mathworks, Inc., Massachusetts, United States.
- Ting, J.M. 1987. Full-Scale Cyclic Dynamic Lateral Pile Responses. *Journal of Geotechnical Engineering*, 113(1): 30–45. doi:10.1061/(ASCE)0733-9410(1987)113:1(30).

EXPERIMENTAL RESULTS

The results of the full-scale shaking table testing program are presented and discussed in terms of natural frequency and response of the test piles. In addition, the effect of pile installation method, number of helices, pile shaft shape and diameter on its natural frequency are assessed. Finally, the effects of seismic loading characteristics (i.e. intensity and frequency) as well as the geometrical properties of the piles on their seismic response were evaluated. The piles responses are shown in terms of peak deflections or bending moment and dynamic p-y curves.

4.1 Natural frequencies of Soil-Pile system

The response of test piles to white noise records can be used to evaluate the natural frequencies of the soil-pile system. The response of each pile was measured using two methods: strain gauge readings along its length and accelerometer readings at the pile's head. The pile's natural frequency was obtained by performing a **Fast Fourier Transform** (FFT) of the measured response time history. These results assist in further understanding the piles' response to ground motions with different frequency content. For example, Figure 4-1 compares the Fourier spectra obtained from strain gauge and accelerometer readings for piles P1 (88-C-1HP) and P4 (88-C-2HP). As noted from Figure 4-1, each Fourier spectrum displays two peaks; the first peak corresponds to the natural frequency of the horizontal degree of freedom (1st mode) of the soil-pile system, while the second peak corresponds to the natural frequency of the rotational degree of freedom (2nd mode). Both the first and second peaks are matching when evaluated from either source. However, the second mode is more pronounced in the accelerometer Fourier spectra due to the higher rotation at the location of the accelerometer (located on top of the concrete mass). Since the horizontal mode is the focus of this study, the strain gauge readings will be used for assessing the natural frequency of the piles.

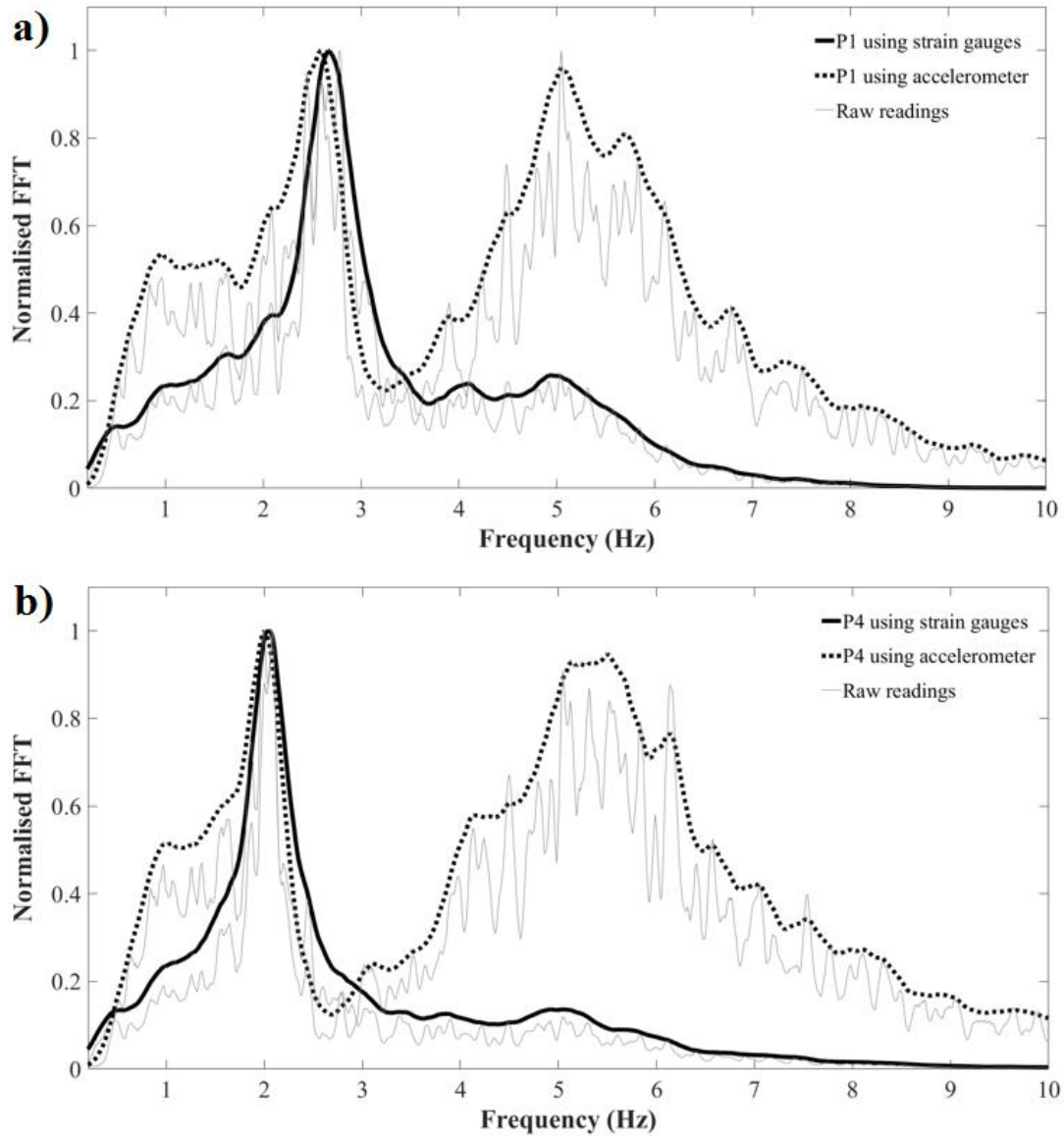


Figure 4-1: Fourier spectra using response from strain gauges and accelerometer readings a) P1 (88-C-1HP) b) P2 (88-C-2HP)

4.1.1 Effect of soil disturbance during installation

As the pile's helix advances through the soil during installation, it causes soil disturbance due to the shearing effect within a cylindrical zone around the pile. Trofimenkov and Mariupolskii (1965) demonstrated the effect of disturbance in single helical piles by examining the difference in uplift and compressive capacities in both sand and clay. Kulhawy (1985) and Mitsch and Clemence (1985) suggested that helical piles cause

significant disturbance in the soil around the pile. Sakr (2009) conducted full-scale static load tests on single and multi-helix piles and the results demonstrated that the soil disturbance was slightly higher for the case of multi-helix piles, which resulted in slightly reduced lateral resistance of the multi-helix pile compared to the single helix pile due to the increased disturbance in the soil. Lutenegger et al. (2014) used field vane tests to show that the degree of disturbance caused by a multi-helix pile is greater than a single helix pile. Bagheri and El Naggar (2015) indicated that the behaviour of multi-helix piles is greatly affected by the disturbance caused by the helices during installation, which leads to a reduction in the friction angle especially in dense sands.

The effect of soil disturbance can be evaluated from the stiffness (or frequency) variation of the tested piles. Figure 4-2 presents Fourier spectra of the responses of a single helix pile (88-C-1HP) and a double helix pile (88-C-2HP) to white noise excitation. As noted from Figure 4-2, the double-helix pile has slightly lower natural frequency compared to the single-helix pile with same geometric properties (flexural stiffness) and pile head mass, which indicates that the soil disturbance is somewhat higher due to the second helix. Similarly, Figure 4-3 compares the Fourier spectra of the responses of a helical pile (88-C-1HP) and a driven pile (88-C-DP) with same geometric properties (flexural stiffness) to white noise excitations. As can be noted from Figure 4-3, there is a pronounced difference between the natural frequencies of the helical and driven piles. However, it should be noted that the mass attached to the helical pile head was almost double the mass attached to the driven pile head; therefore, the mass effect must be taken into account when comparing the natural frequencies of the two piles, i.e.:

$$f_{soil-pile} = \sqrt{\frac{k}{m}} \quad (4.1)$$

where k is the stiffness of the soil-pile system and m is the total mass of the system; doubling the mass reduces the system's natural frequency by about 30%. As noted from Figure 4-3, the natural frequency of the driven pile is 4.06 Hz, which would become approximately 2.85 Hz considering the same mass as for the helical pile. The remaining difference in natural frequency between the driven and helical piles is attributed to the slight disturbance around the helical pile.

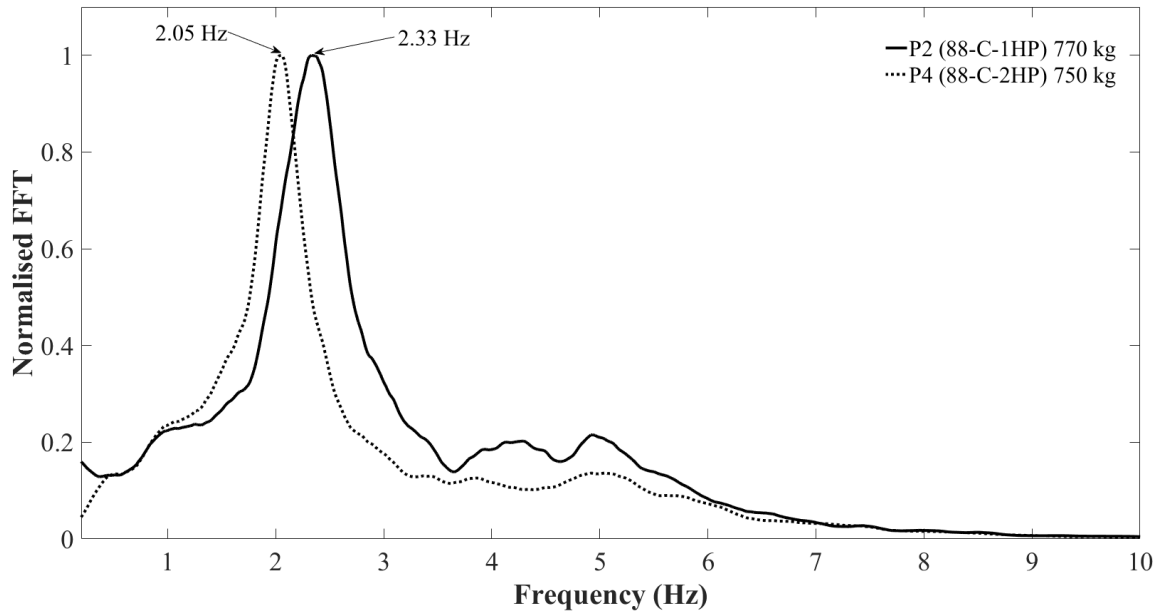


Figure 4-2: Fourier spectra of single (P2) and double (P4) helical piles response to white noise excitation

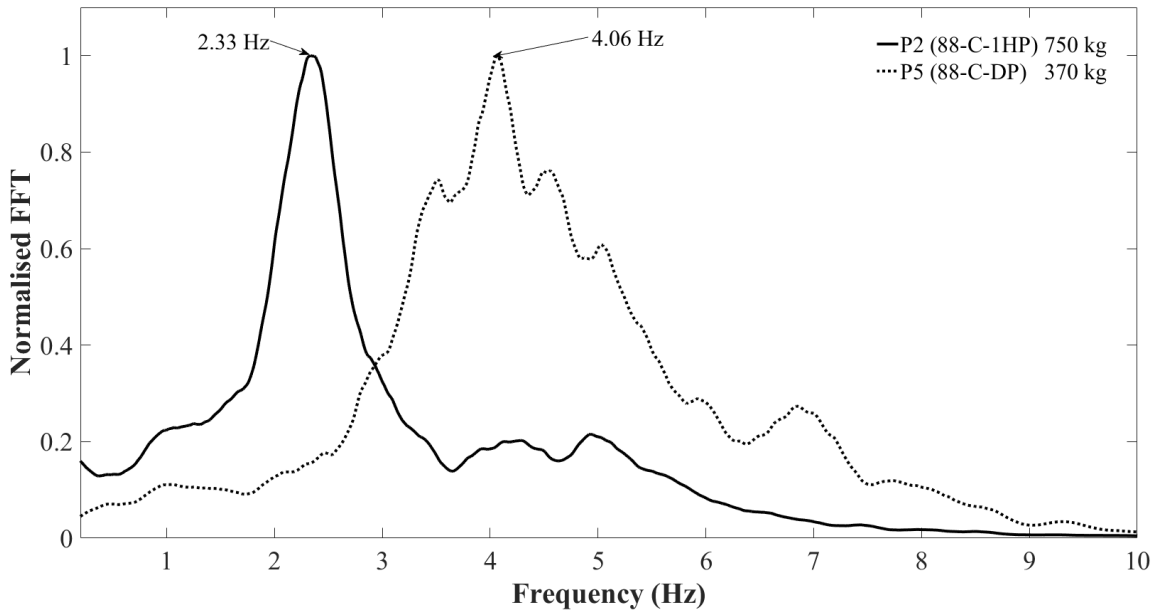


Figure 4-3: Fourier spectra of helical (P2) and driven (P5) piles response to white noise excitation

4.1.2 Effect of pile shaft shape

Several researchers have studied the effect of the shape of pile shaft on its static lateral response. Ashour and Norris (2000) performed static lateral load tests on two piles with different shaft shape but same cross-sectional area. Their results demonstrated that the square shaft pile exhibited higher lateral resistance and stiffness compared to the circular shaft pile. Abbas et al. (2008) and Heidari et al. (2014) conducted numerical analyses on piles with different cross-sectional shape but same area. They found that the square pile exhibited higher lateral resistance compared to the cylindrical pile due to the higher contact surface area between the pile and the soil. Figure 4-4 compares the Fourier spectra of the response of helical piles with circular (88-C-1HP) and square (76-S-1HP) cross-sections to white noise excitations. As can be noted from Figure 4-4, the natural frequency of the square shaft pile is significantly higher than that of the circular shaft pile. Since the pile head mass of the circular shaft was almost double of the square shaft, the mass effect must be taken into account. Adjusting the natural frequency of the square shaft pile considering the same mass as that attached to the circular shaft pile, its natural frequency would become 2.67 Hz which is slightly higher than that of the circular shaft pile (2.33 Hz).

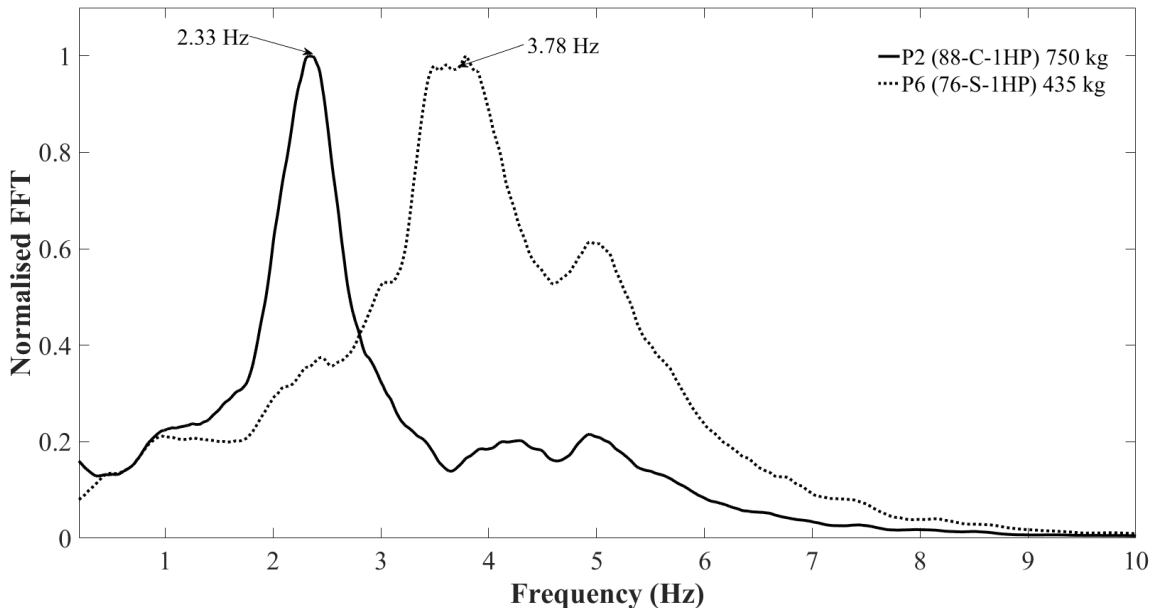


Figure 4-4: Fourier spectra of circular (P2) and square shaft (P6) piles response to white noise excitation

4.1.3 Effect of pile mass and diameter

There is an inverse relation between the natural frequency of the soil-pile system and the total mass (Equation (4.1)). Figure 4-5 compares the Fourier spectra between Piles 8 and 10, that have the same geometric properties (140-C-1HP) but almost double the mass, to white noise excitation.

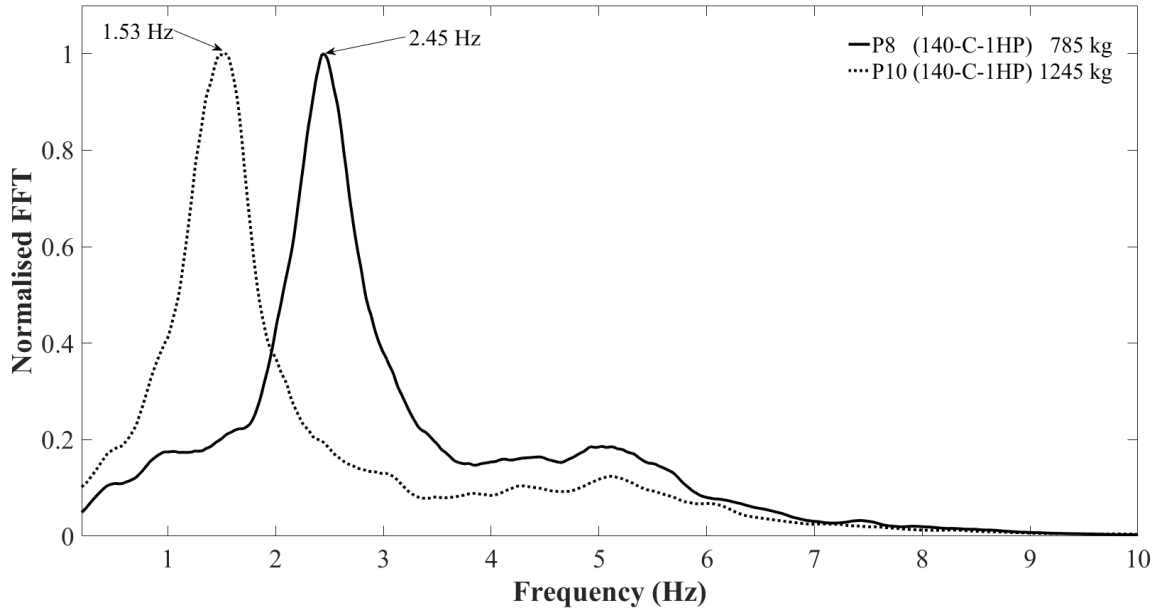


Figure 4-5: Fourier spectra of circular (140-C-1HP) piles with different masses response to white noise

Increasing the pile's diameter increases the flexural stiffness, which leads to an increase in the natural frequency of the system. On the other hand, increasing the stick out length of the pile decreases the natural frequency of the system due to the increase in the unsupported length of the pile. Both 88 and 140 mm piles had the same embedded length in the soil; however, all 88 mm piles had a stick out length of 0.3 m while 140 mm piles had a stick out length of 0.85 m. Figure 4-6 compares the Fourier spectra of response of pile 2 (88-C-1HP) and pile 8 (140-C-1HP) to white noise. The stiffness of pile 8 was slightly higher than pile 2 which indicates that the increase in stiffness due to a larger diameter overcomes the decrease in stiffness due to an larger stick out length.

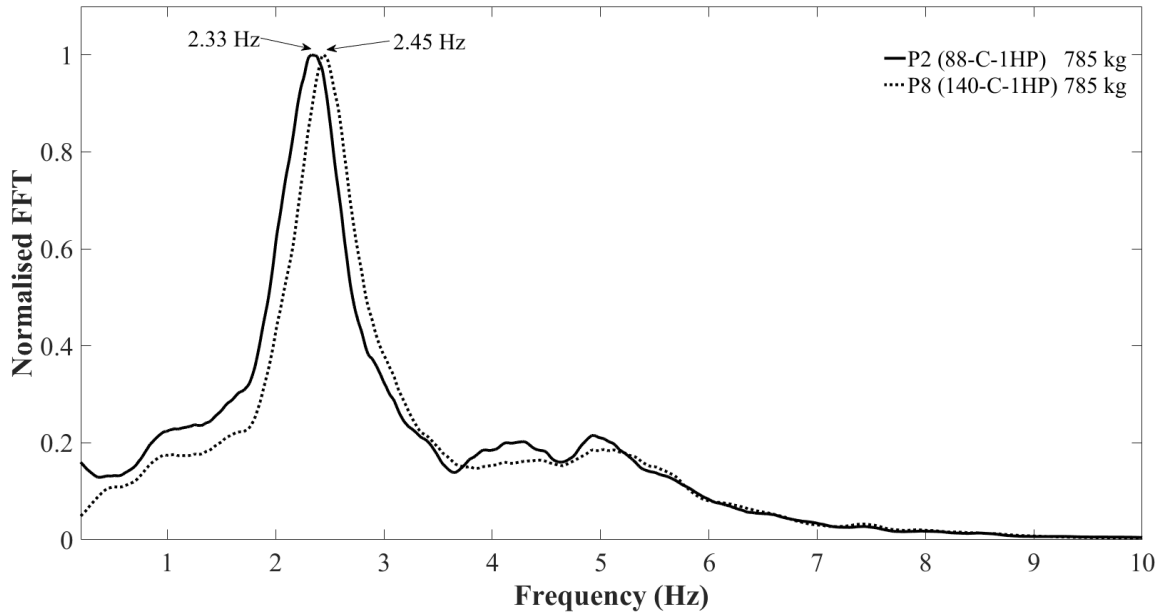


Figure 4-6: Fourier spectra of 88 mm diameter (P2) and 140 mm diameter (P8) response to white noise

4.1.4 Summary of piles response to white noise loading

The seismic response of a pile to a certain earthquake record can be evaluated in terms of frequencies or periods. In the first method, the earthquake’s predominant frequency (f_p) is compared with the pile’s natural frequency (f_{pile}). The closer the two frequencies, the higher the resonance effect and consequently, the pile response. The resonance effect can also be noted more generally through the overlap between the Fourier spectra of the earthquake loading (Figure 3-13) and the transfer function of the pile-soil system, which is approximated by the Fourier spectra of the pile’s response to white noise excitation. Unfortunately, this method lacks any quantitative values but provides a quick assessment whether the pile will resonate under a certain earthquake record.

The second method involves utilising the response spectrum, which would be established for a specific earthquake excitation. This response spectrum can be used to predict the peak acceleration for any system with a specific period. It should be noted that the response spectrum does not account for soil-structure interaction and is performed for a SDOF with 5% damping ratio. Since this method provides quantitative values, it is gaining popularity in the earthquake engineering industry.

The response spectra for both earthquakes used in this test are shown in Figure 3-14. To utilise these figures, all natural frequencies are converted to natural periods. Table 4-1 summarises the natural frequencies and periods of each soil-pile system and the corresponding expected spectral acceleration, which was obtained from the response spectrum, for each earthquake record. To determine the expected spectral acceleration for a scaled down earthquake record such as 75% and 50%, the value of the tabulated spectral acceleration is multiplied by 0.75 and 0.50, respectively.

Table 4-1: Summary of natural frequencies, period and expected spectral accelerations for both EQs for all soil-pile systems

Pile	Natural frequency (Hz)	Natural period (s)	Expected spectral acceleration for Northridge 100% (g)	Expected spectral acceleration for Takatori 100% (g)
1	2.64	0.38	1.09	<u>1.64</u>
2	2.33	0.43	0.92	<u>1.39</u>
3	1.84	0.54	0.58	<u>1.74</u>
4	2.05	0.49	0.68	<u>1.73</u>
5	4.06	0.25	<u>1.82</u>	1.11
6	3.78	0.27	<u>1.69</u>	1.15
7	1.36	0.73	0.38	<u>1.68</u>
8	2.45	0.41	0.99	<u>1.57</u>
9	2.53	0.40	0.99	<u>1.62</u>
10	1.53	0.66	0.47	<u>1.69</u>

4.2 Seismic response of helical piles

4.2.1 Effect of loading characteristics

The pile's seismic response is affected by the earthquake's intensity (i.e. peak acceleration amplitude), earthquake's predominant frequency and pile's natural frequency. The effect

of loading frequency and intensity is investigated by comparing the response of different piles in terms of maximum deflections and dynamic p-y curves at different depths.

4.2.1.1 Loading frequency

To determine the effect of loading frequency, the pile's response during Northridge 100% (peak acceleration of 0.50g) and Takatori 75% (peak acceleration of 0.50g) are compared. As previously noted from Figure 3-13, the energy content of Northridge record is spread over a wide range of frequency (i.e. 1 Hz – 5.0 Hz) while Takatori record's energy content is concentrated within a narrow range 0.5 Hz to 1.5 Hz. Meanwhile, the transfer functions of the tested circular helical piles had significant amplitudes between 1.35 and 2.65 Hz, depending on the pile diameter and the mass attached to its head. This range is closer to the narrow range of frequency for Takatori record (0.5 – 1.5 Hz). Therefore, Takatori 75% caused greater response than Northridge 100%. On the other hand, the driven pile and square shaft helical pile had transfer functions with significant amplitudes within the frequency range (3.65 - 4.10 Hz), i.e., within frequency range of the Northridge record and far from the frequency range of Takatori record. Hence, their response to Northridge 100% was higher than their response to Takatori 75%.

The same conclusion could be reached by considering the spectral accelerations reported in Table 4-1. It can be concluded that all circular helical piles would have greater spectral accelerations during Takatori 75%, while the driven pile and square shaft helical pile would have greater spectral accelerations during Northridge 100%.

Example of difference in response (maximum pile deflection) due to the loading frequency can be seen in Figure 4-7.

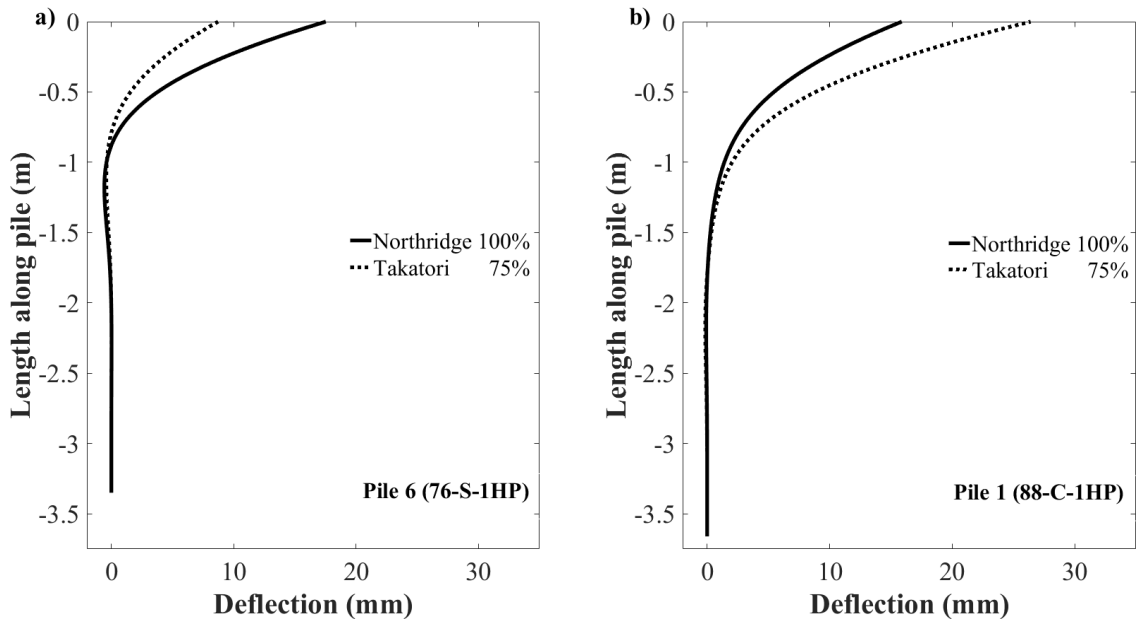


Figure 4-7: Frequency effect on pile response a) Pile 6 - Square shaft helical pile b) Pile 1 - Circular shaft helical pile

The effect of the loading frequency on the dynamic p-y curve for Pile 1 is shown in Figure 4-8. Even though both earthquakes have the same peak acceleration, Takatori 75% resulted in larger hysteretic loops, which indicates higher pile deflection due to the resonance condition as well as higher damping. It can also be seen that the backbone of the dynamic p-y curve was not highly affected by the loading frequency. With increase in depth, lower pile deflection occurred (almost linear elastic behaviour) and hence smaller hysteretic loops and lower damping were realized. Slight soil degradation can be seen, which may be due to the high relative density of the soil (dense sand), which agrees with the findings of Yang et al. (2011) and Dou and Byrne (1996).

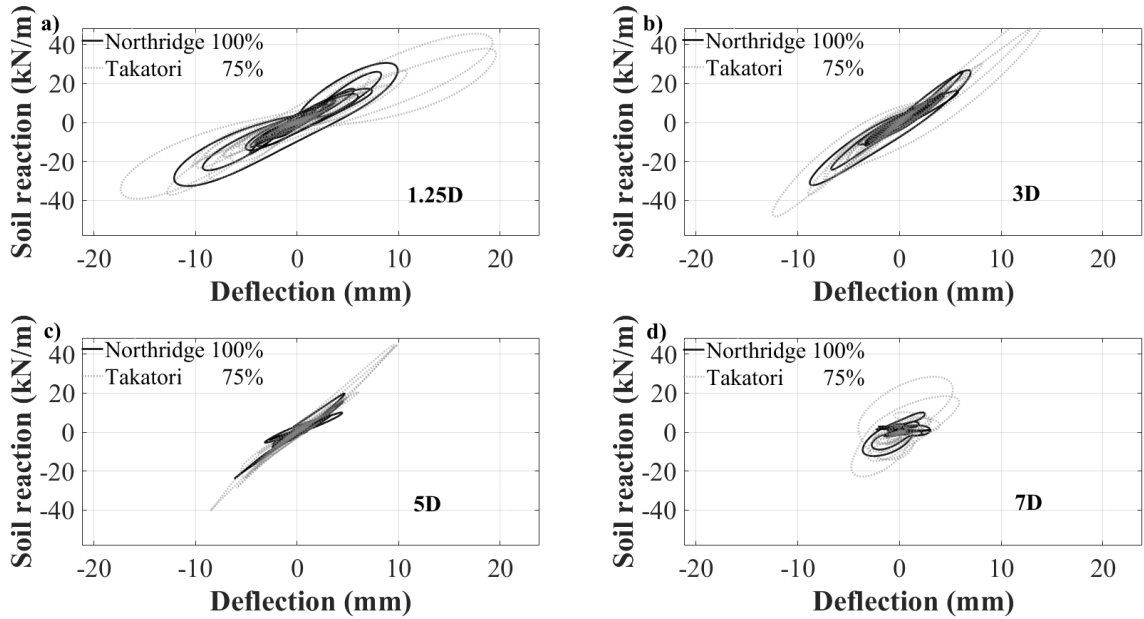


Figure 4-8: Effect of load frequency on dynamic p-y curve for Pile 1 a) Depth of 1.25D b) Depth of 3D c) Depth of 5D d) Depth of 7D

4.2.1.2 Loading intensity

Another important characteristic of earthquake loading is its intensity, which could be evaluated in terms of its peak acceleration. The results indicated there was generally a linear correlation between the loading intensity and the maximum bending moment in the pile only when the loading frequency was close to the natural frequency of the pile-soil system. However, due to the complexity of the non-linearity occurring during the shaking, further investigation is required to confirm this observation. An example of how load intensity affected maximum bending moment is shown in Figure 4-9 for Pile 4 (88-C-2HP), which had two helices attached to its circular shaft. It was also found that the depth of maximum bending moment increased as the intensity of the loading increased, which agrees with the findings of Dou and Byrne (1996), Boulanger et al. (1999), Rovithis et al. (2009) and Heidari et al. (2014b).

An example of the effect of load intensity on the dynamic p-y curve is shown for Pile 1 Northridge and Takatori (Figure 4-10 and Figure 4-11). The results show that for high intensity, as expected, larger hysteretic loops were obtained, which indicates increased

damping and significant soil non-linearity; for lower intensity excitations, for example 50% versus 100%, the hysteretic loops were more linear.

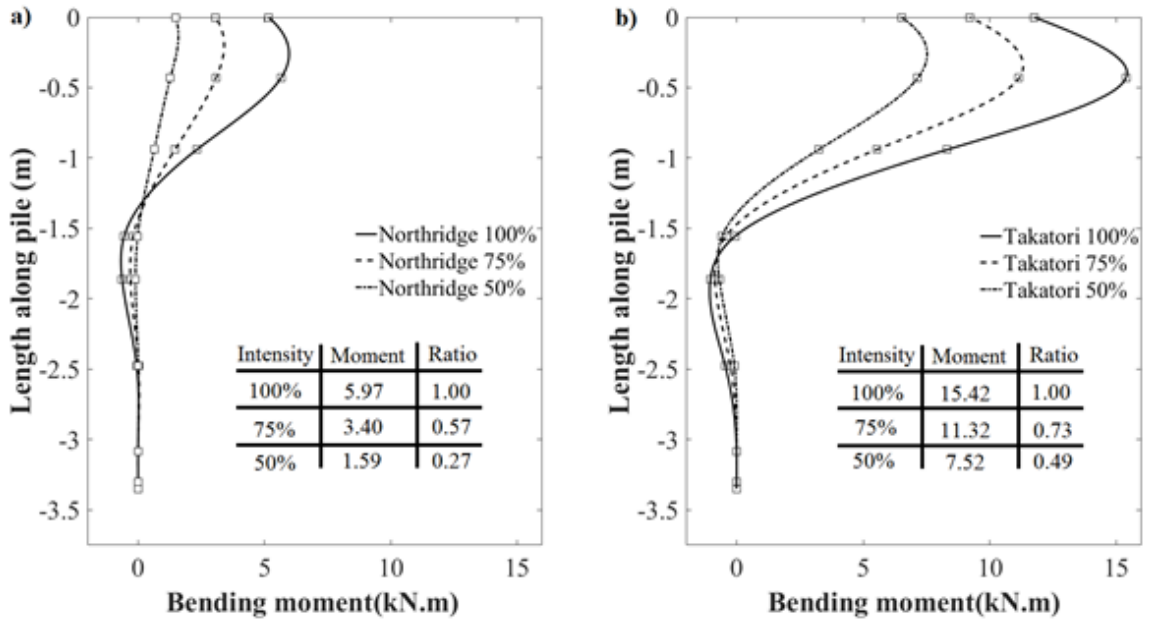


Figure 4-9: Loading intensity correlation with maximum bending moment for P4 a) Northridge b) Takatori

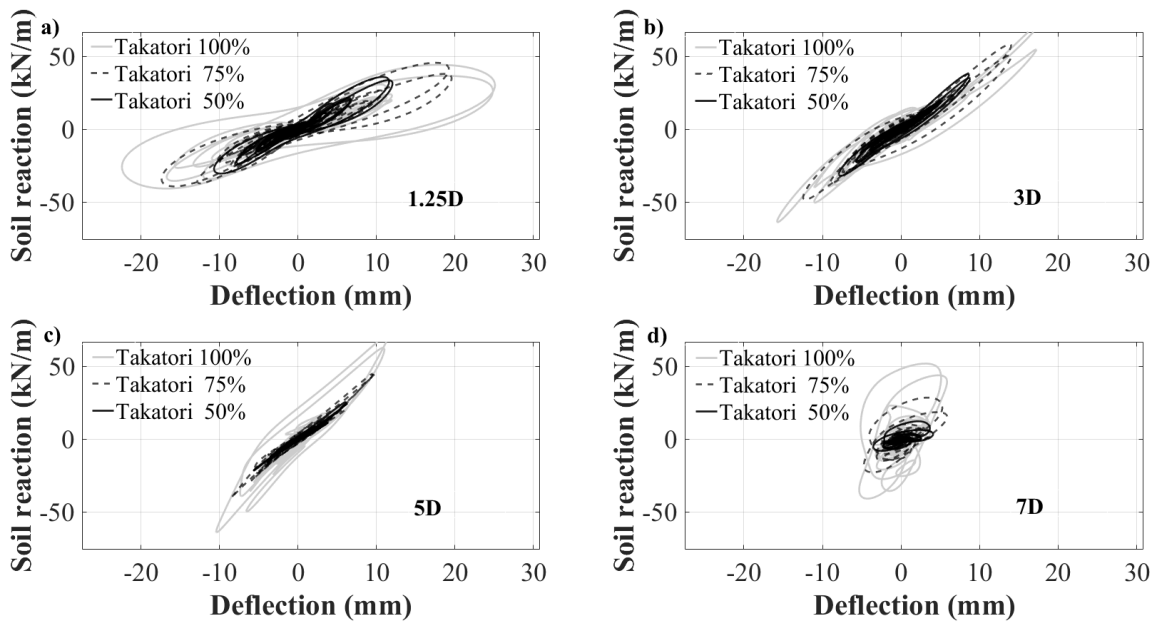


Figure 4-10: Effect of loading intensity on dynamic p-y curve for Pile 1 Takatori a) Depth of 1.25D b) Depth of 3D c) Depth of 5D d) Depth of 7D

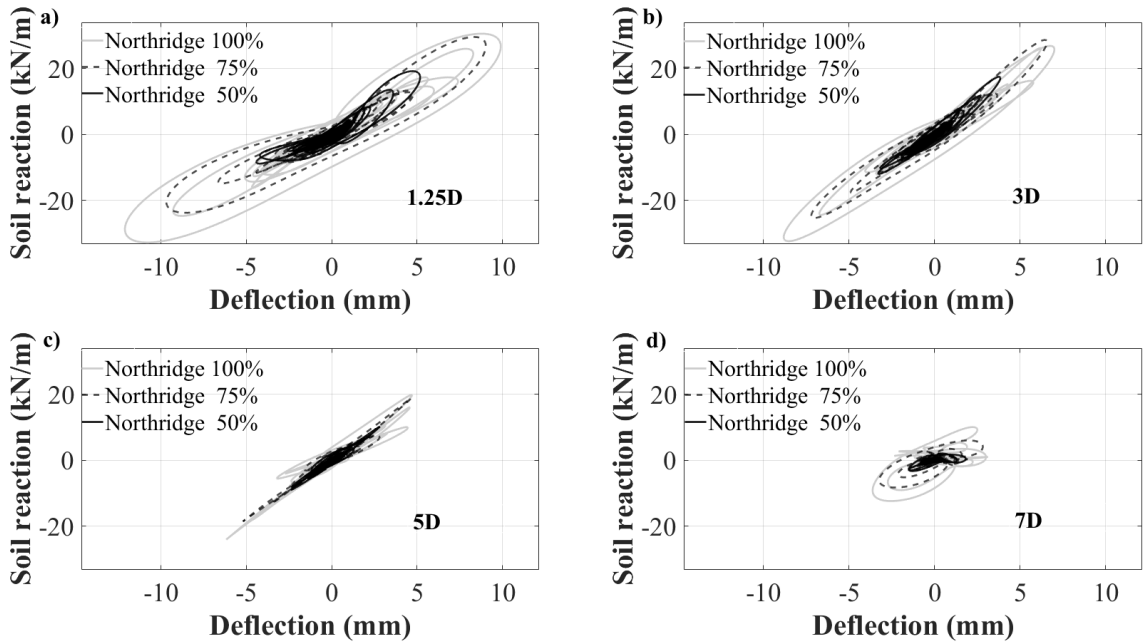


Figure 4-11: Effect of loading intensity on dynamic p-y curve for Pile 1 Northridge
a) Depth of 1.25D b) Depth of 3D c) Depth of 5D d) Depth of 7D

4.3 Effect of pile configuration

4.3.1 Effect of installation method: helical pile versus driven pile (P2 vs P5)

The responses of P2 (helical pile) and P5 (driven pile) were compared in order to better understand the influence of the installation method on the dynamic behavior of deep foundations. While the comparison cannot be direct because the inertial weight of the helical pile was twice the inertial weight that the driven pile resisted, observations can be made on the behavior based on frequency contents. The natural frequencies of both piles 2 and 5 lied within the frequency range of the Northridge earthquake (1.0 – 5.0 Hz). On the other hand, the natural frequency of the helical pile was very close to the predominant frequency range of the Takatori earthquake, which led to amplification of the response due to resonance.

The force at the pile head can be approximated by calculating the product of the expected spectral acceleration at the pile head times the supported inertial mass. The expected

spectral accelerations for P2 and P5 for Northridge 100% are 0.92g and 1.82g, respectively. By taking into consideration that P5 had half the inertial mass of P2, the peak resulting forces at both pile's head should be almost equal during the Northridge earthquake. For Takatori 100%, the expected spectral accelerations for P2 and P5 are 1.39g and 1.11g, respectively. It is evident that P2 would exhibit a greater response than P5 during Takatori 100%. Figure 4-12 compares the peak deflections and back-calculated shear forces at piles' head for P2 and P5 during Northridge 100% and Takatori 100%. The results in Figure 4-12 demonstrate that during the Northridge 100% earthquake, the maximum deflections were almost the same for P2 and P5, whereas for Takatori earthquake, the helical pile (P2) experienced significantly higher maximum deflection.

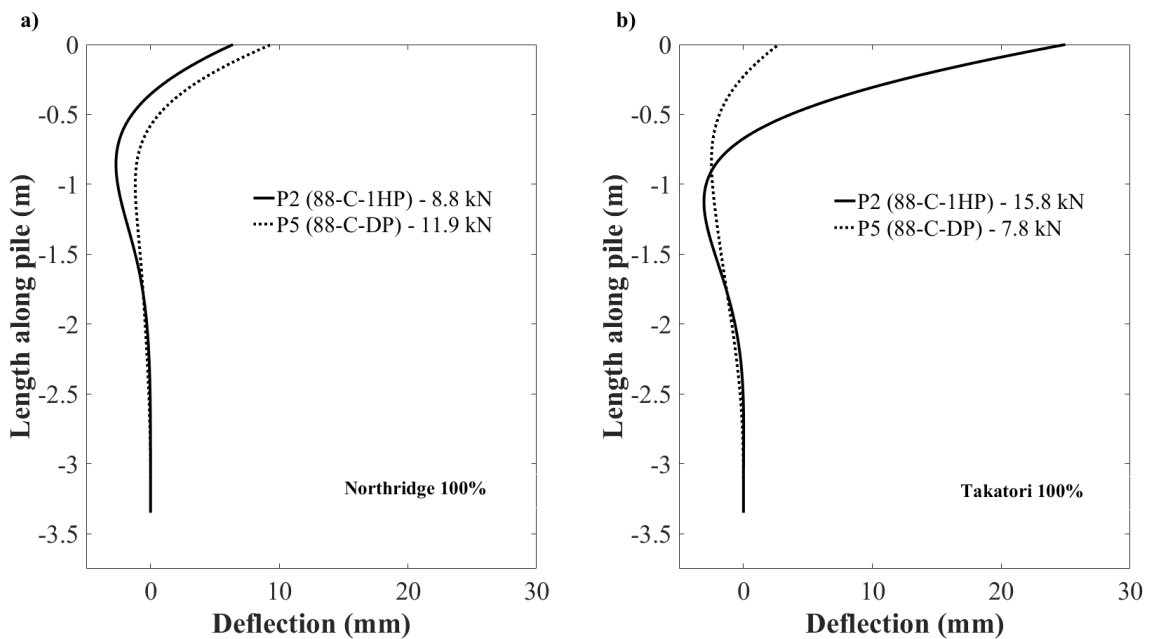


Figure 4-12: Maximum deflection of single helical (P2) and driven (P5) piles a) Northridge 100% b) Takatori 100%

This also can be observed by comparing the dynamic p-y curves of P2 and P5. Figure 4-13 and Figure 4-14 show the dynamic p-y curves for P2 and P5 during Northridge 100% and Takatori 100%, respectively. As it can be seen, during Northridge 100%, the hysteresis behaviour is almost the same. While during Takatori 100%, P2 experienced higher deflection and correspondingly bigger p-y loops indicating higher damping than P5.

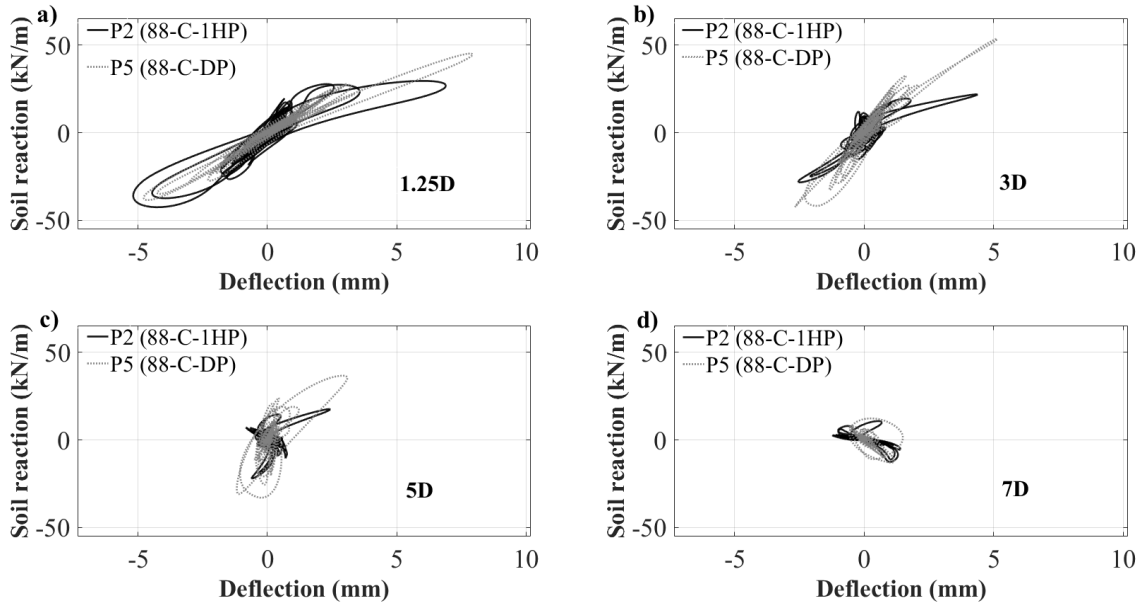


Figure 4-13: Comparison of dynamic p-y curves during Northridge 100% for single helical pile (P2) and driven pile (P5) at different depths a) 1.25D b) 3D c) 5D d) 7D

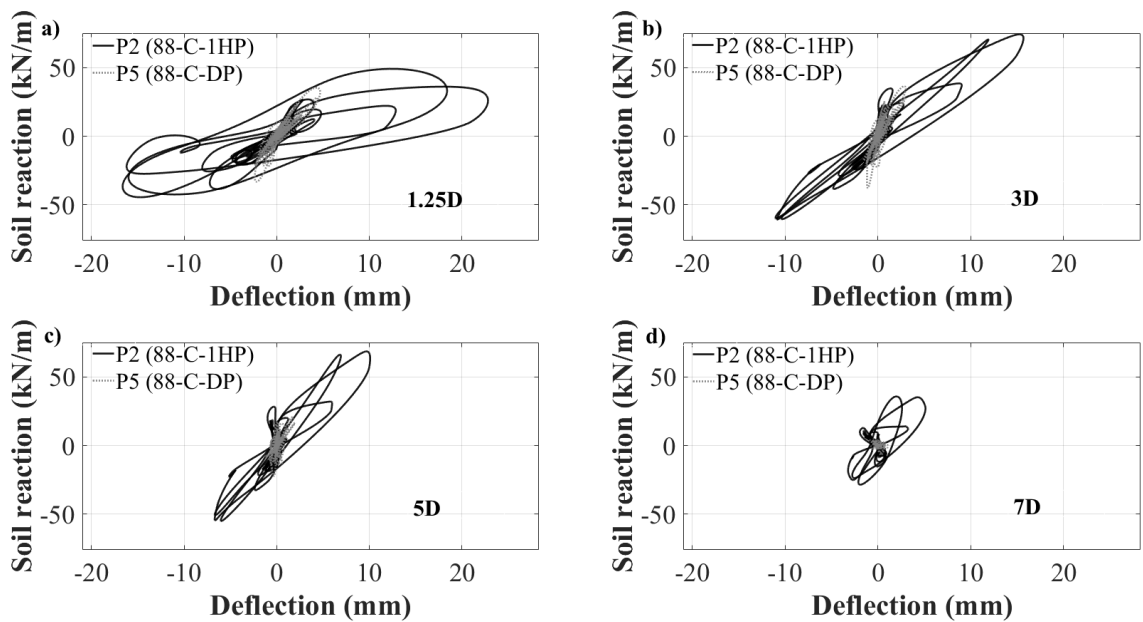


Figure 4-14: Comparison of dynamic p-y curves during Takatori 100% for single helical pile (P2) and driven pile (P5) at different depths a) 1.25D b) 3D c) 5D d) 7D

4.3.2 Effect of number of helices: single helix versus double helix (P2 vs P4)

To evaluate the influence of different helix configurations on the lateral seismic response, the performance of P2 with single helix of diameter 250 mm and P4 with a 200 mm diameter bottom helix and a 250 mm diameter top helix are compared. Both piles had natural frequencies close to the narrow predominant frequency range of Takatori and within the wide predominant frequency range of Northridge. The spectral acceleration for P4 was expected to be slightly higher than P2 during both earthquakes.

It was observed that the responses of P2 and P4 were fairly close during both Northridge and Takatori as shown in Figure 4-15 and Figure 4-16. During all Northridge shakes, P4 had slightly higher deflection than P2 as expected from the spectral accelerations. On the other hand, during the Takatori shakes, P4 initially exhibited higher deflection than P2. As the intensity of Takatori increased, the difference in response between the piles decreased due to the higher resistance contribution of the second helix at high deflections. The contribution of the second helix could also be observed by comparing the p-y curves of P2 and P4 during Takatori 100% and Takatori 50% as shown in Figure 4-17 and Figure 4-18, respectively. As the intensity increased, the p-y curves shifted and overlapped over each other indicating similar response.

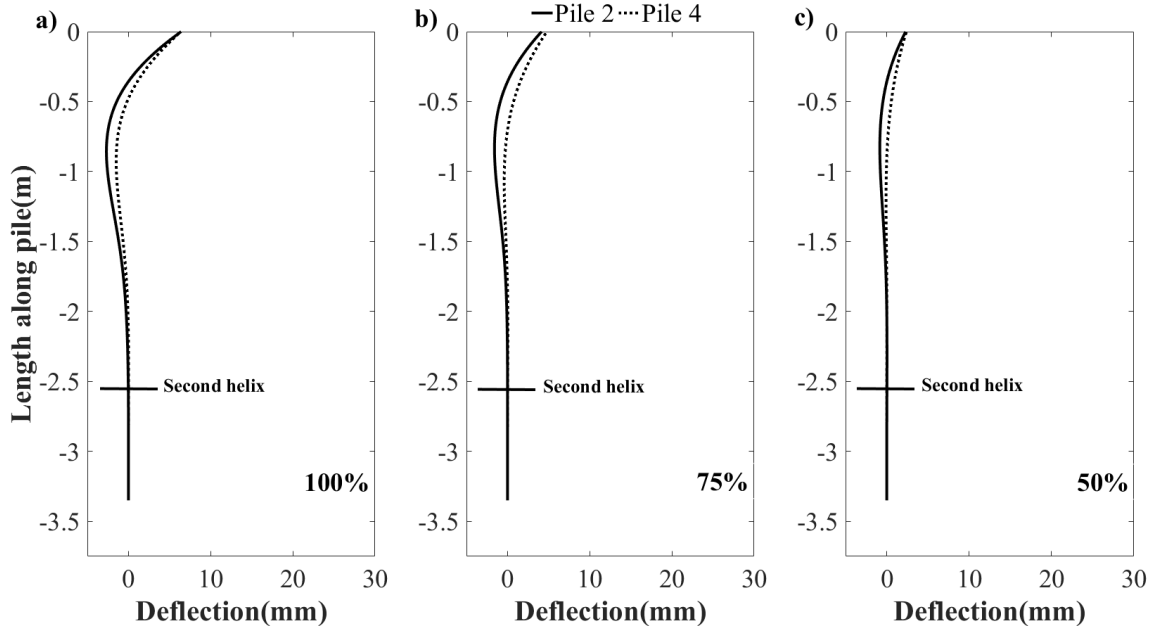


Figure 4-15: Comparison between maximum deflections of single helical (P2) and double helical (P4) piles during Northridge all intensities a) 100% b) 75% c) 50%

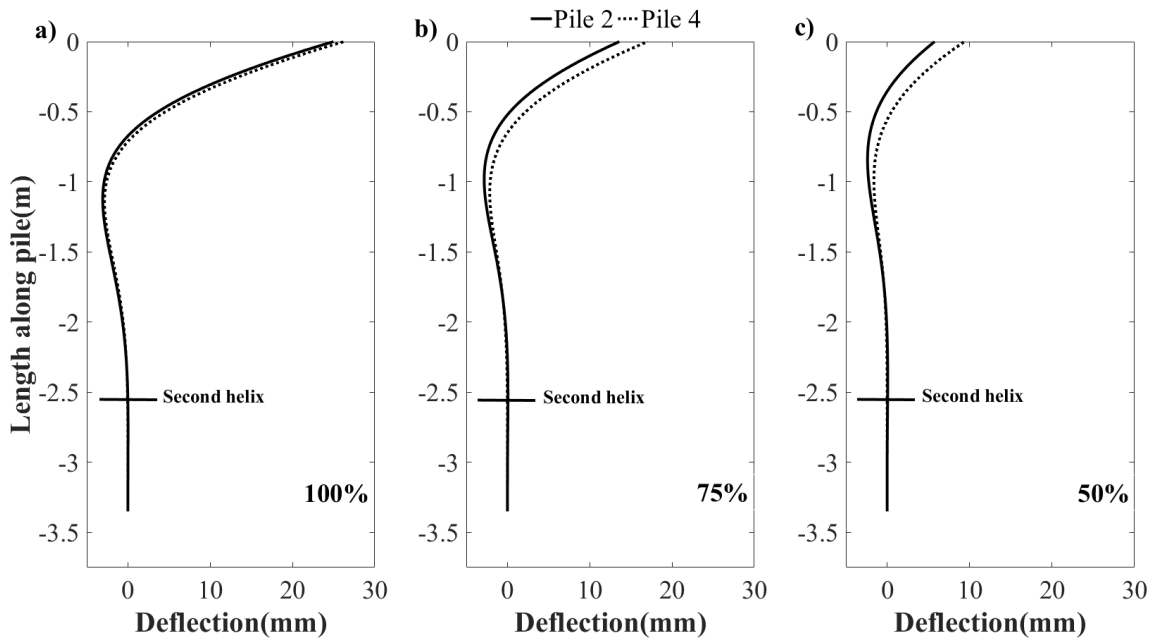


Figure 4-16: Comparison between maximum deflections of single helical (P2) and double helical (P4) piles during Takatori all intensities a) 100% b) 75% c) 50%

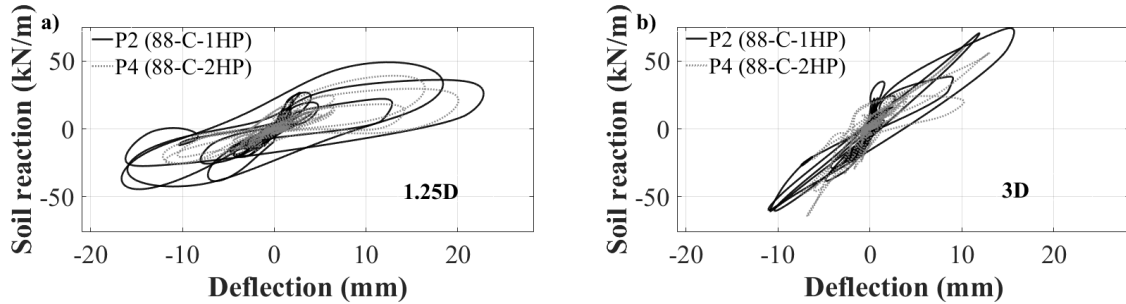


Figure 4-17: Comparison of dynamic p-y curves during Takatori 100% for single helical pile (P2) and double helical pile (P4) at different depths a) 1.25D b) 3D c) 5D d) 7D

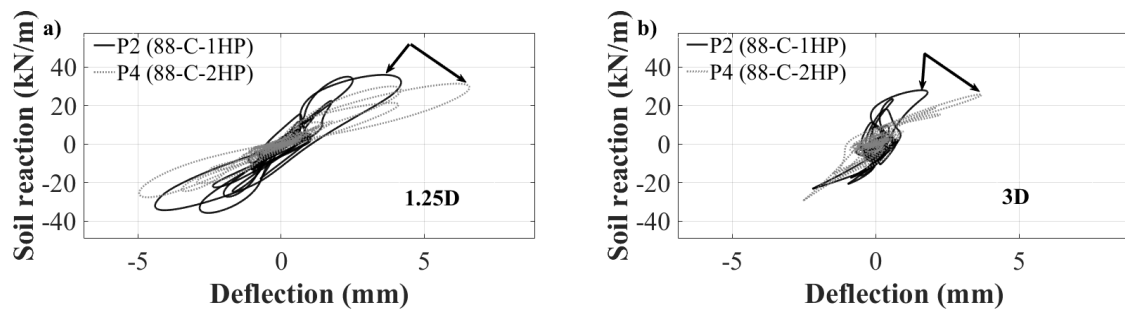


Figure 4-18: Comparison of dynamic p-y curves during Takatori 50% for single helical pile (P2) and double helical pile (P4) at different depths a) 1.25D b) 3D c) 5D d) 7D

4.3.3 Effect of pile shaft shape: circular shaft helical pile versus square shaft helical pile (P3 vs P6)

The responses of P3 (circular helical pile) and P6 (square helical pile) are compared in order to better understand the influence of the pile shaft shape on the dynamic behavior of deep foundations. The natural frequencies of both P3 and P6 were within the wide predominant frequency range of Northridge, while P3’s natural frequency was close to the narrow predominant frequency range of Takatori.

The expected spectral accelerations during Northridge 100% indicate that P6 would have peak acceleration about 3 times that of P3, which would result in approximately 1.5 times greater shear at the pile head (considering the difference in supported mass). On the other hand, the expected spectral accelerations during Takatori 100% suggest higher peak acceleration for P3, by about 1.5 times that of P6.

Figure 4-19 shows the peak response (deflection) and back calculated shear at the piles' head for both P3 and P6 during Northridge 100% and Takatori 100%. As initially predicted, P6 exhibited higher response during Northridge 100% than P3. For Takatori 100%, P3 resonated with the loading frequency of the earthquake and showed higher response than P6.

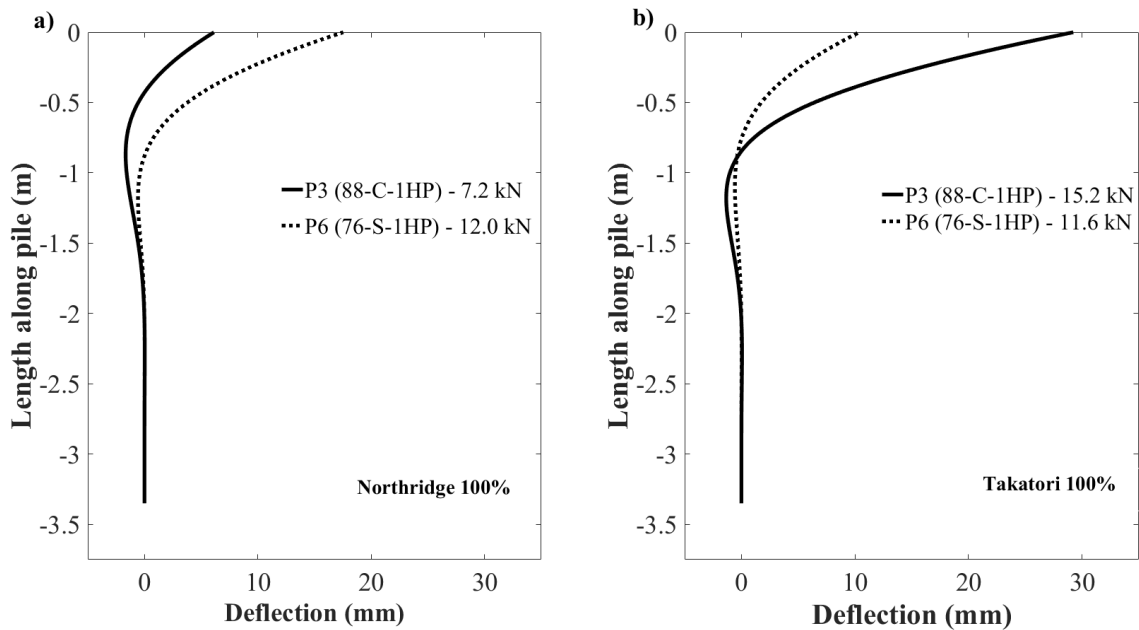


Figure 4-19: Maximum deflection of circular helical (P3) and square helical (P6) piles a) Northridge 100% b) Takatori 100%

The same conclusion could be reached by inspecting the dynamic p-y curves of P3 and P6 during Northridge 100% and Takatori 100% as shown in Figure 4-20 and Figure 4-21, respectively. During Northridge 100%, P6 had bigger p-y loops indicating higher deflections and damping behaviour than P3. While for Takatori 100%, P3 had bigger p-y loops than P6. It can also be noted that the backbone curve connecting the peaks of the loops were the same for both piles, which indicates minimal effect of pile shaft shape on the stiffness of the dynamic p-y curve.

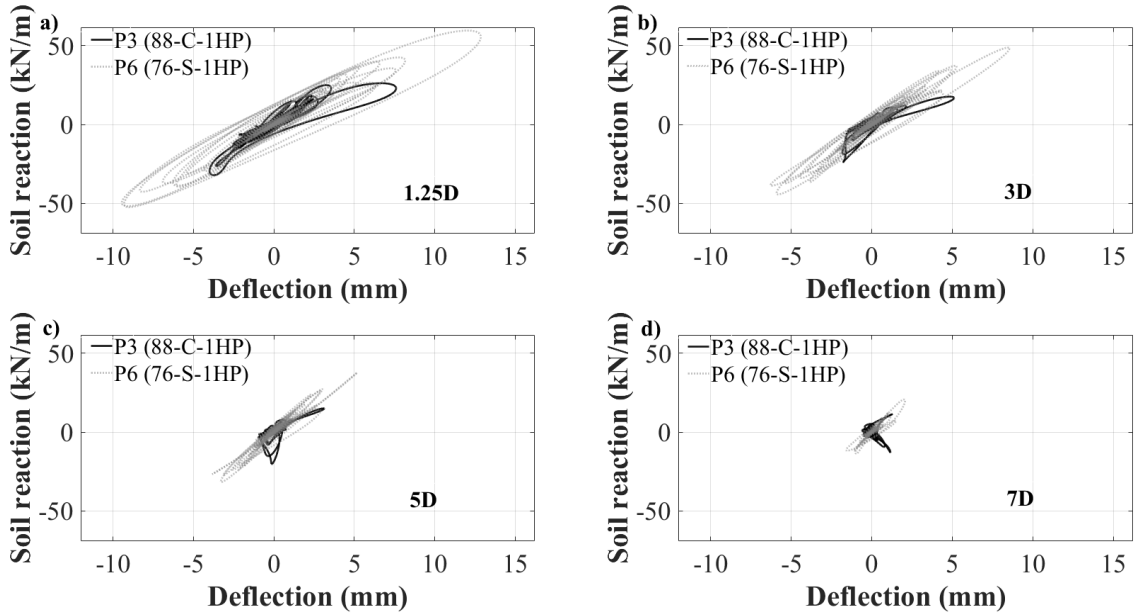


Figure 4-20: Comparison of dynamic p-y curves during Northridge 100% for circular helical pile (P3) and square helical pile (P6) at different depths a) 1.25D b) 3D c) 5D d) 7D

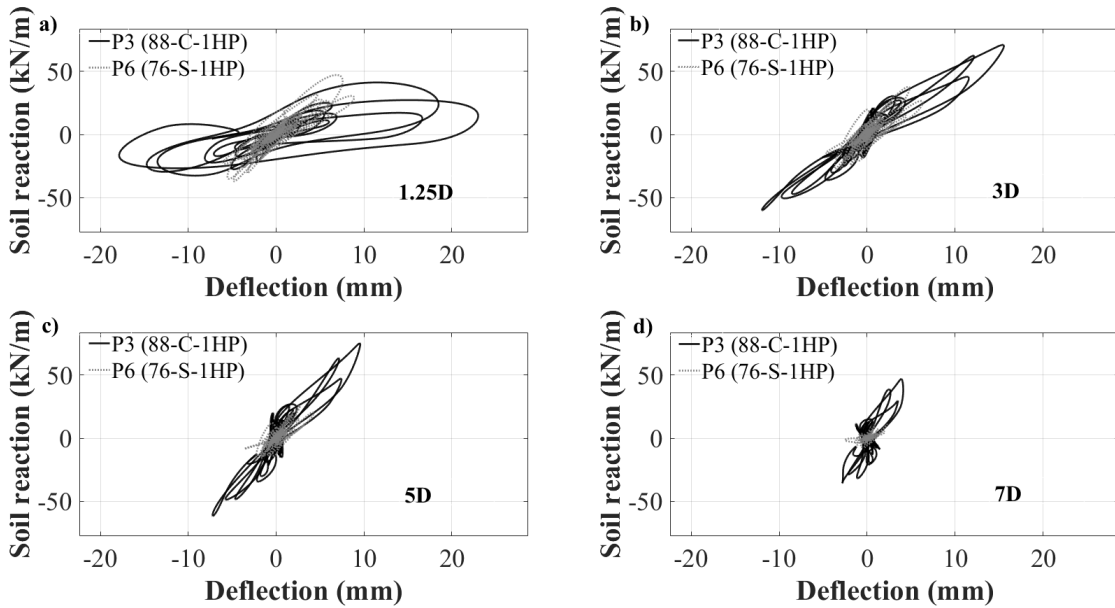


Figure 4-21: Comparison of dynamic p-y curves during Takatori 100% for circular helical pile (P3) and square helical pile (P6) at different depths a) 1.25D b) 3D c) 5D d) 7D

4.3.4 Effect of coupling type: threaded versus bolted coupling (P1 vs P2 and P3)

Helical piles are manufactured with different types of coupling or connections. In this research, there were two main types of coupling: threaded and bolted. P1 had a threaded coupling while P2 and P3 had bolted coupling connections. The dynamic behavior of these piles during Takatori 100% can be compared in terms of the dynamic p-y hysteretic loops obtained for the upper portions of the pile (1.25D to 7D) (Figure 4-22) for piles 1,2 and 3. It was observed that the hysteretic behavior was essentially the same for all piles. This shows that the effect of the coupling used had minimal effect on the piles' behaviour during the shaking. This is may be due to the fact the coupling was located 1.2m below the ground surface (i.e. more than 13.5 times the pile diameter (D)). Accordingly, the coupling had no effect on the lateral response of piles because, typically, the pile deflections below 10D – 15D are insignificant. It was also noted that the response of P2 was exactly the same pile as P3 as shown in Figure 4-22, which provided a sense of repeatability and reliability within the testing program. This repeatability also lends credence to the hypothesis that the type of coupling did not affect the seismic behavior when the coupling was located at least 13.5D below the ground surface.

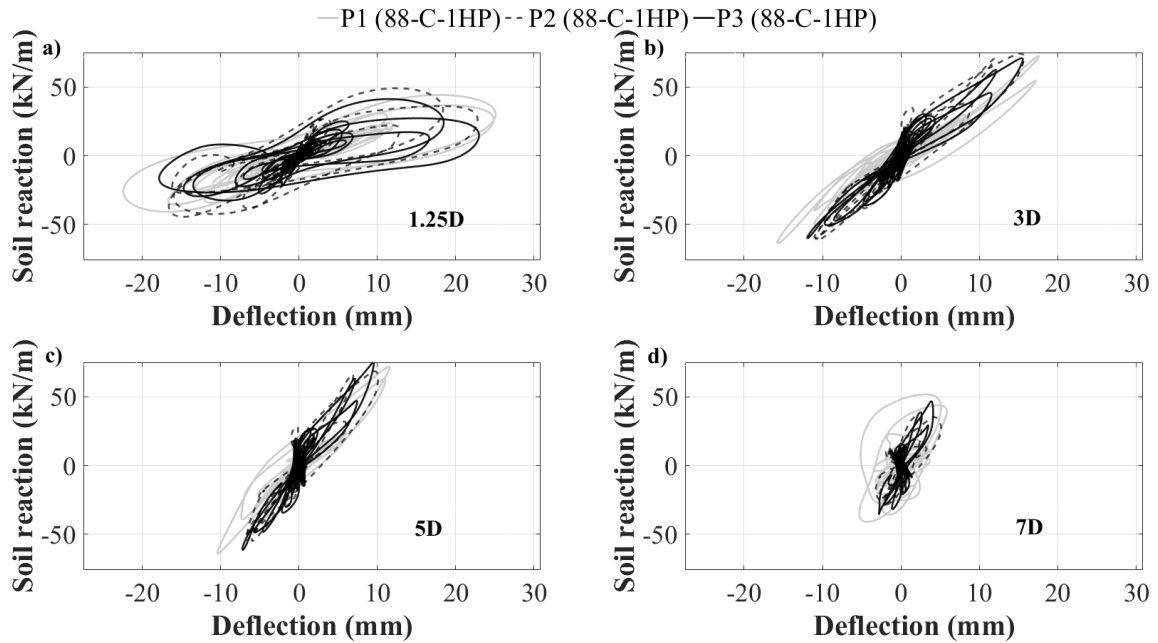


Figure 4-22: Comparison of dynamic p-y curves during Takatori 100% for threaded coupling (P1) and bolted coupling (P2 and P3) at different depths a) 1.25D b) 3D c) 5D d) 7D

4.4 Conclusions

The natural frequencies of the piles, as well as their dynamic p-y curves were used to investigate the effect of shaft geometry, helix configuration, coupling type, installation method and subsequent disturbance on the seismic behavior of helical piles. Based on the obtained test results, the following conclusions can be made:

1. The natural frequency of the piles could be obtained from the fast Fourier transform of either the strain gauge or the accelerometer readings. Both displayed the same peaks; however, the second peak was more pronounced when using the accelerometer readings due to the higher rotation at the location of the accelerometer (on top of the concrete mass).
2. The double helical pile showed slightly lower natural frequency when compared to the single helical pile. This is attributed to slightly higher disturbance associated with the second helix during installation.
3. The driven pile showed slightly higher natural frequency when compared to the single helical pile (after accounting for mass difference). This is attributed to the slight disturbance in the soil around the helical pile.

4. The square shaft helical pile showed slightly higher natural frequency when compared to the circular shaft helical pile (after accounting for mass difference). This is due to the higher contact area between the pile and soil when using a square shaft.
5. Increasing the mass supported at the pile head showed a reduction in the natural frequency of the pile. Increasing the pile's diameter from 88 mm to 140 mm did not result in a big increase in the natural frequency. This is due to the accompanied increase in the stick out length with the large diameter piles that causes a decrease in the natural frequency.
6. The response of the pile is highly affected by the closeness of the loading frequency to the natural frequency of the soil-pile system, i.e. resonance condition. For all circular helical piles, the Takatori earthquake resulted in higher response due to the resonance condition. The driven and square shaft helical piles experienced higher response during the Northridge earthquake due to their higher natural frequency, which was closer to the loading predominant frequency. Owing to soil nonlinearity associated with the large response, which is caused by the resonance condition, the soil reactions were characterized by larger hysteretic loops indicating higher damping.
7. The frequency of loading did not have any effect on the backbone of the dynamic p-y curves for all piles which is expected given the sandy nature of the soil in the conducted shake table tests.
8. As the intensity of the earthquake increased, the depth of the maximum bending moment increased. Also a rough linear relationship was found between the intensity of the earthquake and the maximum bending moment only when the predominant frequency of loading was close the natural frequency of the pile. However, due to the non-linear nature of the response of the piles, further investigation is required.
9. During the Northridge earthquake, the helical pile exhibited very close, if not better, response to that of the driven pile. This illustrates the ability of helical piles to perform as good as conventional piles under seismic loading when both of the piles responses were not affected by the resonance condition.

10. The contribution of the second helix increased as the double helical pile deflection increased. This was highlighted during the different intensities of Takatori. As the intensity increased from 50% to 100%, the difference in response between single and helical pile decreased which indicates increased lateral resistance due to the contribution of the second helix at high deflections.
11. There was no clear advantage for the shape of pile cross-section (i.e. square or circular) because the resonance condition affected their response differently in both ground motions considered. It was also seen that the backbone curve of both piles was not affected by the pile shaft shape.
12. The type of couple and its inherent stiffness may affect the seismic behavior of the helical pile, depending on its location below the ground surface relative to the pile diameter. In all the tests performed, there were no performance difference between threaded and bolted couplings.

4.5 References

- Abbas, J.M., Chik, Z.H., and Taha, M.R. 2008. Single pile simulation and analysis subjected to lateral load. *Electronic Journal of Geotechnical Engineering*, 13 E: 1–15.
- Ashour, M., and Norris, G. 2000. Lateral loading of a pile in layered soil using the strain wedge model. *Journal of Geotechnical and Geoenvironmental Engineering*, 126(May): 420–428.
- Bagheri, F., and El Naggar, M.H. El. 2015. Effects of installation disturbance on behavior of multi-helix anchors in sands. *DFI Journal - The Journal of the Deep Foundations Institute*, (December): 80–91. doi:10.1179/1937525515Y.0000000008.
- Boulanger, B.R.W., Curras, C.J., Member, S., Kutter, B.L., Wilson, D.W., Member, A., and Abghari, A. 1999. Seismic soil-pile-structure interaction experiments and analyses. *Journal of Geotechnical and Geoenvironmental Engineering*, 125(September): 750–759.
- Dou, H., and Byrne, P.M. 1996. Dynamic response of single piles and soil-pile interaction. *Canadian Geotechnical Journal*, 33(1): 80–96. NRC Research Press. doi:10.1139/t96-025.
- Heidari, M., Jahanandish, M., El Naggar, H., and Ghahramani, A. 2014a. Nonlinear cyclic behavior of laterally loaded pile in cohesive soil. *Canadian Geotechnical Journal*, 51(2): 129–143. doi:DOI 10.1139/cgj-2013-0099.
- Heidari, M., El Naggar, H., Jahanandish, M., and Ghahramani, A. 2014b. Generalized cyclic p-y curve modeling for analysis of laterally loaded piles. *Soil Dynamics and Earthquake Engineering*, 63: 138–149. Elsevier. doi:10.1016/j.soildyn.2014.04.001.
- Kulhawy, F.H. 1985. Uplift behavior of shallow soil anchors -an overview. In *Uplift behavior of anchor foundations in soil*. p. 25.
- Lutenegger, A.J., Erikson, J., and Williams, N. 2014. Evaluating Installation Disturbance of Helical Anchors in Clay from Field Vane tests. *Deep Foundation Institute*,: 129–138.
- Mitsch, M.P., and Clemence, S.P. 1985. The uplift capacity of helix anchors in sand. In *Uplift behavior of anchor foundations in soil*. pp. 26–47.
- Rovithis, E., Kirtas, E., and Pitilakis, K. 2009. Experimental p-y loops for estimating seismic soil-pile interaction. *Bulletin of Earthquake Engineering*, 7(3): 719–736. doi:10.1007/s10518-009-9116-7.
- Sakr, M. 2009. Performance of helical piles in oil sand. *Canadian Geotechnical Journal*, 46(9): 1046–1061. doi:10.1139/T09-044.

Trofimenkov, J. G., and Mariupol'skii, L. G. 1965 Screw Piles Used for Mast and Tower Foundations, Proceedings, 6th International Conference on Soil Mechanics and Foundation Engineering, Montreal, Canada, Vol. 2, pp. 328- 332

Yang, E.K., Choi, J.I., Kwon, S.Y., and Kim, M.M. 2011. Development of dynamic p-y backbone curves for a single pile in dense sand by 1g shaking table tests. KSCE Journal of Civil Engineering, 15(5): 813–821. doi:10.1007/s12205-011-1113-0.

NUMERICAL MODELING

In this chapter, ABAQUS v.6.13.3 (SIMULIA 2013a) finite element software was used to model the full-scale shaking table experiment. This chapter presents the different aspects of the developed 3D finite element model including geometry, element type selection, material models, contact formulation and boundary conditions. A mesh sensitivity analysis was performed to select the optimum mesh to ensure the 3D finite element model provides accurate prediction of simulated pile behaviour. Several levels of model verification were conducted to verify the ability of the model to evaluate the static and seismic behaviour of both the soil and pile. Final verification was conducted employing the experimental test results obtained from large scale shake table tests of single helical piles. After verifying the numerical model, a limited parametric study is performed to understand and study the effect of different geometric aspects of the helical pile on the static py curves.

5.1 Numerical Model features

5.1.1 3D Geometry

The soil and pile, including all its components, were simulated in three-dimensional (3D) space. The geometry of the soil-pile model simulated the full-scale shaking table test setup as close as possible. The 3D soil block dimensions matched the physical dimensions of the laminar shear box: 6.70 m long, 3.0 m wide and 4.57 m high (height of soil inside box). The schematic of the laminar box and soil block, and their dimensions are shown in Figure 5-1.

The helical pile system consisted of two components: the steel pile section and the concrete blocks at the pile head. The connection between them is assumed to be rigid. The concrete blocks were modeled as a solid body that has the same dimensions as that used in the test. The helical plate was simulated as a planar cylindrical disk to simplify the meshing process. This would not affect the lateral behaviour of the pile (Kurian and Shah, 2009). The

schematic and dimensions of the helical pile considered in the analysis, Pile 1, are shown in Figure 5-2.

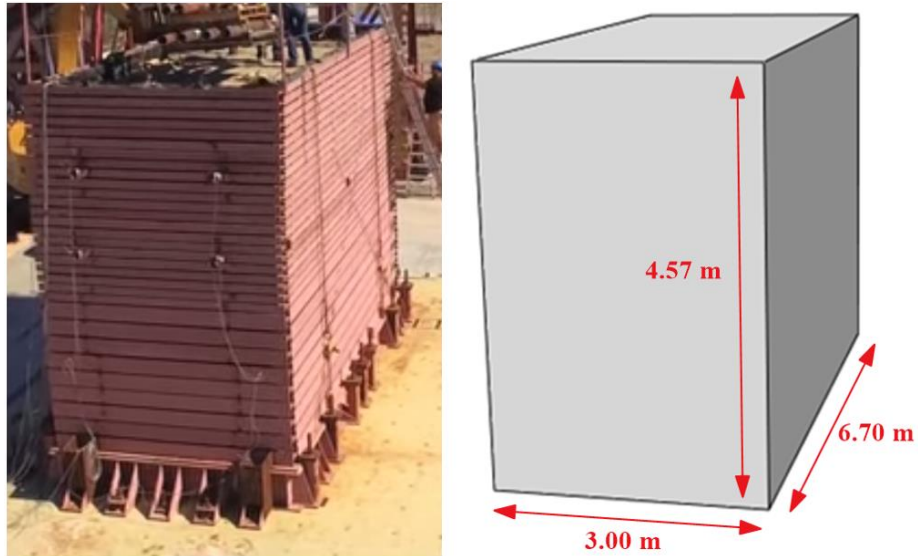


Figure 5-1: Soil block dimensions

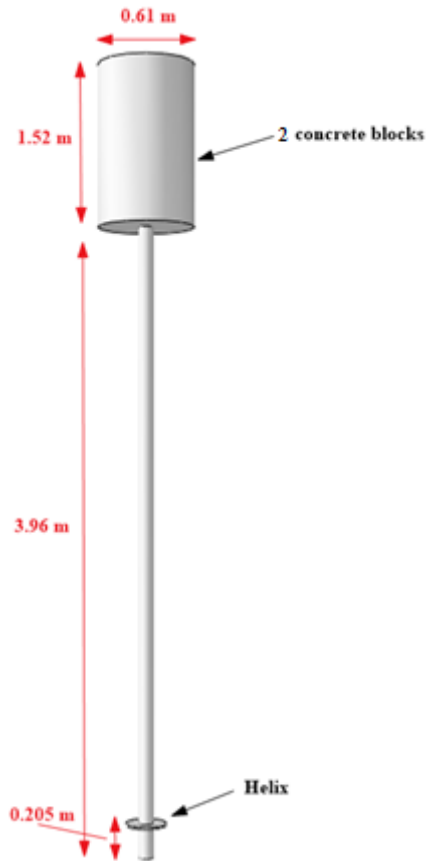


Figure 5-2: Pile 1 dimensions

5.2 Element type

There are several finite element types available in the ABAQUS library to simulate 3D objects. Each element formulation offers some advantages but also suffers from certain shortcomings. A brief discussion of the element types available in ABAQUS library and their formulation is presented below (SIMULIA, 2013b):

The element library includes First-order (linear) interpolation element shapes such as *tetrahedron* (4-node), *triangular prism* (6-node), *hexahedral/brick* (8-node) and second-order (quadratic) interpolation element shapes such as *quadratic tetrahedron* (10-node), *quadratic triangular prism* (15-node) and *quadratic hexahedral/brick* (20-node). First-order triangular and tetrahedral elements are avoided because they are overly stiff and suffer from slow convergence with mesh refinement. First-order hexahedral elements provide accurate results if used with a well structured mesh. In general, second-order elements provide more accurate results, albeit at the cost of higher computational demand.

There are two options for the formulation of the element stiffness, reduced integration and full integration. Fully integrated elements may suffer from shear and volumetric locking when subjected to bending, which may cause these elements to be “too stiff” in bending. Reduced integration allows for a reduction in the number of integration points within the element, which results in substantially lower computation time with minimal difference in accuracy. In addition, reduced integration elements do not suffer from shear and volumetric locking. However, reducing the number of integration points to one may cause “hourglassing”, due to the element distortion such that the calculated strains at the integration point remain zero. The most recent version of ABAQUS, which was employed in the current analysis, an improved hourglass control option has been added, which almost eliminates hourglassing completely. Figure 5-3 shows a comparison between reduced and fully integrated 8-node brick elements.

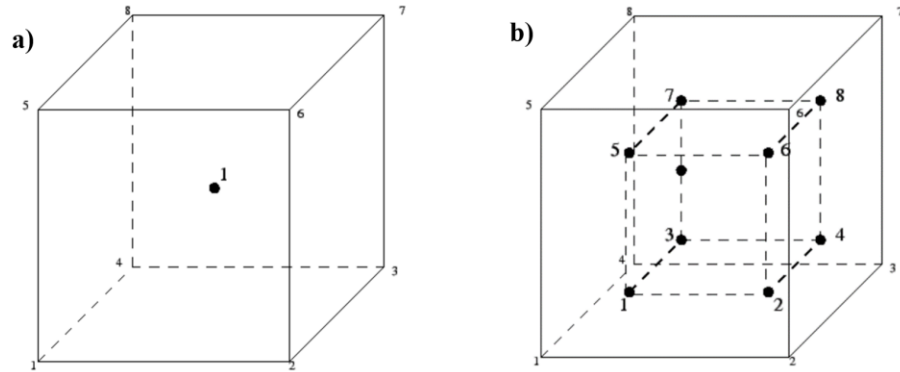


Figure 5-3: Comparison between reduced and fully integrated 8-node brick elements a) reduced integration b) full integration

Based on the discussion above, both the soil block and pile are modeled using 3-dimensional 8-noded, first order (linear), reduced integration, hourglass control elements (C3D8R). This type of element contains only one integration point (at the center), in contrast with the fully integrated element (C3D8) that contains 8 integration points.

5.3 Material models

5.3.1 Pile material model

The pile was modeled using an elastic - perfectly plastic material model. The failure criteria is determined by yield strength of the pile's material (steel). Initially, the pile behaves as a perfectly elastic material until the applied stresses reach the yield strength. Upon reaching the yield strength, the pile deforms plastically. Since no deformations are expected within the concrete block, it is modeled using a rigid material model.

5.3.2 Soil material model

Perhaps the most commonly implemented material model to represent sand behaviour in ABAQUS is the Mohr-Coulomb (MC) model. This is mainly due to the simplicity of the MC model and the few and easily obtained input parameters required to define the model. This model may be sufficient during static loading; however, the non-linear behaviour of soil during dynamic earthquake loading may not be correctly captured by the MC model. ABAQUS allows user-defined material behaviour through the UMAT (User-defined

material) subroutine, but it requires thorough understanding of the finite element formulations, soil behaviour and FOTRAN coding protocols.

Nelson and Dorfmann (1995) proposed parallel mathematical models to represent the non-linear behaviour of materials, denoted the “overlay model”. By using several elements (sharing the same nodes) with different stiffness and yield stresses, any backbone behaviour can be replicated. This method was recently used for non-linear site response analysis by Kaklamanos et al. (2015). However, to the author’s knowledge, this method has not been implemented for soil-structure interaction problems before.

5.3.2.1 Mohr-Coulomb

The MC plasticity model simulates elastic-perfectly plastic behaviour. In this model, the soil deforms elastically with a constant modulus (stiffness) before failure occurs. When the stresses reach the yielding stress (or in this case failure), the soil deforms plastically. The behaviours of the MC model for loading and unloading are shown in Figure 5-4. The yielding criteria is only controlled by two parameters: friction angle and cohesion, i.e.

$$\tau_{yield} = c + \sigma_v \tan(\phi) \quad (5.1)$$

Where c is the cohesion, σ_v is the overburden (vertical) stress, ϕ is the friction angle and τ_{yield} is the resulting failure/yield stress.

However, real soil displays nonlinear behaviour, even before stresses reach the yield strength of the soil as shown in Figure 5-4. Other limitations of the MC model include: the elastic modulus is considered to be constant and does not vary with strain; the loading and unloading stiffnesses are considered to be equal; and the soil is assumed to behave perfectly plastic when the yield strength is reached.

During dynamic earthquake loading, the soil shear modulus reduces as the shear strain increases. This effect is not captured in the MC model. Furthermore, the unloading-reloading rules, approximated by Masing (1926), are not satisfied in the MC model.

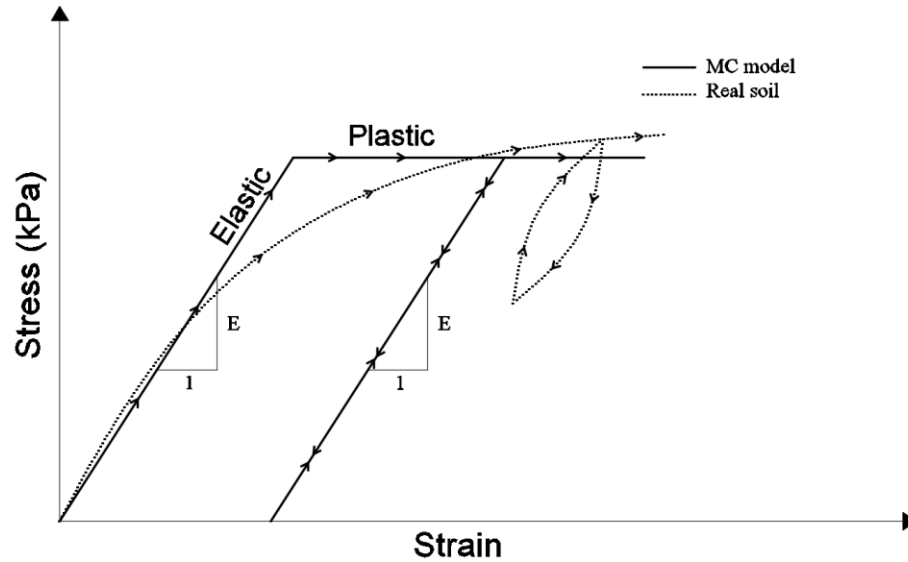


Figure 5-4: MC model behaviour compared to example of real soil

5.3.2.2 Overlay model

By defining an X number of stacked elements that share the same nodes, the behaviour of any backbone curve can be replicated. These elements will have the same strain and will share the total stress depending on their properties. The material models of the individual elements are simple elastic – perfectly plastic models that only require specifying the Young’s modulus and yielding stress. These material models are easily available in all finite element packages and require no further complicated coding by the user. The overlay model concept is further illustrated in Figure 5-5 and Figure 5-6.

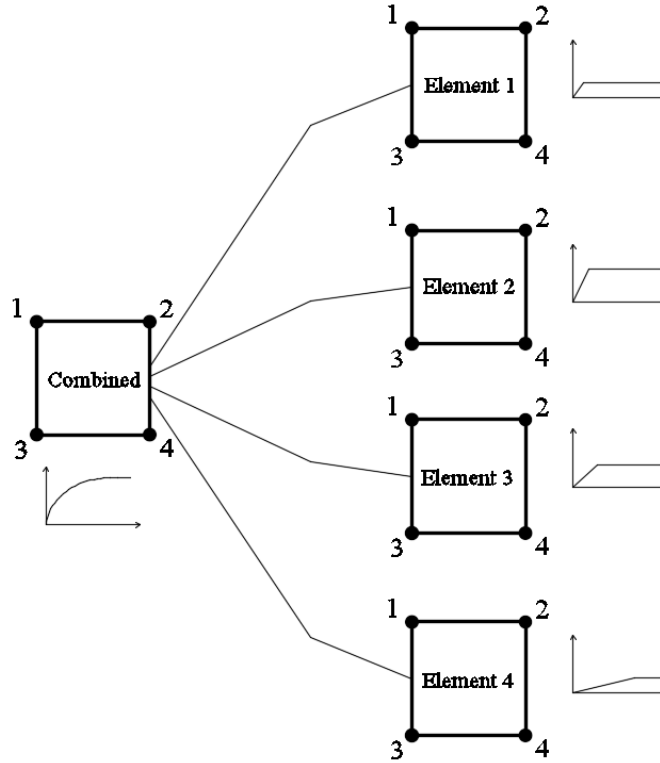


Figure 5-5: Overlay elements schematic in overlay model using $X = 4$ stacked elements

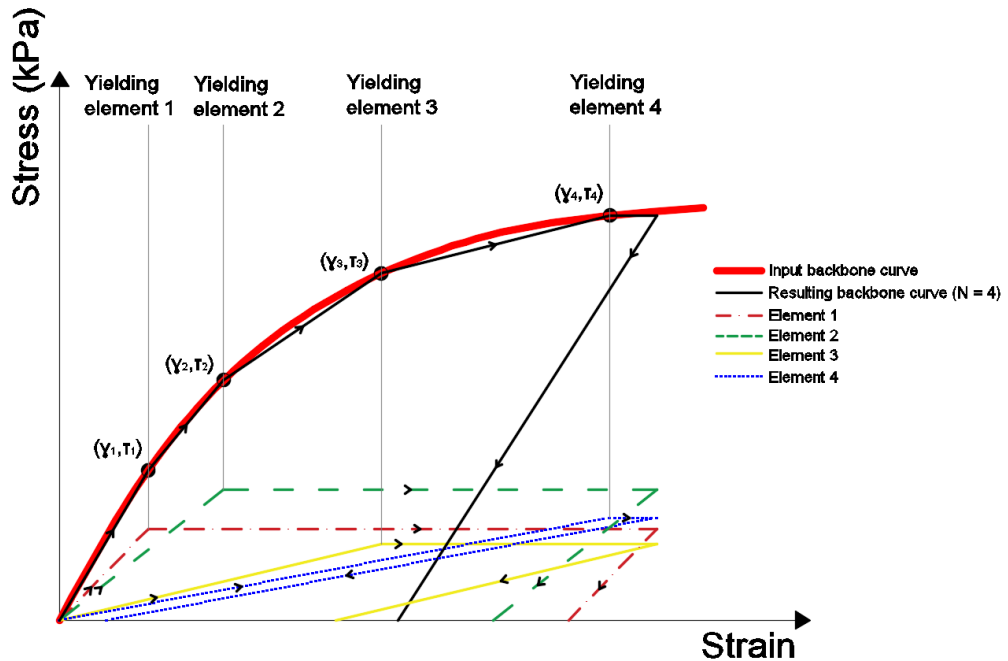


Figure 5-6: One way loading-unloading stress-strain behaviour of overlay model using $X = 4$ stacked elements

The overlay method accounts for stiffness reduction with strain and also the unloading-reloading behaviour following the Masing (1926) rule. To obtain the model parameters, only three input parameters are needed: the desired *backbone curve*, the *number of stacked elements* (X) and the *corresponding points* (γ_i, τ_i) on the backbone curve. The resulting output parameters are the material properties of each stacked element that includes the Young's modulus and plastic yield stress. The material properties for X number of elements are calculated as follows (Kaklamanos et al. 2015):

$$G_{Overlay-1} = \frac{\tau_1}{\gamma_1} - \frac{\tau_1 - \tau_2}{\gamma_1 - \gamma_2} \quad (5.2)$$

$$G_{Overlay-i} = \frac{\tau_{i-1} - \tau_i}{\gamma_{i-1} - \gamma_i} - \frac{\tau_i - \tau_{i+1}}{\gamma_i - \gamma_{i+1}}; \quad i = 2, 3, \dots, X - 1 \quad (5.3)$$

$$G_{Overlay-X} = \frac{\tau_{X-1} - \tau_X}{\gamma_{X-1} - \gamma_X} \quad (5.4)$$

$$\tau_{Overlay-1} = \frac{\tau_2 \gamma_1 - \tau_1 \gamma_2}{\gamma_1 - \gamma_2} \quad (5.5)$$

$$\tau_{Overlay-i} = \frac{\tau_{i+1} \gamma_i - \tau_i \gamma_{i+1}}{\gamma_i - \gamma_{i+1}} - \frac{\tau_i \gamma_{i-1} - \tau_{i-1} \gamma_i}{\gamma_{i-1} - \gamma_i}; \quad i = 2, 3, \dots, X - 1 \quad (5.6)$$

$$\tau_{Overlay-X} = \tau_X - \frac{\tau_X \gamma_{X-1} - \tau_{X-1} \gamma_X}{\gamma_{X-1} - \gamma_X} \quad (5.7)$$

Where γ_i, τ_i are the input shear stress and shear strain, respectively, corresponding to the points selected on the backbone, $G_{Overlay-i}$ and $\tau_{Overlay-i}$ represents the output shear modulus and yielding stress respectively for element i .

ABAQUS defines elastic-perfectly plastic elements by specifying the Young's modulus and the Von-Mises yielding stress, both calculated as shown below:

$$E = 2G(1 + \nu) \quad (5.8)$$

$$\sigma_{VM} = \sqrt{\frac{1}{2}[(\sigma_x - \sigma_y)^2 + (\sigma_y - \sigma_z)^2 + (\sigma_z - \sigma_x)^2 + 6(\tau_{xy}^2 + \tau_{yz}^2 + \tau_{xz}^2)]} \quad (5.9)$$

Where E is the Young's modulus, G is the shear modulus, ν is Poisson's ratio and σ_{VM} is the Von Mises yielding stress.

Implemented backbone curve

Matasović (1993) proposed a backbone curve relationship, which is a modification of the hyperbolic model by Konder and Zelasko (1963). This backbone formulation is employed in the current study and is given by Matasović (1993):

$$\tau = \frac{G_{\max} \gamma}{1 + \alpha \left(\frac{\gamma}{\gamma_r}\right)^s} \quad (5.10)$$

Where τ is the shear stress, G_{\max} is the maximum (initial) shear modulus, γ is the shear strain, α and s are curve fitting parameters (recommended values for sand are 1.47 and 0.72, respectively) and γ_r is the reference shear strain. Hashash and Park (2001) proposed a formulation to take into account the confining pressure in the calculation of reference shear strain:

$$\gamma_r = a \left(\frac{\sigma_v'}{\sigma_{ref}}\right)^b \quad (5.11)$$

Where a and b are curve fitting parameters (recommended values are 0.163 and 0.63, respectively), σ_v' is the vertical effective confining stress and σ_{ref} is the reference confining pressure = 0.18 MPa.

The implied friction angle, ϕ , is back-calculated by the following equation (Hashash et al. 2016):

$$\phi = \tan^{-1} \left(\frac{\tau_{\max}}{\sigma_v'}\right) \quad (5.12)$$

Where τ_{\max} is the maximum shear stress, which can be obtained from Equation (5.10) at 10% strain.

Figure 5-7 compares the Matasovic (1993) backbone curve with the Seed and Idriss (1991) mean limit backbone curve, which is widely used to represent cohesionless soils.

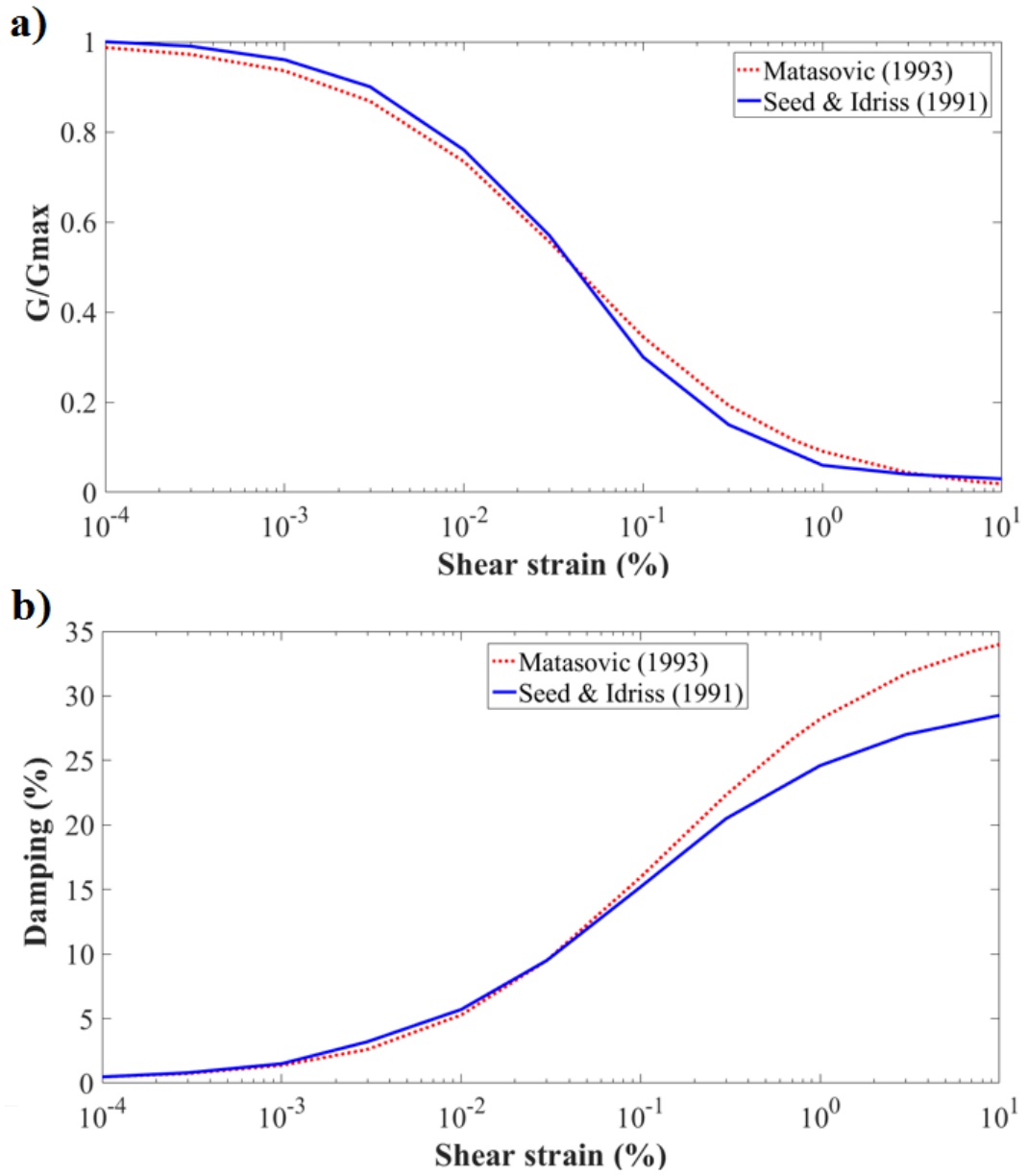


Figure 5-7: Matasovic (1993) versus Seed & Idriss (1991) a) Shear modulus reduction with strain b) Damping with strain

Number of Overlay Elements

Increasing the number of overlay elements allows the user to better capture the behaviour of the backbone curve but with the cost of increased computational time due to the additional number of elements. Kaklamanos et al. (2015) suggested using a minimum of $X = 10$ elements to get a good representation of the backbone behaviour. To minimise computational demand, the number of overlay elements was set to $X = 10$ in all analyses in the current investigation.

Through trial and error, it was found that placing most the selected overlay elements (8) along the initial part of the backbone (at strains less than 5%) captured most of the non-linear behaviour and only 2 elements are sufficient at strains larger than 5%.

To improve computational efficiency, non-linear overlay elements are only used in soil regions of expected high stresses and consequently significant non-linearity. Non-linear soil behaviour due to pile movement is expected around the pile; therefore, overlay elements are implemented for soil elements adjacent to the pile up to a depth of 1.00 m (12 D) and width of 0.20 m (2.5 D). The rest of the soil block is modeled as elastic elements. The regions of elastic and non-linear (overlay) elements are shown in Figure 5-8.

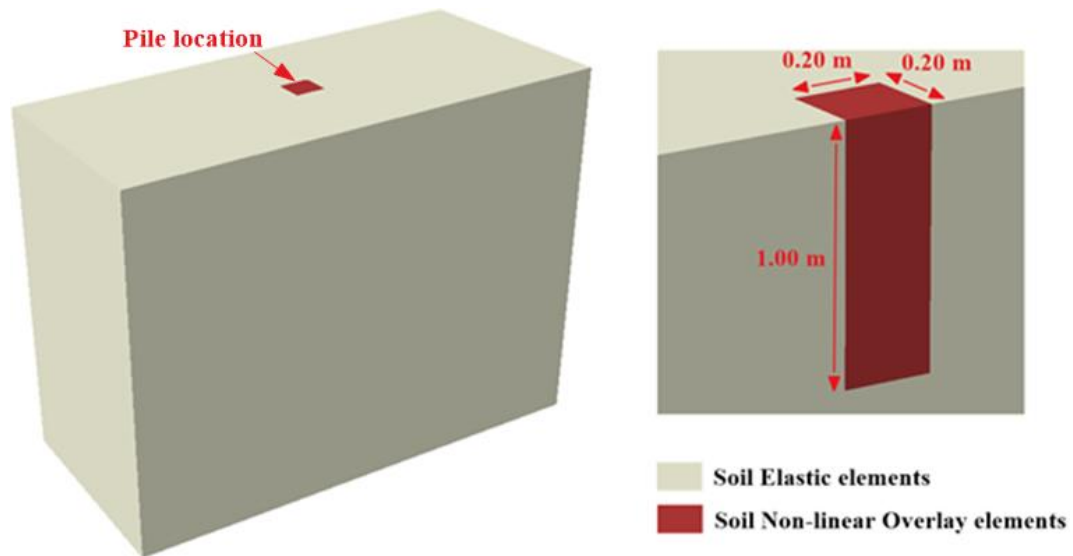


Figure 5-8: Soil block elastic and non-linear regions

5.3.3 Damping

There are two important mechanisms for energy dissipation during dynamic or cyclic loading: viscous (radiation) damping and hysteretic (material) damping. Viscous damping refers to energy dissipation as the wave propagates away from the source. On the other hand, hysteretic damping refers to energy dissipated during inelastic deformations occurring during the loading-reloading of soil in the form of hysteretic loops. Nonlinear soil elements subjected to high strains usually dissipate energy mainly in the form of hysteretic damping; while during low strain excitations, hysteretic damping is negligible due to the lack of inelastic deformations. To provide damping at low strains, viscous damping is incorporated in the form of Rayleigh damping coefficients. Rayleigh damping is also implemented in elastic material models to represent the damping at low and high strains.

5.3.3.1 Viscous damping

Elastic material models do not dissipate energy through hysteretic damping due to the absence of inelastic deformations. Therefore, the damping matrix for elastic elements is calculated considering Rayleigh damping, i.e.:

$$[D] = \alpha_{\text{rayleigh}} [M] + \beta_{\text{rayleigh}} [K] \quad (5.13)$$

Where $[D]$ represents the damping matrix, α and β are Rayleigh damping coefficients, $[M]$ represents the mass matrix and $[K]$ represents the stiffness matrix. The mass-proportional damping coefficient, α , affects lower frequencies while the stiffness-proportional damping coefficient, β , affects higher frequencies. The damping coefficients are calculated as follows:

$$\alpha_{\text{rayleigh}} = \frac{2w_1 w_2}{w_1 + w_2} (\xi) \quad (5.14)$$

$$\beta_{\text{rayleigh}} = \frac{2}{w_1 + w_2} (\xi) \quad (5.15)$$

Where ξ represents the target critical damping ratio, w_1 and w_2 represent the desired frequency range. The variation of resultant net damping with frequency is shown in Figure

5-9. There are several schemes regarding the selection of w_1 and w_2 , some of which are included in Table 5-1.

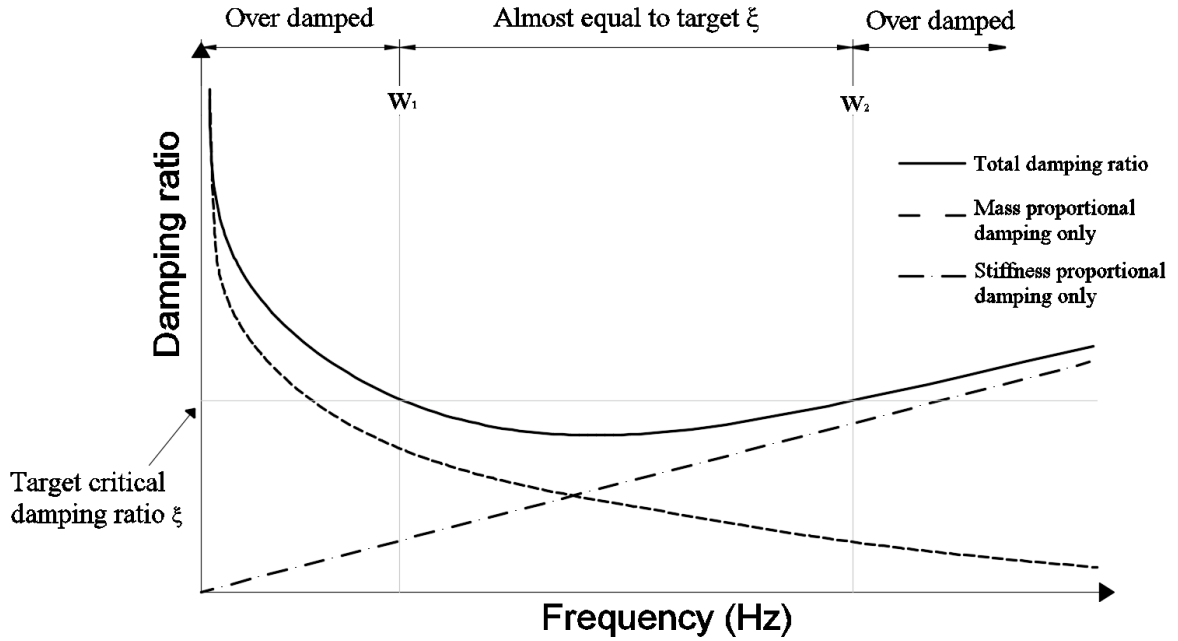


Figure 5-9: Rayleigh damping with frequency

Table 5-1: Selection schemes for w_1 and w_2

	w_1	w_2
Hudson et al. (1994)	f_{n1}	$(\frac{f_{p2}}{f_{n1}})$ rounded to the nearest odd integer
Hashash and Park (2002)	f_{n1}	$(\frac{f_{p2}}{f_{n1}})$ rounded to the nearest odd integer
Amorosi et al. (2010)	f_{p1}	f_{p2}

* f_{n1} : first natural frequency of soil, f_{p1} lower bound of predominant frequency of loading, f_{p2} upper bound of predominant frequency of loading.

In accordance with the suggested method by Amorosi et al. (2010), w_1 and w_2 were set as 0.25 and 8 Hz, respectively, in the current analysis. A value of 5% critical damping ratio was assumed. This selection covered all the important predominant frequencies of loading in the earthquake time records.

5.3.3.2 Hysteretic damping

Hysteretic damping is controlled by the behaviour of the soil deformation during loading-reloading. The nonlinear overlay elements deform following the Masing rule, thus they automatically dissipate energy in the form of hysteretic damping. Hysteretic damping calculation and behaviour is shown in Figure 5-10.

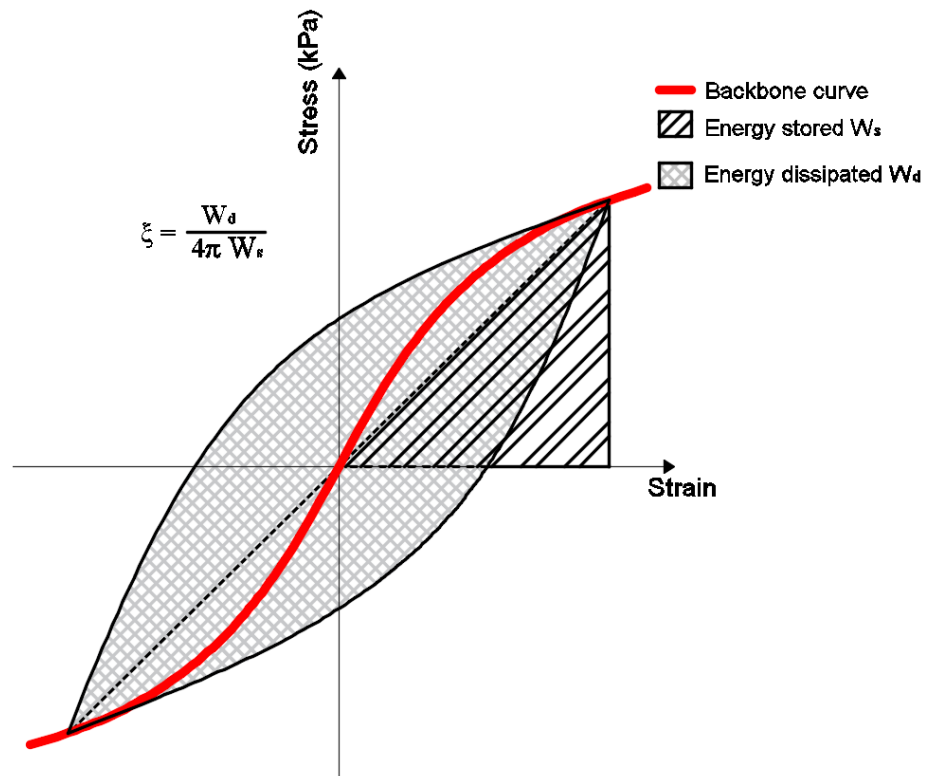


Figure 5-10: Hysteretic damping schematic during one loading cycle for non-linear overlay elements

A summary of the damping used for each element material model is shown in Table 5-2.

Table 5-2: Summary of damping for elastic and non-linear elements

	Viscous damping (%)	Hysteretic damping (%)
Elastic elements	5	0
Non-linear elements (Overlay)	0	(0 – 35)*

*Viscous damping depends on the level of strain as shown in Figure 5-7

5.4 Pile – soil contact interface

ABAQUS provides two algorithms for tracking and defining contact interaction between two surfaces: general contact and contact pair.

General contact is used when the interacting surfaces are not known before the analysis or there are too many surfaces to manually define. In these cases, the general contact becomes computationally demanding as all surfaces are tracked during the analysis.

Contact pair involves defining the contact surfaces that could potentially be in contact. For this reason, contact pair algorithm is computationally efficient as only the specified surfaces are tracked during the analysis. For this reason, the contact pair algorithm is used.

The two surfaces involved in a contact pair interaction are denoted master and slave surfaces. The general rule of thumb is to define the more rigid material as the master surface. For this study, the pile and soil are assigned as the master and slave surfaces, respectively. The contact surfaces are assigned interaction properties covering two behaviours: tangential and normal.

Tangential behaviour is defined by the Coulomb friction model, which is characterized by the friction coefficient, μ , based on the contact nature and materials in contact. As long as the shear stress at contact is less than the critical stress, no slippage occurs. The limiting critical stress is given by:

$$\tau_{crit} = \mu p_{contact} \quad (5.16)$$

Where: τ_{crit} is the critical stress after which movement occurs, $p_{contact}$ is the normal contact pressure between the two surfaces. A friction coefficient of 0.8 was used in the current analysis to represent interface of steel pile surface and dense sand in accordance to value suggested by the Canadian Foundation Engineering Manual (2006).

The normal behaviour is defined as “hard” contact that allows for separation. “Hard” contact ensures that the master or slave surfaces do not penetrate each other.

5.5 Boundary conditions

The lateral vertical boundaries were simulated by the tied boundaries proposed by Zienkiewicz et al. (1989) are implemented. Every pair of nodes at every elevation were tied together in the shaking direction (x – direction). In ABAQUS, this was achieved by enforcing an *EQUATION constraint with the following form:

$$\Delta x_{left_i} - \Delta x_{right_j} = 0 \quad (5.17)$$

Where: Δx_{left_i} is the displacement of node (i) on the left boundary, Δx_{right_j} is the displacement of node (j) on the right boundary. Nodes (i) and (j) are on the same elevation. An illustration of tied boundaries is shown in Figure 5-11.

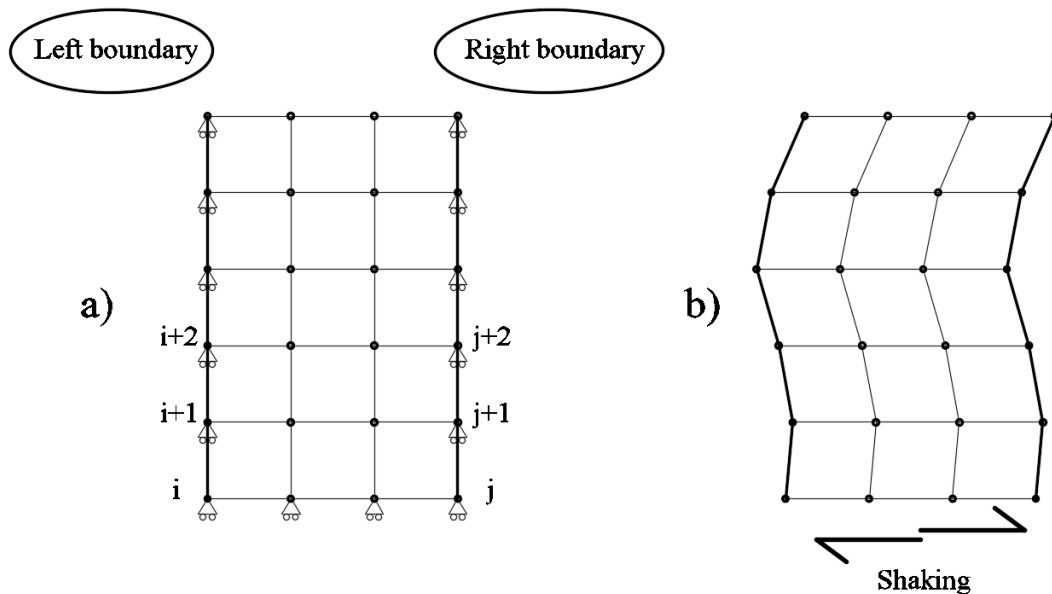


Figure 5-11: Tied boundaries a) Un-deformed b) Deformed

5.5.1 Tied boundary validation

To validate the suitability of tied boundaries to correctly simulate elastic wave propagation and free field conditions, an elastic soil block was excited under earthquake ground motion. The input acceleration was applied at the bottom nodes directly to simulate a rigid base similar to what was applied in the full-scale shake table test. The soil movement was allowed only in the direction of shaking and all other degree of freedoms were locked, which approximately simulated 1D wave propagation. The amplification at the surface and

the transfer function of the soil were then compared with the linear elastic solution obtained by DEEPSOIL.

5.5.1.1 Model input

Table 5-3 summarises the soil properties used for the soil block. Since an elastic material model is used, Rayleigh damping was used to provide energy dissipation. To be consistent, the same methodology for selecting w_1 and w_2 adopted by DEEPSOIL was implemented in finite element model in this study, where w_1 and w_2 were set to be the first and fifth natural frequencies of the soil block. The n th natural frequency of the soil is given by:

$$f_n = (2n - 1) * \frac{V_s}{4H} \quad (5.18)$$

Where f_n is the n -th natural frequency of the soil block, H is the total thickness and V_s is the shear wave velocity.

Table 5-3: Soil properties used for validation of tied boundaries

Soil block	
Thickness (m)	20
Shear wave velocity (m/s)	300
Unit weight (kN/m ³)	17.65
Poisson's ratio	0.27
Damping ratio (%)	2

The Coyote earthquake record, obtained from the PEER strong motion database (PEER, 2010), was applied as the input ground motion with a peak ground acceleration of 0.124g.

5.5.1.2 Results

The amplification at the surface is evaluated as the acceleration calculated at the surface of the soil block divided by the input motion acceleration. This can also be given by the transfer function, defined as:

$$TF(f) = \frac{Acceleration_{surface}(f)}{Acceleration_{base/input}(f)} \quad (5.19)$$

Where $Acceleration_{surface}$ is the acceleration at the surface, $Acceleration_{base/input}$ is the acceleration input at the base and TF is the transfer function and (f) refers to the frequency domain.

Figure 5-12 and Figure 5-13 compare the acceleration time history at the surface and the transfer function, respectively, obtained from DEEPSOIL and ABAQUS.

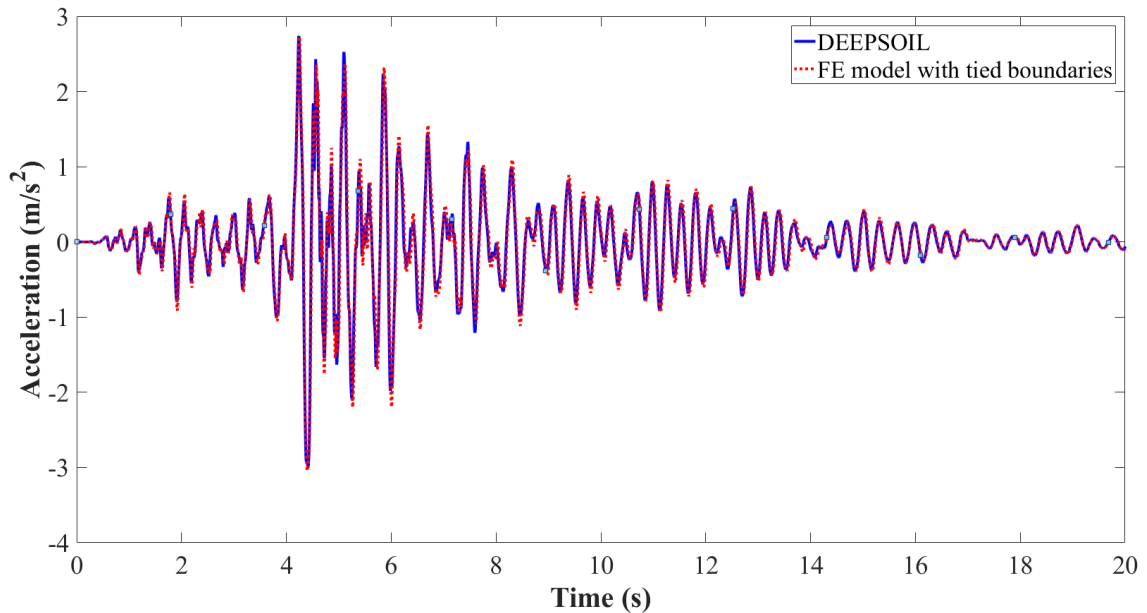


Figure 5-12: Acceleration at surface by DEEPSOIL and FE model with tied boundaries

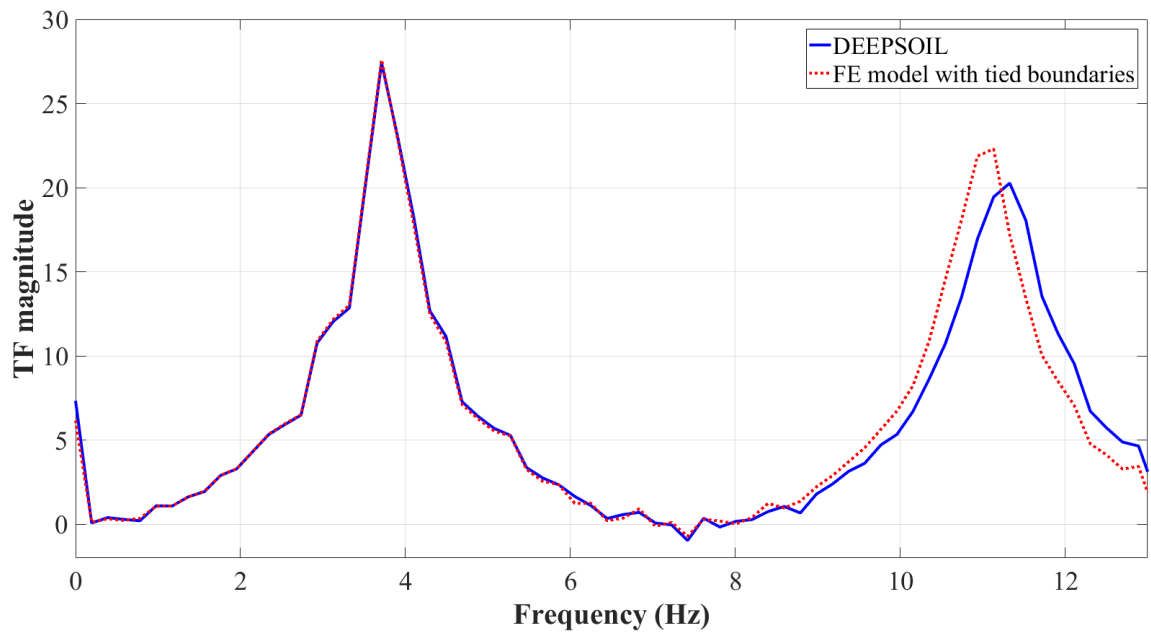


Figure 5-13: Acceleration transfer function (output/input) by DEEPSOIL and FE model with tied boundaries

Figure 5-12 and Figure 5-13 show that the finite element (FE) model with tied boundaries reproduced the correct wave propagation and free-field conditions. The small difference in the transfer function (at the second peak) may be attributed to the 3D effects of wave propagation accounted for in the FE model, while DEEPSOIL assumes strictly 1D wave propagation.

5.6 Mesh sensitivity analysis

The mesh sensitivity was performed in two stages: mesh sensitivity of the pile alone and mesh sensitivity of the combined system (pile installed in soil). The mesh was optimised to yield a balance between computational demand and accuracy. The procedure to obtain the optimum mesh is discussed in this section.

5.6.1 Pile mesh

Most of the deflections experienced by piles during lateral loading occur in the top 10 – 15 D. This was confirmed from the experimental shaking table results, where the moments and deflections of the piles were negligible at 1 m (about 12D) below the ground surface. Therefore, the mesh has been refined in the top 12D to ensure more accurate results within the region of expected high deformations and stresses. The two mesh zones are shown in Figure 5-14.

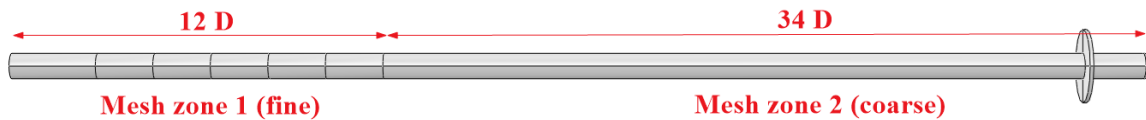


Figure 5-14: Pile mesh zones schematic

A simple lateral load test is performed on the pile alone, i.e., without soil. The main goal of this test was to optimise the mesh at zone 1. The pile was fixed at the bottom up to a depth of 1 m and a concentrated lateral load of 10 kN was applied at the pile head as shown in Figure 5-15. A linear elastic model was used for the pile. The steel material properties are summarised in Table 5-4.

Table 5-4: Pile material properties for mesh sensitivity

Pile	
Unit weight (kN/m ³)	78.50
Young's Modulus (GPa)	200
Poisson's ratio	0.30

The pile behaved essentially as a cantilever beam with a concentrated force acting on its edge; therefore the deflections obtained from ABAQUS is also compared with the closed-form beam theory equation shown below:

$$Deflection(x) = \frac{Px^2}{6EI} (3L - x) \quad (5.20)$$

Where: P is the magnitude of the concentrated force, x is the unsupported distance along the beam, EI is the flexure rigidity of the beam, L is the total unsupported length.

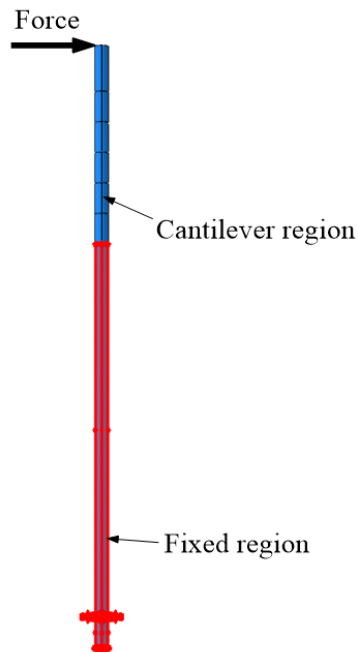


Figure 5-15: Loading for pile mesh sensitivity

Deflection at the pile's head was used as the criterion to judge mesh convergence. The size of elements along the pile's shaft thickness, perimeter and length are varied. The aspect ratio is kept within a range of 1 – 10 to ensure accurate results. Table 5-5 shows the details and results for optimising the pile mesh at Mesh zone 1. The deflection at the pile head is then compared with the closed-form solution by the beam theory. Results showing the error involved in each pile mesh trial is shown in Table 5-6.

Table 5-5: Optimising pile mesh at zone 1 trials


Mesh Details (Mesh zone 1)							
Label	Number of elements	Element size/number Thickness (#)	Perimeter (mm)	Length (mm)	Avg. aspect ratio	Deflection at pile head (mm)	
	1	15600	3	6.5	10	4.72	27.16
	2	5200	1	6.5	10	1.69	27.22
	3	1280	2	13	40	12.80	28.00
	4	640	1	13	40	6.40	28.06

Table 5-6: Error in deflection for each pile mesh trial

Closed-form solution (mm)	
Mesh Label	Error in Deflection (%)
	26.73
1	1.61
2	1.83
3	4.75
4	4.98

Mesh Label 4 was used to mesh the pile (zone 1) as it has shown good performance (less than 5% error) and uses a minimum number of elements without sacrificing accuracy. The pile mesh at zone 2 is set to be slightly coarser than zone 1 which is acceptable since the magnitude of deflections in that region are negligible.

The total elements used for the pile are 1550 elements.

5.6.2 Soil mesh (combined system)

The element size at the pile-soil interface greatly affects the accuracy of analysis. To eliminates convergence issues during contact formulations, the mesh of soil (slave) at the interface must be finer than the mesh of pile (master) (SIMULIA, 2013b). Another constraint on the mesh sizing of the soil elements is controlled by the wave speed in the soil medium. A general rule of thumb is to specify at least 10 elements per wavelength (Alford et al. 1974). The maximum element size is calculated as shown below:

$$size \leq \frac{V_s}{10f_{\max}} \quad (5.21)$$

Where $size$ is the element size allowed, V_s is the shear wave velocity and f_{\max} is the maximum frequency in the input acceleration signal.

Similar to the pile meshing methodology, the soil mesh is split into 2 regions: Fine region (around pile) and coarse region (away from pile). The mesh zones are show in Figure 5-16.

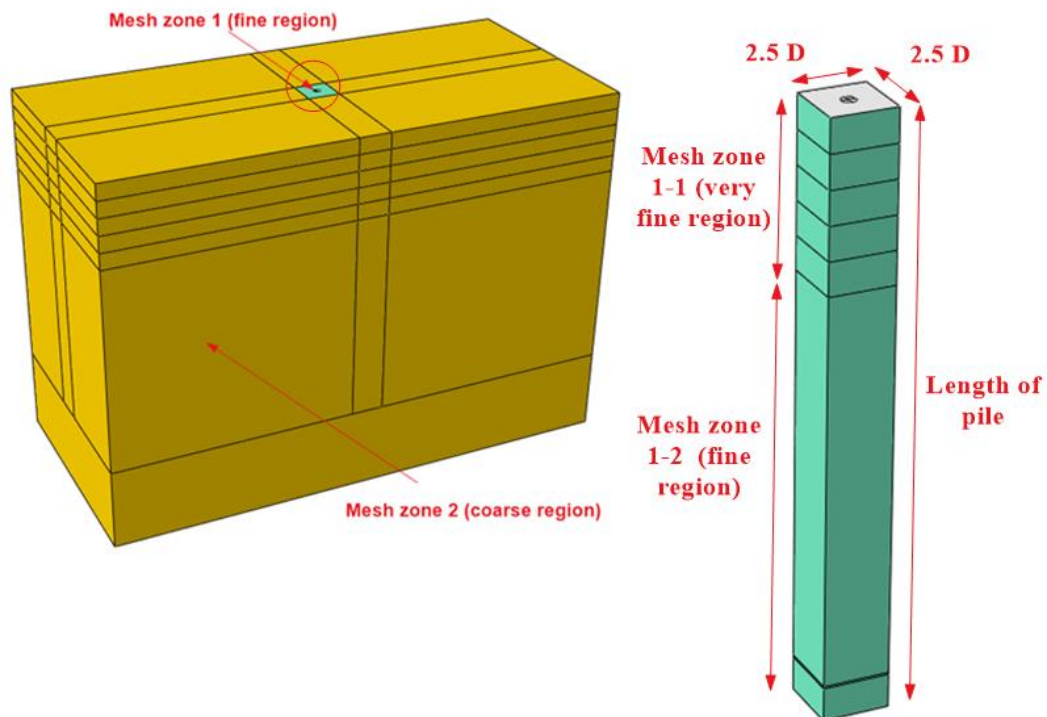


Figure 5-16: Soil mesh zones schematic

A lateral load test was performed on a pile installed in soil to optimise the soil mesh in zone 1. A 10 kN lateral load was applied to the pile head as shown in Figure 5-17. The soil and pile were modeled using linear elastic material models. The soil properties used are shown in Table 5-7. The pile’s mesh and material used in section (5.6.1) were used for this test.

Table 5-7: Soil properties (all layers) for mesh sensitivity

Soil	
Unit weight (kN/m ³)	19.50
Young’s Modulus (MPa)	60
Poisson’s ratio	0.25

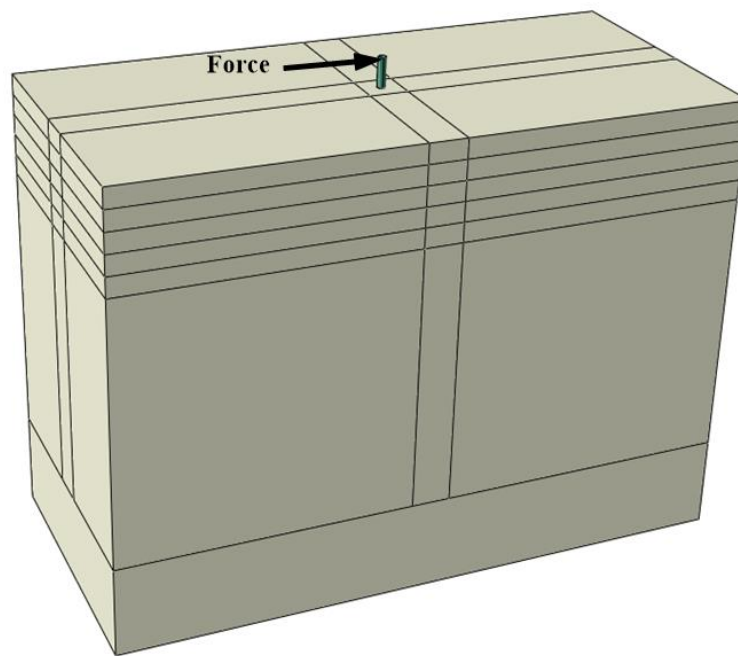


Figure 5-17: Loading on pile for soil mesh sensitivity

The pile deflection was used as the criterion for mesh convergence. The number of soil elements along the pile’s perimeter and length are varied. Table 5-8 shows the details and results for optimising the soil mesh at Mesh zone 1. Table 5-9 shows the change in pile deflection with each soil mesh trial.

Table 5-8: Optimising soil mesh at zone 1 trials


Mesh Details (Mesh zone 1)						
Label	Total elements	Element size		Avg. aspect ratio	Deflection at pile head (mm)	
		Perimeter (mm)	Length (mm)			
	1	64478	5	20	3.81	4.041
	2	44702	8.5	20	2.74	4.052
	3	32934	5	40	6.01	4.053
	4	21054	8.5	40	4.15	4.066

Table 5-9: Change in deflection for each soil mesh trial

Mesh Label	Change in Deflection (%)
1	-
2	0.27
3	0.30
4	0.47

Mesh Label 4 was used to mesh the soil (zone 1). The soil mesh at zone 2 is set to be coarser than zone 1. All elements sizes did not exceed the maximum allowable element size calculated by Equation (5.21).

The total number of elements used for the soil was 90000 elements.

5.7 Final model verification with experimental results

5.7.1 Final model input parameters

The soil profile was discretized into 6 layers as shown in Figure 5-18. As stated earlier, overlay non-linear elements were only used in the vicinity of the pile and the rest of the soil is modeled elastic elements. The soil and pile material parameters used are summarised in Table 5-10 and Table 5-11.

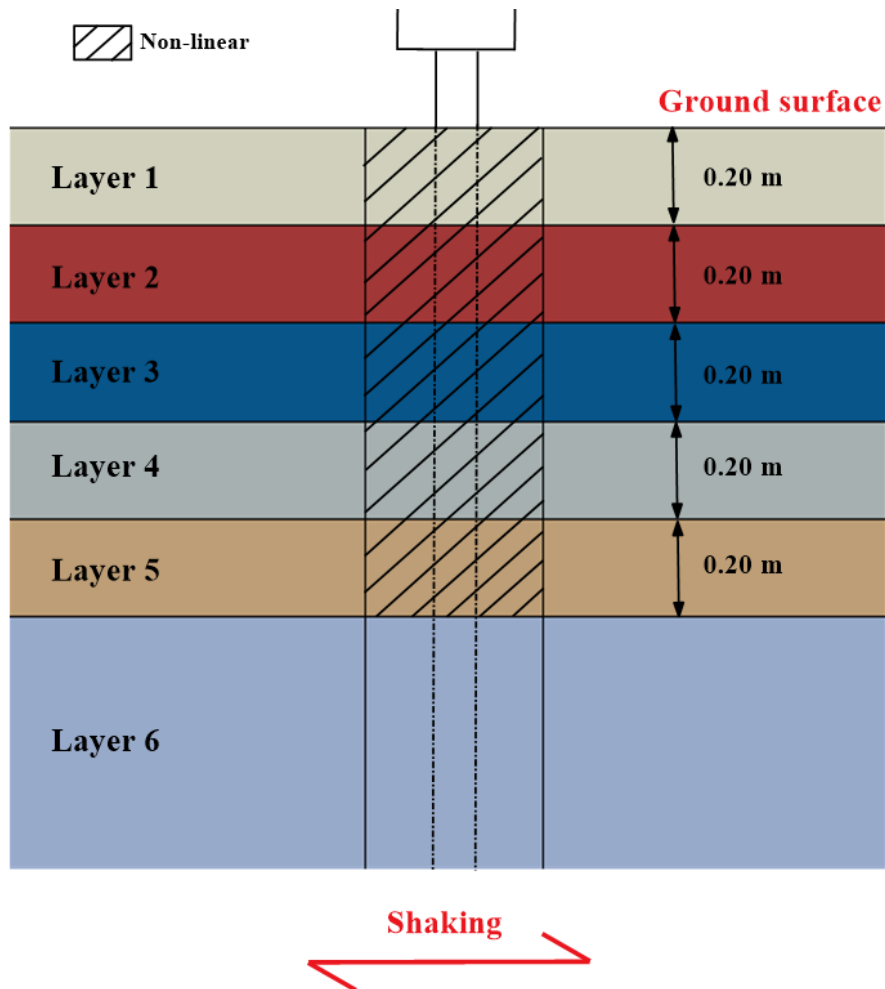


Figure 5-18: Soil profile and layers thickness

Table 5-10: Summary of soil layers properties

Layer	Soil properties				
	Correlated Young's Modulus (MPa)	Final Young's Modulus (MPa)	Poisson's ratio*	Friction angle (°)	Lateral earth pressure** (K _s)
1	25	15			
2	40	60			
3	65	75			
4	85	80	0.25	48.5	1.50
5	85	80			
6	85	82.5			

*assumed as 0.25 which is in accordance with values suggested by (Bowles, 1988)

** assumed as 1.50 which is in accordance to the values suggested for driven piles in very dense sand by (Canadian Geotechnical Society, 2006)

Table 5-11: Pile material properties

Steel		Concrete	
Unit weight (kN/m ³)	78.50	Unit weight (kN/m ³)	25.00
Young's Modulus (GPa)	200		
Poisson's ratio	0.30		
Yield stress (MPa)	450		

5.7.2 Analysis steps

The analysis steps are summarised in Table 5-12. Two solvers can be used in the analysis: implicit and explicit. The implicit solver enforces equilibrium of internal forces with externally applied loads by running Newton-Raphson iterations. Even though this may increase computational time, it produces far more accurate results during highly non-linear contact and material formulations. On the other hand, the explicit solver does not enforce equilibrium at the end of every iteration and generally does not converge unless the time increment is very small, smaller than the Courant time increment. The Courant time is the time needed for the wave to travel across an element. For this reason, the presence of a very small element (in fine meshed regions) may decrease the time step drastically for the explicit solver.

Additionally, the implicit solver is unconditionally stable and generally can solve with larger time increments since equilibrium is enforced at the end of every time increment. On the other hand, the explicit solver is only conditionally stable.

Based on the above reasons, the implicit solver was selected. The time increment is controlled using an automatic controller with a limitation on the maximum time increment equal to the time step of the input signal.

Table 5-12: Analysis steps descriptions and boundary conditions

Step	Description	Boundary condition	
		Vertical	Base
Initial	Pile is deactivated and only soil block exists. Pre-defined geostatic stresses and initial boundary conditions are applied.	$U_x = 0$ $U_y = 0$	$U_x = 0$ $U_y = 0$ $U_z = 0$
Step 1	Geostatic: Own weight of soil is applied to stabilise the initial the geostatic stresses. The pile is still deactivated.	$U_x = 0$ $U_y = 0$	$U_x = 0$ $U_y = 0$ $U_z = 0$
Step 2	Contact interaction: Soil occupying pile's location is removed and pile is activated (wished in place). Contact interaction between pile and soil is activated. Own weight of pile (including concrete block) is applied to initialise the contact and represent the conditions before shaking is applied.	$U_x = 0$ $U_y = 0$	$U_x = 0$ $U_y = 0$ $U_z = 0$
Step 3	Earthquake shaking: Tied boundaries are implemented and the earthquake's acceleration time history is applied at the base of the soil block.	$U_x = \text{tied}$ $U_y = 0$	$A_x = \text{EQ}$ $U_y = 0$ $U_z = 0$

5.7.3 Model assumptions

Finite element modeling provides a powerful and accurate tool to model experimental tests subject to its assumptions and uncertainties. All of the assumptions adopted in the finite element model used herein are listed below:

- The soil parameters used in the model do not account for the disturbance effect of the helix during installation.
- The soil nonlinearity is assumed to be limited to the elements within the nonlinear zone (i.e. width of 2.5D and depth of 12D). The rest of the soil medium is assumed to behave in a linear fashion under seismic loading.
- The model assumes that the experimental setup and pile spacing produces no interaction between neighboring piles, hence only one pile is modeled in the center of the block.
- The model assumes that previous shaking did not affect the soil properties or the results of subsequent shakes.

5.7.4 Verification results

The model was subjected to two loading schemes: white noise and Takatori (100%) records. The white noise record verification ensured that the stiffness of the pile (natural frequency) in the finite element model matched the experimental results. On the other hand, the Takatori earthquake results were used to verify the ability of the overlay modeling methodology to reproduce the non-linear behaviour of soil during seismic events.

5.7.4.1 White noise results

Figure 5-19 compares the Fourier spectra of the pile's response to white noise between the FE model and the experimental results for Pile 1. As it can be seen from Figure 5-19, there is almost a perfect match in the first natural frequency (horizontal mode). However, the second natural frequency (rocking mode) is not matching. This may be due to how the concrete mass connection with the pile head was modeled; in the physical experiment, a bolted steel plate was used at the connection, which may add extra rotation (less stiff) due to the connection not being totally rigid as assumed in the finite element model. The assumption of a completely rigid connection shifts the second rocking mode frequency to

the right. This should not have any effect on the results of the analysis as the horizontal mode is the dominant mode.

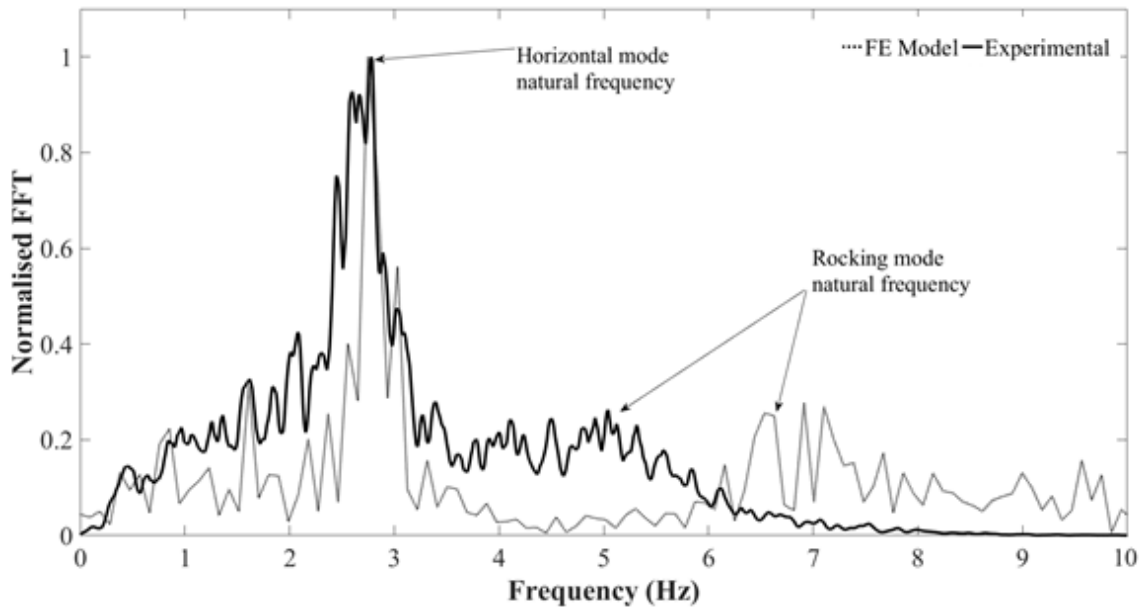


Figure 5-19: Comparison Fourier spectra of pile response to white noise between FE Model and Experiment for Pile 1 (88-C-1HP)

5.7.4.2 Takatori 100% results

The calculated maximum response of the pile was compared with the experimental results as shown in Figure 5-20. There is almost perfect match between the maximum bending moments with depth and maximum displacements with depth.

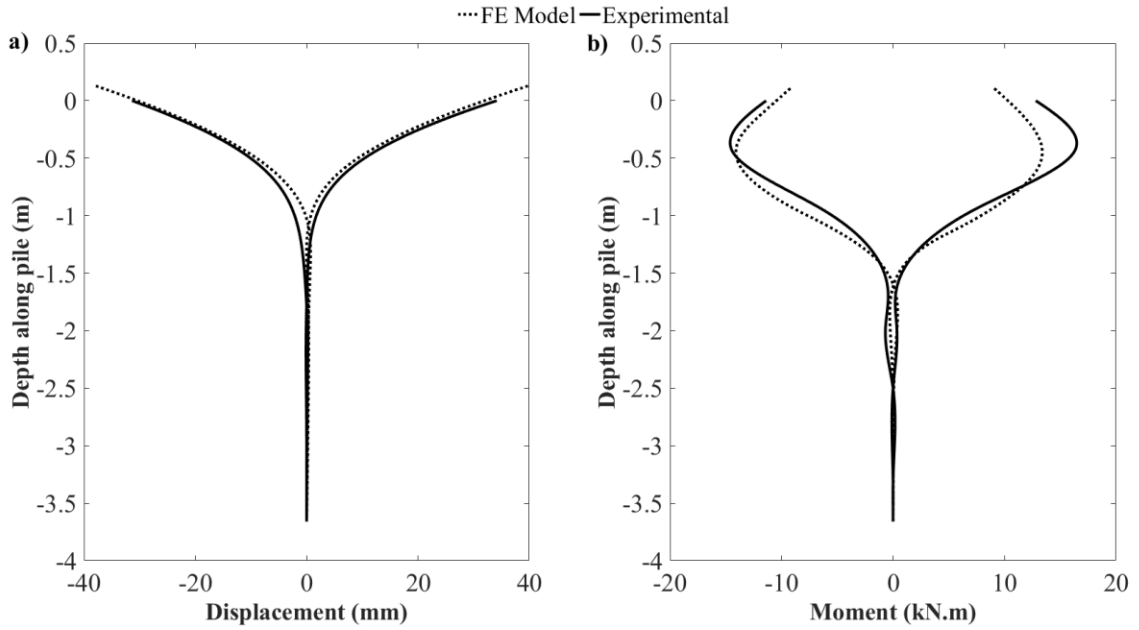


Figure 5-20: Comparison of peak response between FE Model and Experiment results for Pile 1 (88-C-1HP) a) Displacement versus depth b) Bending moment versus depth

The dynamic p-y curves are also compared as shown in Figure 5-21. The comparison shows good agreement which indicates that the non-linear soil model implemented (overlay model) is capable of capturing most of the non-linear behaviour of the soil.

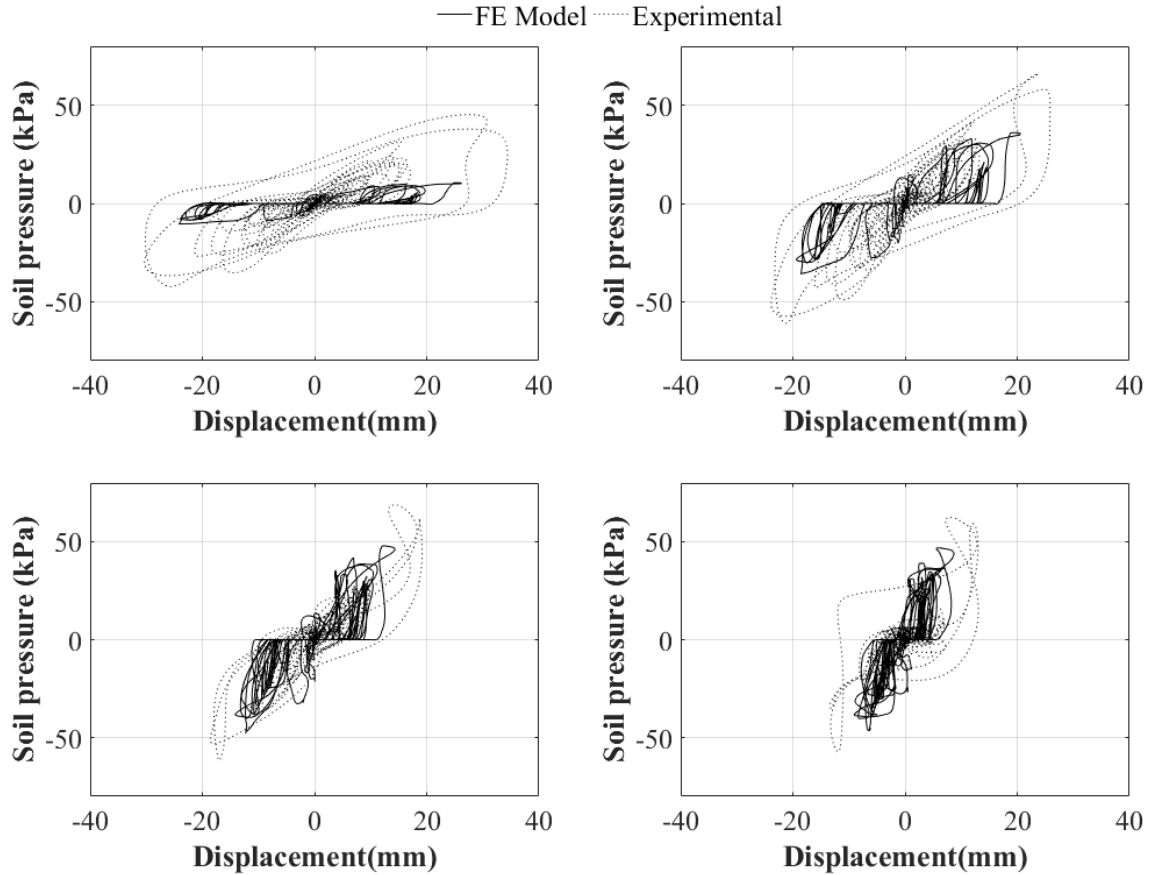


Figure 5-21: Comparison of dynamic p-y curves between FE Model and Experiment results for Pile 1 (88-C-1HP) at different depths a) 1.25D b) 3D c) 5D d) 7D

5.8 Parametric study

The verified numerical model is employed to perform a limited parametric study to investigate the load transfer mechanism of helical piles under lateral loading and to evaluate the effects of pile stiffness and second helix on the p-y curves and pile response. The performance of a similar straight shaft pile is also demonstrated to highlight the contribution of the helix.

To best evaluate the effect of pile stiffness, two cases are considered: flexible (long) and rigid (short) piles. The increase in pile bending stiffness without altering the area exposed to soil can be achieved by either increasing the wall thickness while keeping the outer diameter constant, filling the hollow volume with concrete or increasing the Young's

modulus of the steel. In this study, to obtain the rigid behaviour, the modulus of steel is increased to keep the number of elements in the two models consistent.

The piles are wished into the same soil properties and profile used in the dynamic numerical model (Figure 5-18) was 0.2 m (1.5D) stick out of the pile. The soil is behaviour is simulated using the MC material model to reduce the computational cost of the extra overlay elements. A dilation angle of 15° is assumed to represent the dense sand (Vermeer and de Borst, 1984).

The fixed vertical and horizontal boundaries are placed at a sufficient distance of 10D and 5D, respectively, from the pile. The pile is loaded at the pile head (0.2 m eccentricity above ground) until the pile head has been displaced a total distance of 30 mm. Table 5-13 details the pile’s shaft and helix properties considered. To observe rigid behaviour without altering the area exposed to the soil, the bending stiffness (EI) is increased by 500%. Figure 5-22 shows the schematic and helix locations of the three types of piles considered. The effect of disturbance is not considered for any of the pile types to keep the comparison consistent.

Table 5-13: Pile shaft and helix geometric properties used in parametric study

<i>Shaft</i>		
	Flexible	Rigid
Outer Diameter (mm)	140	
Thickness (mm)	10.0	
Length (m)	2.25	
Inertia (m ⁴)	8.68 x 10 ⁻⁶	
Modulus (GPa)	200	
EI (kN.m ²)	1.75	9.55
<i>Helix</i>		
Outer Diameter (mm)	255	
Thickness (mm)	12.7	

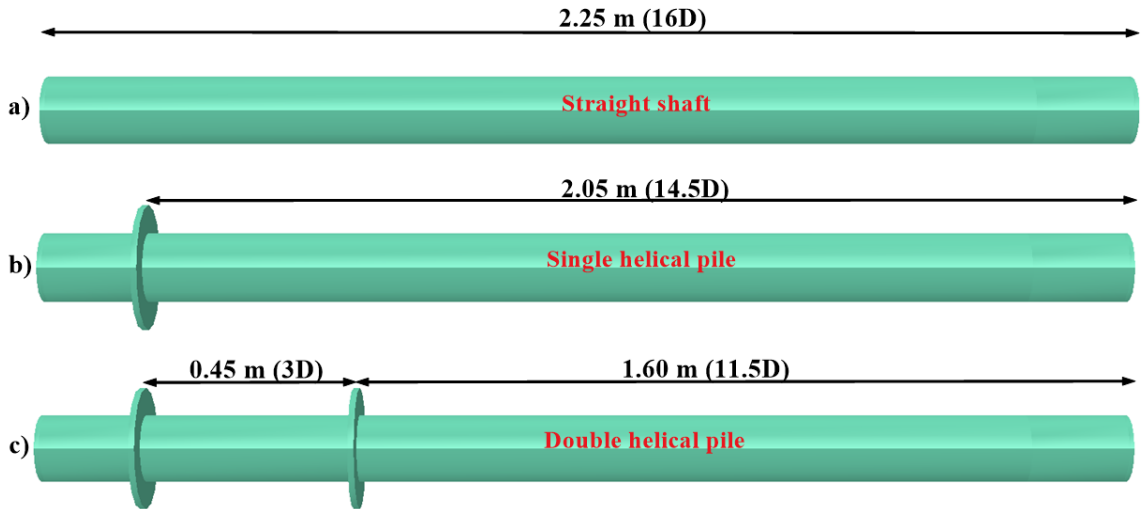


Figure 5-22: Schematic of piles used in parametric study a) Straight shaft b) Single helical c) Double helical

5.8.1 Effect of pile stiffness (EI)

The effect of pile stiffness is evaluated in terms of the global and local behaviour of the pile. The global behaviour refers to the total force versus displacement at pile head, while the local behaviour refers to p-y curves at different depths.

The soil resistance against pile movement can be split into two terms: normal and shear resistance. Normal resistance is due to the normal perpendicular contact between the pile and soil, while shear resistance is due to the tangential friction between the pile and soil as the pile moves against the soil. Figure 5-23 shows the effect of pile stiffness for different on the pile response for different piles considered. As expected, the rotation dominates the deflected shape for the rigid piles whereas flexural deflection defines the behaviour of the flexible piles.

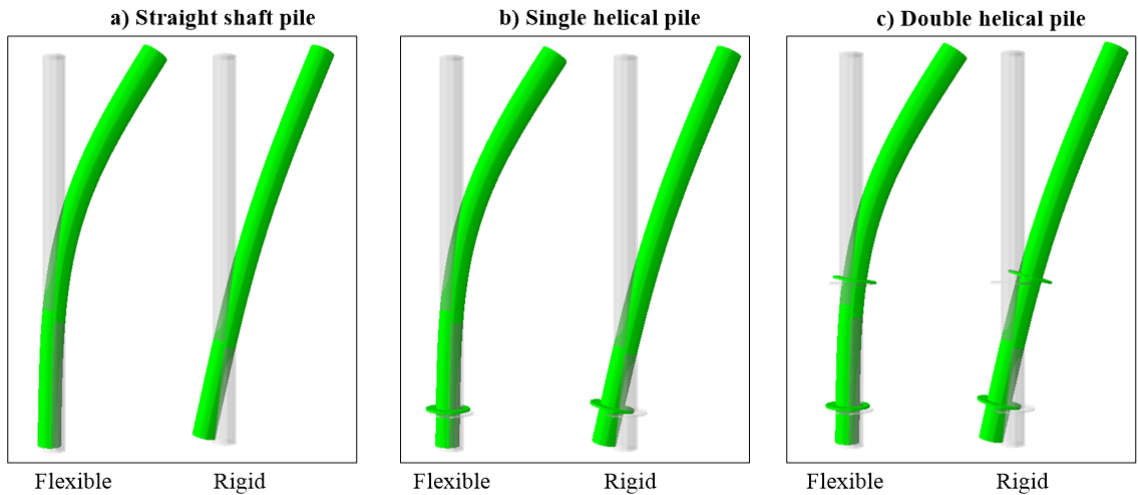


Figure 5-23: Effect of pile stiffness on deflection shape of different pile types a) Straight shaft b) Single helical c) Double helical

Figure 5-24 demonstrates the effect of pile stiffness on the force versus displacement at pile head for different types of piles. The thick lines represent the higher stiffness pile (rigid). The general trend is the same, increasing the stiffness of the pile increases the force required to obtain a displacement of 30 mm.

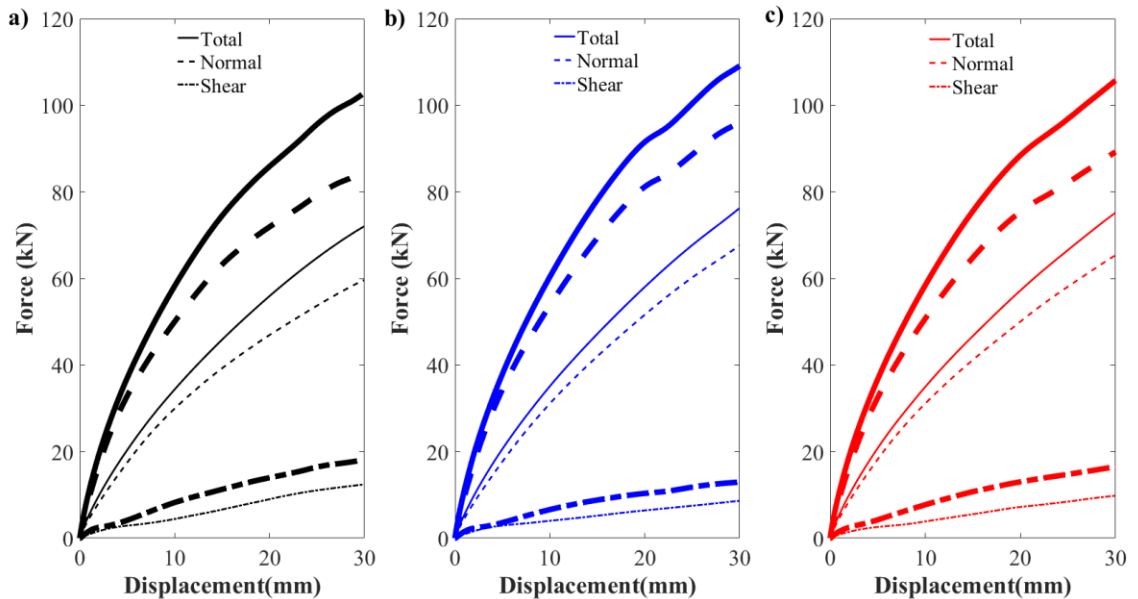


Figure 5-24: Effect of pile stiffness on force versus displacement at pile head for different pile types a) Straight shaft b) Single helical c) Double helical

Table 5-14 summarises the contribution of each soil resistance component for each pile type with different stiffness. It can be seen that during the transition from flexible to rigid behaviour, the contribution of the shear slightly increases. This may be even more evident if larger diameter piles are considered.

Table 5-14: Percentage contribution of each soil resistance component during load for each pile type with different pile stiffness

Pile type	Flexural Stiffness	Normal (%)	Shear (%)
Straight shaft pile	Flexible	83	17
	Rigid	82	18
Single helical pile	Flexible	89	11
	Rigid	88	12
Double helical pile	Flexible	87	13
	Rigid	84	16

The same observation is seen when observing the p-y curves at different depth. Figure 5-25 and Figure 5-26 show the p-y curves due to different soil resistance components at a depth of 3D for single helical and double helical piles, respectively.

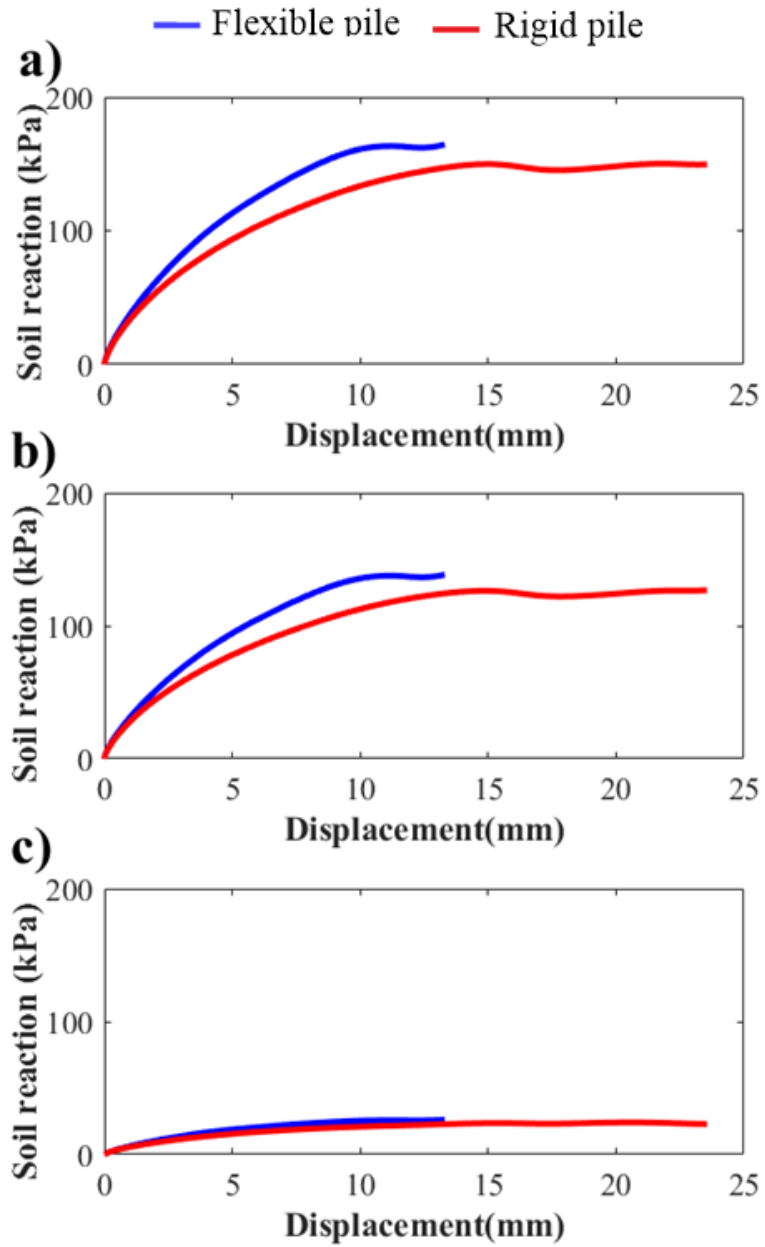


Figure 5-25: p-y curves for flexible and rigid single helical pile at 3D. a) Total b) Normal c) Shear

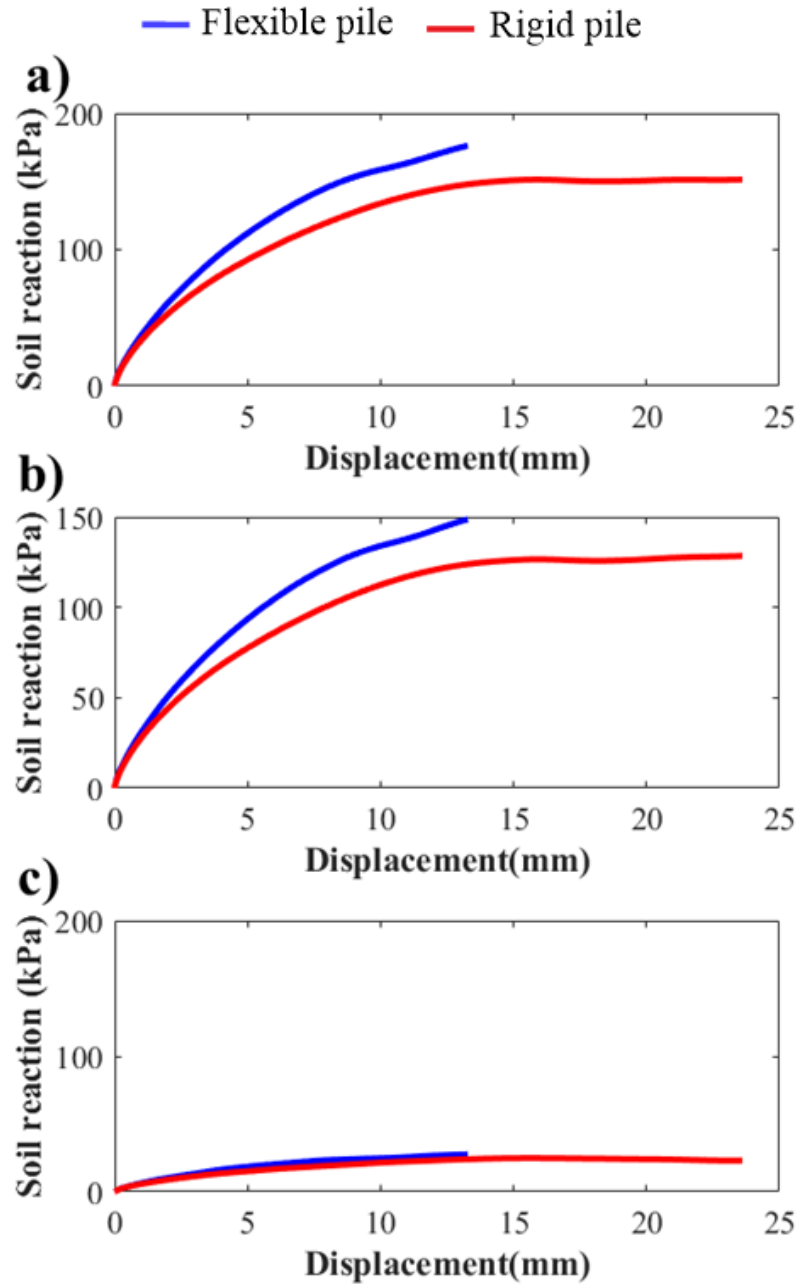
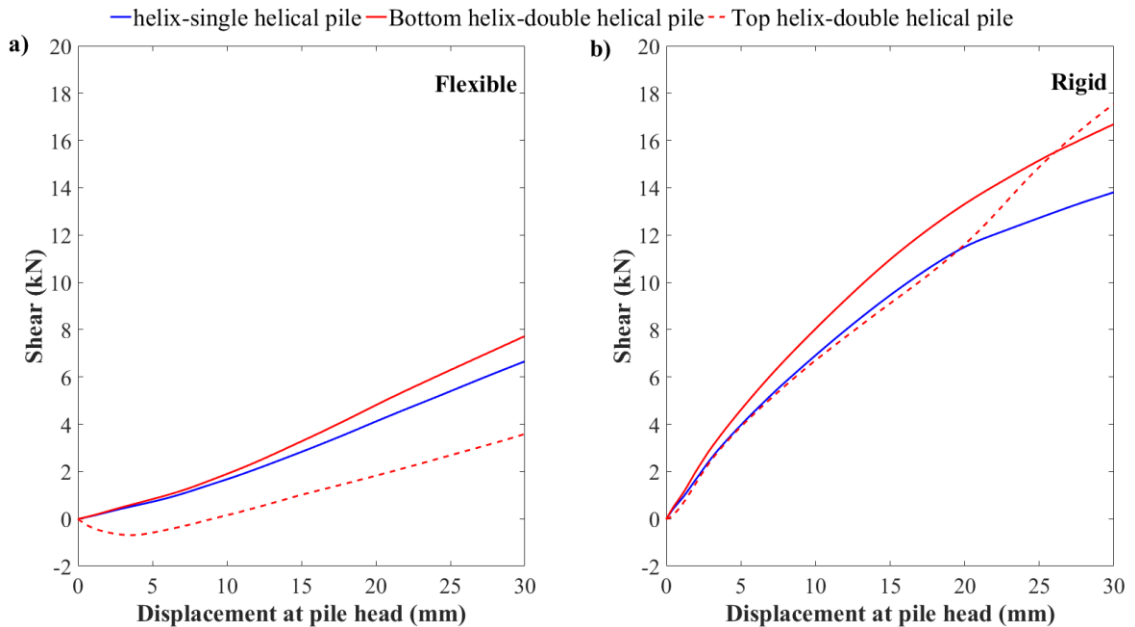


Figure 5-26: p-y curves for flexible and rigid double helical pile at 3D. a) Total b) Normal c) Shear

5.8.2 Effect of addition of second helix

The helical plate provides extra surface area to increase the shear resistance of the pile at that elevation. Also, as the pile rotates, the helix provides fixation by applying moment opposing the motion. Understanding the load transfer mechanism during pile movement and rotation at the helix can aid in modeling the helical plate in simplified models such as BNWF by providing a rotational spring.

Table 5-14 compares the contribution of different soil resistance component to the total soil resistance. As can be seen from Table 5-14, the second helix increased the shear component slightly as compared with the case of single helix pile. This can be furtherly noted by calculating the amount of shear on the helical plate during loading. Figure 5-27 shows the variation of soil shear resistance on the helical plate surface during loading for both the single and double helical piles. When the piles behave flexibly, the bottom helical plates for both piles have almost the same shear resistance with the top helical plate providing a small contribution to shear. However, for piles exhibiting rigid behaviour, both helices in the double helical pile have the same shear contribution as the single helical pile.



**Figure 5-27: Shear at helical plate for both single and double helical piles a) Flexible
b) Rigid**

Figure 5-28 shows the moment developed by the helical plate for both the single and double helical piles. When the piles deform flexibly, the moment accompanied by the very small rotation at the bottom helical plates is very small. For both the flexible and rigid piles, the moment developed due to the bottom helical plate in the double helical pile is equal to the moment developed by the bottom helical plate in the single helical pile. However, for flexible piles, the top helical plate does not carry any moment while for rigid piles, the top helical plate develops some moment but not as much as the bottom helical plate. This is due to the higher overburden pressure at the location of the bottom helical plate.

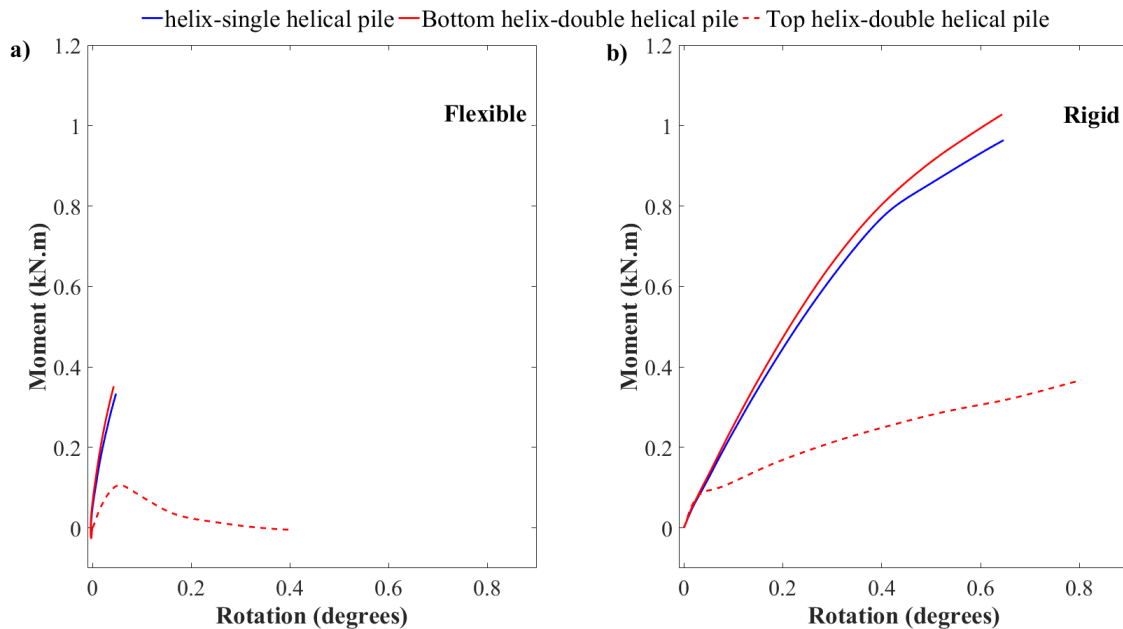


Figure 5-28: Moment due helical plate for both single and double helical piles a) Flexible b) Rigid

The behaviour of the helical plates for both the single and double helical piles which shows the contact status, shear force and normal force on the helical plate after loading is shown in Figure 5-29 to 5-32.

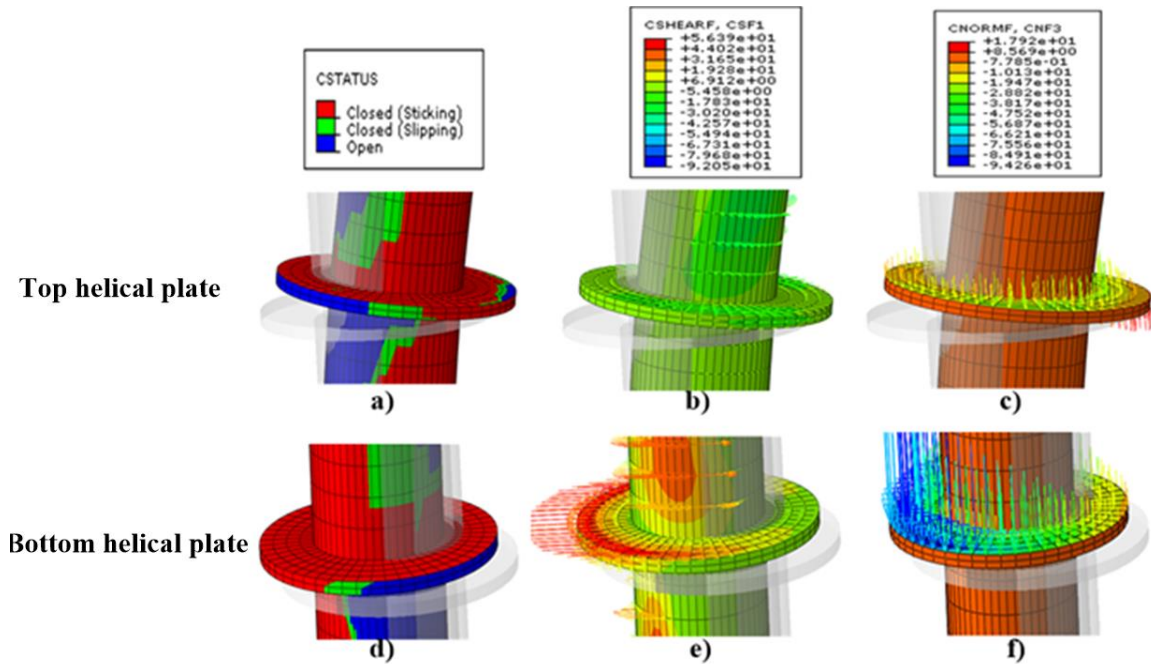


Figure 5-29: Top and bottom helical plates for double helical pile when the pile is flexible a,d) Contact status b,e) Shear force c,f) Normal force

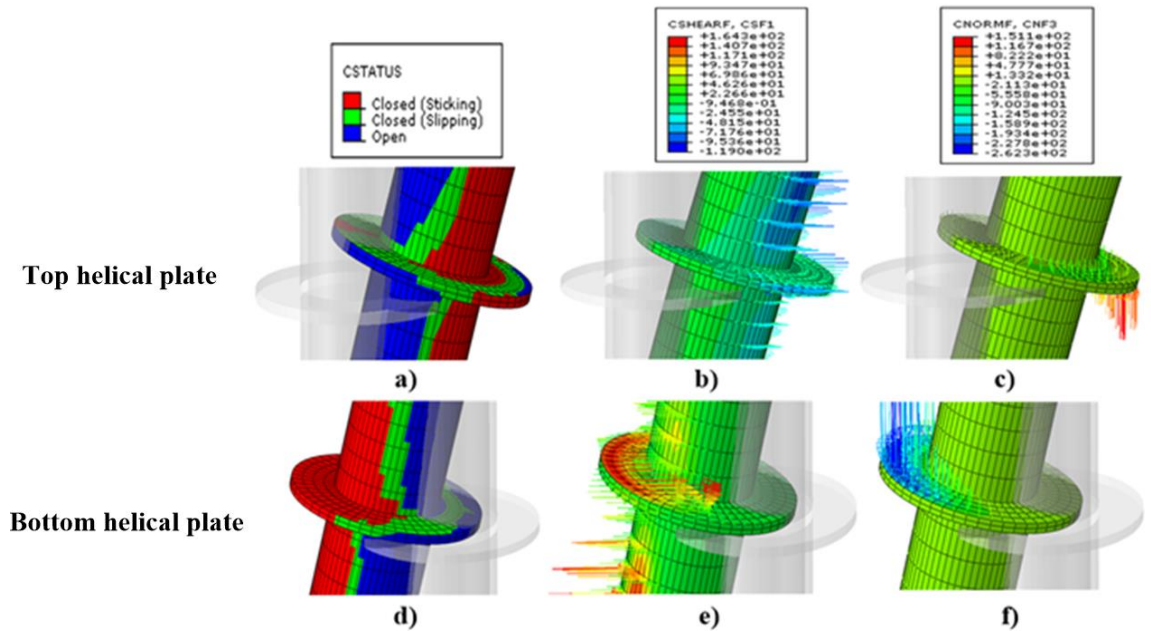


Figure 5-30: Top and bottom helical plates for double helical pile when the pile is rigid a,d) Contact status b,e) Shear force c,f) Normal force

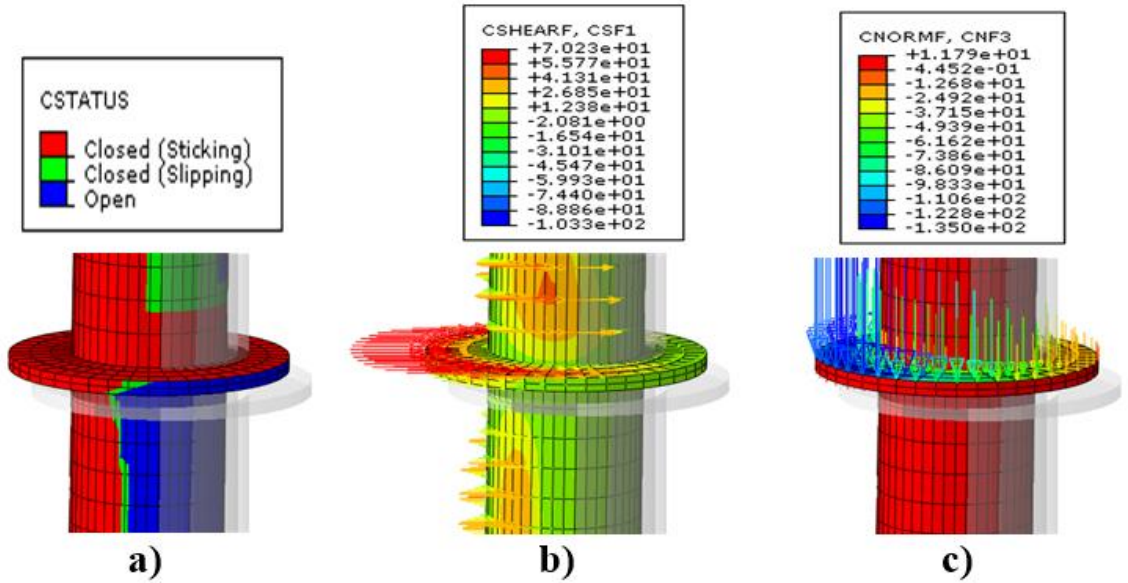


Figure 5-31: Helical plate for single helical pile when the pile is flexible a) Contact status b) Shear force c) Normal force

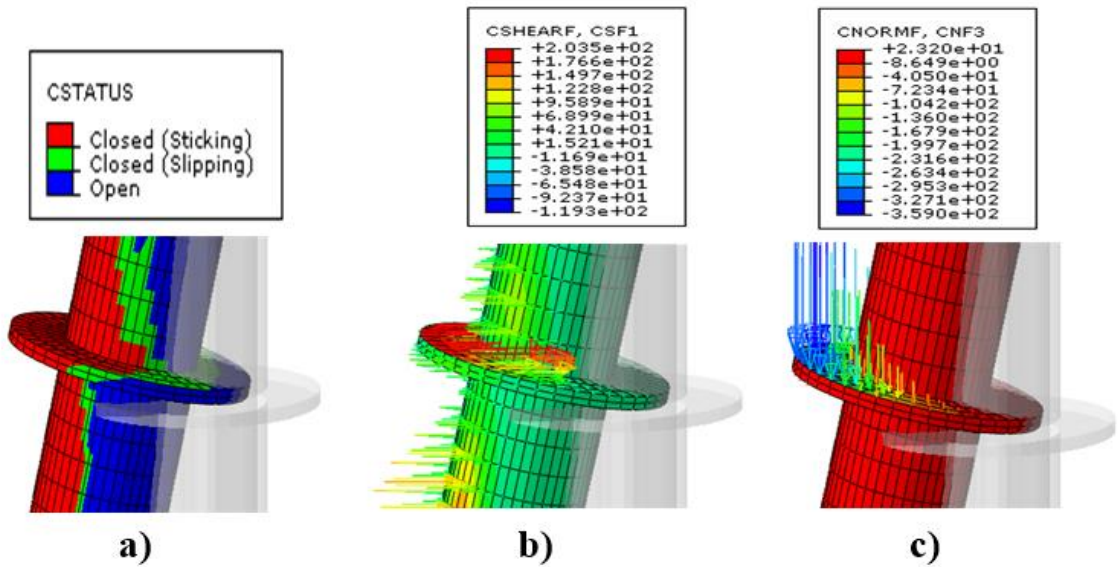


Figure 5-32: Helical plate for single helical pile when the pile is rigid a) Contact status b) Shear force c) Normal force

5.9 Summary

A 3D finite element model is constructed that is verified with experimental results. The tied boundaries implemented showed correct transfer function and the ability to model wave propagation. This tied boundaries replicate the laminar shear box behaviour used in the full-scale shaking table experiment. The overlay method was used to implement the Matasovic (1993) backbone curve proved to be capable of modeling the full non-linear behaviour of the soil which includes stiffness reduction with strain and the Masing's loading-unloading rules.

The limited parametric study performed shows that increasing the pile stiffness may cause a slight increase in the contribution of soil reaction due to shear contact. Further investigation is required using larger diameter piles. Also, the addition of the second helical plate did not affect the behaviour of the bottom helical plate that already existed in terms of shear or moment developed by the helical plate. Lastly, the moment rotation curves presented might offer valuable information to modelling the helical plate in models such as BNWF by replacing the helical plate by a rotational spring with stiffness provided by numerical modeling.

5.10 References

- Alford, R.M., Kelly, K.R., and Boore, D.M. 1974. Accuracy of finite-difference modeling of the acoustic wave equation. *Geophysics*, 39(6): 834–842. Society of Exploration Geophysicists.
- Amorosi, A., Boldini, D., and Elia, G. 2010. Parametric study on seismic ground response by finite element modelling. *Computers and Geotechnics*, 37(4): 515–528.
- Bowles, J.E. 1988. *Foundation analysis and design*.
- Canadian Geotechnical Society. 2006. *Canadian foundation engineering manual*. Richmond, B.C.
- CGS. 2006. *Canadian Foundation Engineering Manual*.
- Hashash, Y.M.A., Musgrove, M.I., Harmon, J.A., Groholski, D., Phillips, C.A., and Park, D. 2016. *DEEPSOIL V6.1, User Manual*. Board of Trustees of University of Illinois at Urbana-Champaign, Urbana, IL.
- Hashash, Y.M.A., and Park, D. 2001. Non-linear one-dimensional seismic ground motion propagation in the Mississippi embayment. *Engineering Geology*, 62(1): 185–206.
- Hashash, Y.M.A., and Park, D. 2002. Viscous damping formulation and high frequency motion propagation in non-linear site response analysis. *Soil Dynamics and Earthquake Engineering*, 22(7): 611–624.
- Hudson, M., Idriss, I.M., and Beirkae, M. 1994. *QUAD4M User's manual*. A computer program to evaluate the seismic response of soil structures using finite element procedures and incorporating a compliant base.
- Kaklamanos, J., Dorfmann, L., and Baise, L.G. 2015. *A Simple Approach to Site-Response Modeling: The Overlay Concept*. *Seismological Research Letters*.
- Konder, R.L., and Zelasko, J.S. 1963. A hyperbolic stress-strain formulation of sands. In *Proceedings of the 2nd Pan American Conference on Soil Mechanics and Foundation Engineering*. Sao Paulo, Brasil. pp. 289–324.
- Kurian, N.P., and Shah, S.J. 2009. Studies on the behaviour of screw piles by the finite element method. *Canadian Geotechnical Journal*, 46(6): 627–638. NRC Research Press.
- Masing, G. 1926. Eigenspannungen und verfestigung beim messing. In *Proceedings, second international congress of applied mechanics*. pp. 332–335.
- Matasović, N., and Vucetic, M. 1993. Cyclic characterization of liquefiable sands. *Journal of Geotechnical Engineering*, 119(11): 1805–1822. American Society of Civil Engineers.

Nelson, R.B., and Dorfmann, A. 1995. Parallel elastoplastic models of inelastic material behavior. *Journal of engineering mechanics*, 121(10): 1089–1097. American Society of Civil Engineers.

PEER. 2010. PEER Ground Motion Database Web Application. Available from <http://peer.berkeley.edu/smcat/> [accessed 10 April 2017].

SIMULIA. 2013a. ABAQUS/CAE. Dassault Systèmes Simulia Corp, RI, USA.

SIMULIA. 2013b. 6.13 User Documentation. Abaqus user's guide.

Vermeer, P. A. & de Borst, R. (1984). Non-associated plasticity for soils, concrete and rock. *Heron* 29, No. 3.

Zienkiewicz, O.C., Bicanic, N., and Shen, F.Q. 1989. Earthquake Input Definition and the Transmitting Boundary Conditions. In *Advances in computational nonlinear mechanics*. Springer. pp. 109–138.

SUMMARY, CONCLUSIONS AND RECOMMENDATIONS

6.1 Summary

The seismic performance of helical piles was evaluated by performing full-scale shaking table tests and three-dimensional numerical modeling using the general finite element program ABAQUS/Standard.

The experimental setup involved installation of ten steel piles with different configurations and pile head masses in dry sand enclosed in a laminar shear box mounted on the NEES/UCSD Large High Performance Outdoor Shake Table (LHPOST). The loading scheme consisted of white noise and two earthquake time histories with varying intensity and frequency content. The performance of different moment curve fitting techniques was compared by performing a simple moment curve fitting study using theoretical data by LPILE. The results of the full-scale shaking table test were then evaluated and examined in terms of natural frequency and response (maximum deflection and dynamic p-y curves) of the test piles. The effects of the loading intensity and frequency, installation method, number of helical plates, pile shaft shape and diameter are evaluated.

The dynamic numerical model constructed included tied vertical boundaries to properly simulate the actual conditions during the shake table tests. In addition, a nonlinear soil material model that considers shear modulus reduction with strain and Masing's loading-unloading rules was used to simulate the soil behaviour during the seismic loading. The soil material model is implemented using the overlay method. The numerical model was verified using the results of the full-scale shake table tests, and then was used to conduct a limited parametric study. The parametric study investigated the effect of pile stiffness and addition of second helix on the static p-y curves.

6.2 Conclusions

Based on the experimental testing program, the main conclusions are listed below:

1. The performance of different moment curve fitting methods heavily depends on the test/instrumentation setup used. It is strongly recommended to perform a simplified analysis for the test setup before developing the instrumentation plan to ensure the number and spacing of strain gauges used are sufficient to produce accurate and reliable results. Through the LPILE curve fitting test, it was shown that the instrumentation scheme used was sufficient and is capable of providing reliable results to evaluate the seismic behaviour of the test piles.
2. The quintic spline interpolation curve fitting method provided the best deflection (y) results for the specific test/instrumentation setup used herein, while quartic and cubic spline approximation curve fitting methods provided the best soil reaction (p) results for piles with 6 strain gauges and piles with 7 strain gauges, respectively.
3. The natural frequency of the piles obtained from the Fast Fourier transform of either the strain gauge or accelerometer readings during the white noise signal displayed the same two peak locations. However, the second peak (rotational degree of freedom) was more pronounced due to the higher location of the accelerometer.
4. When resonance occurred during pile shaking, the dynamic p - y curves showed larger hysteretic loops and higher damping. Furthermore, earthquake shaking with higher amplitudes resulted in higher damping, which was manifested in dynamic p - y curves with larger hysteretic loops.
5. The loading frequency did not have any effect on the backbone of the dynamic p - y curves in any pile.
6. As the intensity of the earthquake increased, the location of the maximum bending moment increased. Also, a rough linear relationship was found between the intensity of the earthquake and the maximum bending moment only when the predominant frequency of loading was close the natural frequency of the pile. However, due to the nonlinear nature of the pile response, further investigation is required.

7. Increasing the mass supported at the pile head decreased the natural frequency of the pile. On the other hand, increasing the pile's diameter resulted in a slight increase in the natural frequency. This is due to the accompanied increase in stick out length with the large diameter piles that causes a decrease in the natural frequency.
8. The double-helix pile showed slightly lower natural frequency than the single-helix pile due to the higher disturbance associated with the second helix during installation. Also, the contribution of the second helix was seen to increase as the pile deflection increased during shaking.
9. The driven pile showed slightly higher natural frequency than the helical pile (after accounting for mass difference) due to the soil disturbance around the helical pile. During the Northridge earthquake, the helical pile's performance was similar to that of the driven pile that supported less mass. This confirms the ability of helical piles to perform as good as driven conventional piles under seismic loading.
10. The square shaft helical pile showed slightly higher natural frequency than the circular shaft helical pile (after accounting for mass difference) due to the higher contact area between the pile and soil when using a square shaft. During shaking, there was no clear advantage for the shape of the pile cross-section (i.e., square or circular). It was also observed that the pile shaft shape had no effect on the backbone of the dynamic p-y curves.
11. The type of coupling (bolted or threaded) had no effect on the dynamic p-y curves or the performance of the piles. This may be due to its deep location below the ground surface or its lack of influence on the stiffness of the pile.

Based on the three dimensional numerical modeling and limited parametric study, the main conclusions are listed below:

1. The overlay method used to implement the Matasovic (1993) backbone curve proved to be capable of modeling the full non-linear behaviour of the soil which includes stiffness reduction with strain and the Masing's loading-unloading rules.

2. Increasing the pile stiffness may cause a slight increase in the contribution of soil reaction due to shear contact. Further investigation is required using larger diameter piles.
3. The addition of the second helical plate did not affect the behaviour of the bottom helical plate that already existed in terms of shear or moment developed by the helical plate.
4. The moment rotation curves presented might offer valuable information to modelling the helical plate in models such as BNWF by replacing the helical plate by a rotational spring with stiffness provided by numerical modeling.

6.3 Recommendations for future research

The results of the current research highlights the ability of helical piles to withstand seismic loads and perform as well as other conventional pile options. To further understand the load transfer mechanisms and behaviour of helical piles during seismic events, the following are recommended for future research:

- Perform full-scale shaking table tests with EQ time records that contain a wider range of frequencies. In addition, using different types of soils such as saturated sand can demonstrate the behaviour of helical piles during liquefaction which is of great important during seismic events. The use of large diameter helical piles (diameters of 0.20 m and up) with different helix configurations.
- Studying the effect of subsequent shaking on helical piles with different diameters and helix configurations to determine whether a certain optimum configuration that shows minimal stiffness reduction can be obtained.
- FE modeling to understand the load transfer mechanics and behaviour of helical piles with different diameters and helix locations during cyclic and seismic loading.

Curriculum Vitae

Name: Moustafa El-Sawy

Post-secondary Education and Degrees: United Arab Emirates University
Al-Ain, United Arab Emirates
2011-2015 B.Eng.

Honours and Awards: PCI Big Beam Competition
2016

Milos Novak Memorial Award
2016

Related Work Experience: Internship
Bechtel International Dubai Office
2014-2015

Teaching Assistant
The University of Western Ontario
2015-2017